Institut für Physikalische und Theoretische Chemie
der Technischen Universität München

Matrix-Isolation Spectroscopy of Mass-Selected Ions

Martin Lorenz

Vollständiger Abdruck der von der Fakultät für Chemie der Technischen Universität München zur Erlangung des akademischen Grades eines

Doktors der Naturwissenschaften

genehmigten Dissertation.

Vorsitzender: Univ.-Prof. Dr. Walter Nitsch

Prüfer der Dissertation:

1. Univ.-Prof. Vladimir E. Bondybey,
   Ph.D. (Univ. of California, Berkeley/USA)
2. Univ.-Prof. Dr. Eckehart Nolte
3. apl. Prof. Dr. Friedrich R. Kreißl

Die Dissertation wurde am 21.11.2000 bei der Technischen Universität München eingereicht und durch die Fakultät für Chemie am 19.12.2000 angenommen.

Contents

List of Figures

List of Tables

Part I

Introductory Chapters

Introduction

> *La perfection non est atteinte, quand ne reste rien à ajouter,*
> *mais quand ne reste rien à enlever.*
>
> ANTOINE DE SAINT EXUPERY

Under normal conditions, molecular ions are highly reactive and thus appear only as short-lived intermediates in chemical reactions. Besides their frequent appearance on earth as solvated ions in aqueous solutions, they are found in the gas phase for example in flames [1, 2] and plasmas [3], as well as in higher layers of our atmosphere, the stratosphere and the ionosphere [4, 5]. In addition to these terrestrial occurrences, it is well-known that molecular ions play an important role in the photochemistry of comet tails [5, 6] and interstellar clouds [7, 8], with the simple H_3^+ ion being the most important molecular ion in interstellar space [9]. Due to these widespread occurrences, molecular ions have attracted more and more attention in the last decades.

Although *mass spectrometry* (MS) allows an easy proof of the existence of molecular ions and their identification by the mass/charge ratio, it is more difficult to obtain structural information about them. To establish gas phase structures of ions, techniques like collision-induced fragmentation, ion/molecule reactions, isotopic labeling and combination with ab-initio calculations have been developed [10]. *Spectroscopy*, on the other hand, yields direct information about the geometry and structure of the examined species, provided that they have appropriate transitions that can be induced by electromagnetic radiation. The combination of these two methods, mass spectrometry and spectroscopy, thus appears to be the “Holy Grail” of physical chemistry since it closes the gap between what mass spectrometrists want and what spectroscopists can do. This combination was first introduced in 1978 combining the multiphoton ionization of neutral molecules and the mass-selective detection of the charged products [11, 12] – a technique which has evolved now to extremely sensitive and widely used methods like resonance enhanced multiphoton ionization (REMPI) [13] or mass analyzed threshold ionization (MATI) spectroscopy [14].

To characterize chemical intermediates and free radicals spectroscopically, the *matrix isolation* (MI) method, first introduced in 1954 by PIMENTEL [15] and PORTER [16], is frequently used nowadays [17]. With this technique, the transient species are trapped (isolated) in a transparent, cryogenic solid (matrix) and afterwards characterized by standard spectroscopic methods ranging from infrared to electronic spectroscopy. To reduce the guest-host interactions, light rare gases at temperatures in the range from typically 4 to 20 K are preferably used as host materials. Matrix isolation has been further developed in the last decades to characterize also molecular ions. The ions can be produced either *in-situ* using for example UV photoionization [18] or electron bombardment [19], or during/before deposition using a pulsed electric discharge [20] or laser vaporization to produce metal cations which further react via charge-transfer with an appropriate precursor substance to produce the desired ionic species [21].

Returning to the desire to couple mass spectrometry with spectroscopy, the first successful matrix isolation studies of mass-selected cations were reported in 1989 by RIVOAL et al. [22] and, almost synchronously, by MAIER and co-workers trapping mass-selected C_2^+, $C_2N_2^+$ and $C_2Cl_2^+$ in solid neon and measuring their electronic absorption spectra by a waveguide technique [23]. Apparently, this MS-MI coupling has several enormous advantages compared with old, conventional MI experiments since it allows the real-time optimization of the ion source and the ion optics, it avoids disturbing impurities in matrices and reduces guest-guest interactions by simply discriminating the unwanted species and finally, it facilitates the identification of unknown species by providing the mass information. Although one has to surmount several obstacles to implement this method such as fragmentation during ion deposition [24] or the accumulation of positive space charge hindering the deposition of further ions [25], up to now five groups worldwide are/were successfully employing this method producing impressive results, which are summarized in section 2.4.1.

Due to the apparent success of this MS-MI coupling, we decided to enhance our existing, conventional matrix experiment by attaching a mass-selection stage. In the scope of this thesis, an apparatus was thus designed and implemented for the matrix isolation of mass-selected ions mainly consisting of a modified, commercial quadrupole mass spectrometer. The successful implementation of this method in our laboratory is demonstrated in this thesis by presenting new results on the spectroscopy of CS_2^+ and $C_6F_6^+$. These ions were produced in microwave discharge or electron-impact sources developed in our laboratory and following mass-selection, trapped in solid neon. Subsequently, they were characterized spectroscopically mainly using laser excitation and laser-induced fluorescence. It turned out that the ion currents of approximately 1-10 nA achieved by our sources are sufficiently high to observe visible and even infrared absorption spectra – methods which are orders of magnitude less sensitive than laser excitation scans.

Additional results were obtained synchronously to the planning and implementation of the new mass-selection experiment by using the old setup, with the most tantalizing results being also presented in this thesis. Transition metal oxides, which show an extremely rich electronic spectroscopy due to the partially filled d-shells of the metal atoms, have also been studied. In particular for the tungsten oxides WO and WO_2, new insights into their vibronic structure were obtained, and the interesting relaxation behavior of WO resulting in intense infrared vibrational emission was investigated.

In collaboration with Prof. Räsänen from the University of Helsinki, we performed also studies on the photolysis of hydrogen halides like HCl and HBr in neon matrices. Annealing of such matrices which were additionally doped with xenon atoms resulted in formation of the novel, neutral rare gas compounds HXeCl and HXeBr [26, 27]. The fact that these new compounds exist even in the weakly polarizable neon environment suggests that they should be capable of existence as free molecules in the gas phase – their observation in the gas phase is still lacking – and appears as an important milestone leading to the very recent discovery of the first stable argon containing compound HArF [28].

The present thesis is divided in four major parts. The first part starts with an introductory chapter dealing with the theoretical foundations such as quantum mechanics of molecules and the effects of isolating a molecule in matrices, and is followed by a chapter giving a detailed description of the experimental setup including the mass-selection stage. In the subsequent parts, the results of this work are presented beginning with the tungsten oxides WO and WO_2 and followed by the novel HRgY compounds. The last major part reports then on new insights into the spectroscopy of the CS_2^+ and $C_6F_6^+$ cations obtained with the new mass-selection apparatus and finally, this thesis is summarized and an outlook on the future development of the experiment is presented.

Chapter 1

Theoretical Basis

This introductory chapter deals with the theoretical foundations which are necessary for a comprehensive understanding of this thesis. To understand the nature of the chemical bonding and with that the geometry and structure of molecules on a microscopic level, *quantum mechanics* is absolutely necessary. The calculation of electronic and vibrational states of molecules, as well as transitions between them (selection rules), is briefly discussed. Finally the effects of embedding a free molecule in a solid matrix environment, the *matrix isolation*, are presented and the properties of suitable matrix host materials, as well as new relaxation pathways for the guest molecule, are discussed.

1.1 Quantum Mechanics of Molecules

1.1.1 The Born-Oppenheimer Approximation of the Schrödinger Equation

A molecule, consisting of N electrons and M nuclei, is a complex many-body system. The non-relativistic dynamics of such a system is quantum-mechanically described by the *time-dependent Schrödinger equation* [29]:

$$i\hbar\frac{\partial}{\partial t}\Psi(\mathbf{r},\mathbf{R},t) = H\Psi(\mathbf{r},\mathbf{R},t) \tag{1.1}$$

where H is the *Hamiltonian* operator, equivalent to the sum of kinetic and potential energy operators

$$H = T_e + T_N + V_{ee} + V_{eN} + V_{NN} \tag{1.2}$$

acting on the *wave function* $\Psi(\mathbf{r},\mathbf{R},t)$ which depends on the position vectors $\mathbf{r} = (\mathbf{r}_1,\ldots,\mathbf{r_N})$ and $\mathbf{R} = (\mathbf{R}_1,\ldots,\mathbf{R_M})$ of the electrons and nuclei, respectively.

Now the main interest of this chapter is finding approximate solutions of the *time-independent* Schrödinger equation, obtained from (1.1) by substituting $\Psi(\mathbf{r},\mathbf{R},t) = e^{-iEt/\hbar}\psi(\mathbf{r},\mathbf{R})$:

$$H\psi(\mathbf{r},\mathbf{R}) = E\psi(\mathbf{r},\mathbf{R}) \tag{1.3}$$

To solve this eigenvalue equation, one has to apply the so-called *Born-Oppenheimer approximation*, which is central to quantum chemistry [30]. Qualitatively, since nuclei are much heavier than electrons, they move more slowly. Hence, to a good approximation, one can consider the electrons in a molecule to be moving in the field of fixed nuclei. Within this approximation, the second term of (1.2), the kinetic energy of the nuclei, can be neglected and the last term, the repulsion between nuclei, can be considered as constant. The remaining terms in (1.2) are called the electronic Hamiltonian describing the motion of N electrons in the field of M fixed point charges. Thus, when substituting $\psi(\mathbf{r},\mathbf{R}) = \phi_{\mathbf{R}}(\mathbf{r})\Phi(\mathbf{R})$ in (1.3), where the electronic wave function $\phi_{\mathbf{R}}(\mathbf{r})$ depends only *parametrically* on the nuclear coordinates, this partial differential equation can be separated in two parts:

$$\begin{aligned} (T_e + V_{ee} + V_{eN})\phi_{\mathbf{R}}(\mathbf{r}) &= E^{el}_{\mathbf{R}}\phi_{\mathbf{R}}(\mathbf{r}) && (1.4)\\ (T_N + V_{NN} + E^{el}_{\mathbf{R}})\Phi(\mathbf{R}) &= E\Phi(\mathbf{R}) && (1.5) \end{aligned}$$

Here the first part constitutes the electronic problem, where the total energy for fixed nuclei must also contain the constant nuclear repulsion $E^{tot}_{\mathbf{R}} = E^{el}_{\mathbf{R}} + V_{NN}(\mathbf{R})$. Methods to solve the electronic problem will be treated in the next section. Equation (1.5) describes the motion of nuclei under their own repulsion and in the average field of the electrons, including translation, rotation and vibration of a molecule. From these nuclear motions only the vibrations, to be described in detail in section 1.1.3, are important for matrix isolation spectroscopy, since rotations are hindered for small, light diatomics (for example CN [31]) and impossible for larger molecules in solids.

The quantitative aspects of this approximation, including the problem of deriving corrections to it, are beyond the scope of this thesis and are discussed for example in [32]. The Born-Oppenheimer approximation, however, breaks down in the case of the so-called *Jahn-Teller effect [33]* and its correspondent for linear molecules, the *Renner-Teller effect*[34]. The general Jahn-Teller effect states that a non-linear molecule with a degenerate electronic ground state is instable; it will change its nuclear configuration so that the previously higher symmetry gets broken and the degeneracy splits. For example the linear CS_2^+ cation in its $^2\Pi_g$ ground state with its non-zero orbital angular momentum is subject to the Renner-Teller effect, see for example Ref. [35] for a detailed *ab-initio* calculation on this topic.

1.1.2 Ab-Initio Quantum Chemistry

Finding and describing approximate solutions to the electronic Schrödinger equation (1.4) has been a major preoccupation of quantum chemists since the birth of quantum mechanics. Except for the simplest cases like H_2^+, which can be solved analytically, one is faced with complex many-particle problems. To overcome these problems, appropriate approximations and numerical calculations are absolutely necessary. Central to attempts at solving such problems is the *Hartree-Fock Self-Consistent Field* (HF-SCF) approximation. This method, and the more elaborate *Density Functional Theory* (DFT), which is used for theoretical calculations in later chapters, are shortly covered in this section.

Hartree-Fock

The Hartree-Fock approximation, which is equivalent to the molecular orbital approximation, is central to physical chemistry. The simple picture, that chemists carry around in their heads, of electrons occupying orbitals is in reality an approximation, sometimes a very good one but, nevertheless, an approximation — the Hartree-Fock approximation. Since electrons, with their spin $\frac{1}{2}$, are fermions, they have to obey the *Fermi-Dirac* statistics, i. e. the wave function of the electrons $\phi(\mathbf{r})$ must be antisymmetric on exchange of two electrons: $\phi(\mathbf{r}_1, \ldots, \mathbf{r}_a, \ldots, \mathbf{r}_b, \ldots, \mathbf{r}_N) = -\phi(\mathbf{r}_1, \ldots, \mathbf{r}_b, \ldots, \mathbf{r}_a, \ldots, \mathbf{r}_N)$. Now, the easiest way to construct such a wave function is to build an anti-symmetrized product function $|\phi_0\rangle$ from single-electron wave functions (spin orbitals) $\chi_a(\mathbf{r}_a)$, the so-called *Slater determinant,* abbreviated as

$$|\phi_0\rangle = |\chi_1\chi_2\cdots\chi_N\rangle \tag{1.6}$$

The goal of the Hartree-Fock approximation is now to find the best possible approximation $|\phi_0\rangle$ to the real ground state of the N electron system. According to the variational principle, the “best” orbitals are those which minimize the electronic energy

$$E_0 = \langle\phi_0|\, H\, |\phi_0\rangle \tag{1.7}$$

This variation then leads to a system of N integro-differential equations for the “best” spin orbitals $\chi_a(\mathbf{r}_a)$ [36]

$$h_a\chi_a + \sum_{b\neq a}\left[\int |\chi_b(\mathbf{r}_b)|^2 \frac{1}{r_{ab}}\,d\mathbf{r}_b\right]\chi_a - \sum_{b\neq a}\left[\int \chi_b^*(\mathbf{r}_b)\chi_a(\mathbf{r}_b)\frac{1}{r_{ab}}\,d\mathbf{r}_b\right]\chi_b(\mathbf{r}_a) = \varepsilon_a\chi_a \tag{1.8}$$

where $h_a = -\frac{1}{2}\nabla_a^2 - \sum_A \frac{Z_A}{r_{aA}}$ (in natural units) is the kinetic energy and potential energy for nuclear attraction of a single electron a. The orbital energy of the orbital $\chi_a(\mathbf{r}_a)$ is ε_a.

The second term in this Hartree-Fock equation is the *Coulomb* term corresponding to the Coulomb repulsion of electron a in the averaged field of the remaining electrons. The third expression is the *exchange* term, which arises because of the antisymmetric nature of the Slater determinant.

Apparently, this coupled system of integro-differential equations can not be solved analytically, here computers have to jump in and solve this system numerically in an iterative way. Beginning with an appropriate set of start orbitals, the Hartree-Fock equations are solved with the old orbitals as source of the averaged field which results in a new (hopefully better) set of orbitals. This procedure is repeated until changes in subsequent sets become negligible, i. e. the state of self-consistent-field (SCF) is reached.

As a result of this procedure, one obtains orbitals $\chi_a(\mathbf{r})$ and orbital energies ε_a, as well as the total electronic density $\rho(\mathbf{r})$ and the total electronic energy $E^{el} = E_0$. Using these values, one can calculate all molecular properties of interest like dipole moment, polarizabilities, etc. The resulting wavefunction $|\phi_0\rangle$ has a certain symmetry which is connected with the symmetry of the nuclear configuration. This symmetry is used to designate electronic states in close analogy to spectroscopic notation in atomic physics. For linear molecules, it is convention to write

$$^{2S+1}\Lambda_\Omega$$

as symbol for the electronic state, where the total spin S determines the *multiplicity* $2S+1$, $\Lambda = 0(\Sigma), 1(\Pi), 2(\Delta), \ldots$ is the angular momentum of all electrons projected on the symmetry axis and the total angular momentum Ω is the sum of Λ and the projection Σ of the spin S ($\Omega = |\Lambda - \Sigma|, \ldots, |\Lambda + \Sigma|$). Additionally, when the molecule possesses an inversion symmetry, a letter u or g is added in the index for *ungerade* or *gerade* parity.

This Hartree-Fock method can be used to calculate the vibrational potential energy surface $V(\mathbf{R}) = V_{NN}(\mathbf{R}) + E^{El}(\mathbf{R})$ of a certain molecule, which contains information about the equilibrium geometry (the absolute minimum) and the normal vibrations of this molecule.

Density Functional Theory

Hohenberg and Kohn have shown that, without explicit knowledge of the electronic wave function, the total energy of an n electron system can be expressed as a functional of its electron density $\rho(\mathbf{r})$ [37]. Usually the total energy is partitioned in the following way:

$$E(\rho) = E^T(\rho) + E^V(\rho) + E^J(\rho) + E^{XC}(\rho) \tag{1.9}$$

where E^T is the kinetic energy of the electrons, E^V the sum of the coulomb repulsion energies between nuclei (V_{NN}) and the coulomb attraction between nuclei and electrons (V_{eN}), E^J is the so-called coulomb self-interaction of the electron density (V_{ee}), and E^{XC} is the *exchange-correlation* term. Here the first three term can be expressed analytically but, unfortunately, no analytical expression exists for the exchange-correlation term.

Usually, this exchange-correlation term is approximated as an integral of the spin densities $\rho_{a,b}(\mathbf{r})$ (local part) and their gradients $\nabla\rho_{a,b}(\mathbf{r})$ (non-local part):

$$E^{XC}(\rho) = \int f(\rho_a, \rho_b, \nabla\rho_{a,}\nabla\rho_b)\, d^3\mathbf{r} \tag{1.10}$$

For example, the basic local exchange functional, developed for the uniform electron gas, has the following form [38]:

$$E^X_{LDA} = -\frac{3}{2}\left(\frac{3}{4\pi}\right)^{1/3} \int \rho(\mathbf{r})^{4/3}\, d^3\mathbf{r} \tag{1.11}$$

As a result of continuous improvements, since this simple functional showed large error when applied to molecules, the semi-empirical B3LYP functional emerged [39], which is now widely in use in commercial quantum chemistry programs as for example GAUSSIAN94 [40] :

$$E^{XC}_{B3LYP} = (1-c_0)E^X_{LDA} + c_0E^X_{HF} + c_x\Delta E^X_{Becke88} + (1-c_c)E^C_{VWN3} + c_cE^C_{LYP} \tag{1.12}$$

Here the parameters c are fitted to a wide range of small molecules (the G1 set) to obtain best results. The exchange is here a combination of local LDA and Hartree-Fock exchange as well as the non-local Becke88 functional [41]. As correlation energy, a mixture of the local VWN3 [42] and non-local Lee-Yang-Parr functional [43] are used.

This B3LYP methods will be extensively used in the following chapters to compute molecular properties, because it is significantly better than Hartree-Fock due to the explicit inclusion of (semi-empirical) electron correlation. Furthermore, nowadays B3LYP is simply the state-of-the-art method to compute molecules in a reasonable time with reasonable costs. The results of this B3LYP and the more primitive Hartree-Fock method are compared with experimental values

constant	HF/sb	HF/cb	B3LYP/cb	gas phase[a]	neon[b]
electronic energy E [hartree]	-832.463	-832.629	-834.191		
distance r_{S-C} [Å]	1.6087	1.5509	1.5543	1.554	
symmetric stretch ν_1 [cm^{-1}]	569	666	668	615	617.7
bending ν_2 [cm^{-1}]	289/351[c]	298/404	307/372	346	349
asymmetric stretch ν_3 [cm^{-1}]	1121	1132	1237	1200	1206.9

---

[a] from Ref. [44]

[b] this work

[c] two values, due to asymmetric $\pi_x^2\pi_y$ population

Table 1.1: Comparison of *ab-inito* HF and B3LYP using simple 6-31 (sb) and complex 6-311++G(3d,3pd) basis sets with experimental gas phase and matrix values of the linear CS_2^+.

in gas phase and neon matrices in Table 1.1 using the $^2\Pi_g$ ground state of the CS_2^+ cation as example.

1.1.3 Vibrations of Molecules

As shown in the previous sections, the M nuclei of a molecule move in the potential

$$V(\mathbf{R}) = V_{NN}(\mathbf{R}) + E^{El}(\mathbf{R})$$

Generally, this is a complicated function of the nuclei's positions $\mathbf{R}$, it is even sometimes a difficult task to find the absolute minimum of $V(\mathbf{R})$ — the equilibrium geometry of the molecule. To calculate the dynamics of the nuclei, it is useful to apply the *harmonic* approximation, i. e. to develop the potential $V(\mathbf{R})$ around the equilibrium position $\mathbf{R}^0$ to the second order:

$$V(\mathbf{R}) \approx V(\mathbf{R}^0) + \frac{1}{2}\sum_{k,l=1}^{3M} \frac{\partial^2 V}{\partial R_k \partial R_l}(R_k - R_k^0)(R_l - R_l^0) + \dots \qquad (1.13)$$

Resubstituting this harmonic potential into (1.5) results in a Schrödinger equation for $3M$ coupled, harmonic oscillators, corresponding to the $3M$ degrees of freedom of an M-atomic molecule. This equation can be easily diagonalized, resulting in $3M$ eigenvalues ω_i^2 (the harmonical normal frequencies) and corresponding eigenvectors. Since an M-atomic molecule has generally $3M - 6$ vibrational degrees of freedom, it will turn out that several ω_i equal 0. These $\omega_i = 0$ correspond to translations and rotations that are of no interest here, since they are hindered by the *cage effect* of solid matrices.

Taking for example the linear CS_2 molecule, which has $3 \times 3 - 5 = 4$ vibrational degrees of freedom, it turns out that actually only three vibrations have different frequencies, since the bending vibration is doubly degenerated, see Fig. 1.1.

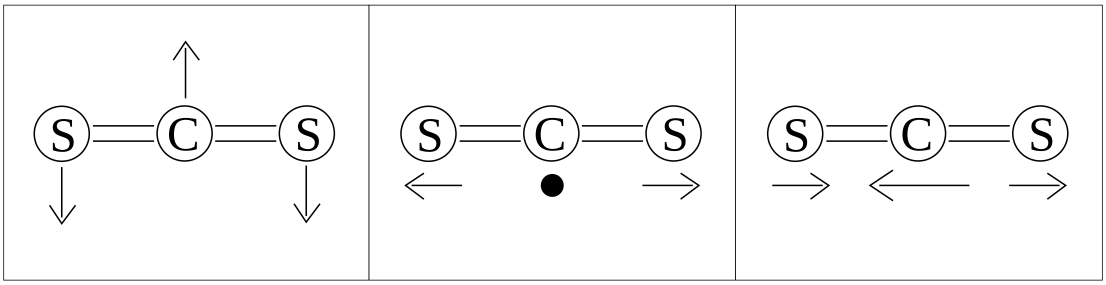

Figure 1.1: The normal vibrations of CS_2: The doubly degenerated bending vibration ν_2 (with symmetry π_u) , the symmetric ν_1 (σ_g) and the antisymmetric stretch vibrations ν_3 (σ_u, arranged in increasing frequency).

This diagonalization results now in $3M - 6$ (or $3M - 5$) decoupled Schrödinger equations for independent harmonic oscillators, whose eigenvalues $E_i = \hbar\omega_i(v_i + \frac{1}{2})$ are well known. Including the fact that vibrational potentials are always more or less *inharmonic*, one arrives finally at the following general formula for the vibrational energy levels [45, 46] (in spectroscopic notation):

$$G = T_e + \sum_i \omega_i(v_i + \frac{1}{2}) + \sum_{i,j} x_{ij}(v_i + \frac{1}{2})(v_j + \frac{1}{2}) + \dots \tag{1.14}$$

where T_e corresponds to the electronic energy at the equilibrium position ($V(\mathbf{R}^0)$), the second term is the harmonic energy of v_i quanta in the ith vibration with frequency ω_i and the third term is the correction due to the anharmonicity of the potential.

1.1.4 Interaction with Electromagnetic Radiation

The interaction of matter with electromagnetic radiation ("light") is central for spectroscopy where absorption or emission of radiation by solids, molecules, atoms or even elementary particles is examined. This effect, physically based on the coupling of the electromagnetic field with electric charges, determines the form of spectra of quantum mechanical systems, for example:

- which lines do appear? (selection rules)
- life time of excited states (and therefore line widths)
- absorption cross sections

To calculate the interaction of the vibrating electromagnetic field with a molecule, one has to perform time-dependent *perturbation theory*, which examines the development of an unperturbed system with the Hamiltonian H^0 perturbed by a time-dependent interaction H^{int}.

Fermi's Golden Rule

This perturbation theory results in the famous *Golden Rule* of Enrico Fermi for the transition rate $W_{i \to f}$ from an initial state $|i\rangle$ to a final state $|f\rangle$ [47]:

$$W_{i \to f} = \frac{2\pi}{\hbar} \delta(E_f - E_i) \left| \langle i| H^{int} |f\rangle \right|^2 \tag{1.15}$$

which states that the transition rate is proportional to the square of the interaction matrix element.

Now one has to specify the operator for the interaction in more detail. Due to the so-called *minimal coupling* $\mathbf{p} \to \mathbf{p} - \frac{e}{c}\mathbf{A}$, one obtains the following expression for the interaction of matter with light:

$$H^{int} = \int \left[e\rho(\mathbf{x})\phi(\mathbf{x}) - \frac{e}{c}\mathbf{j}(\mathbf{x})\mathbf{A}(\mathbf{x}) \right] d^3x$$

To compute transition rates, it is sufficient to use $\mathbf{A}(\mathbf{x}, t) = A\mathbf{e}e^{i(\mathbf{kx} - \omega t)}$ as plane wave ansatz for the vector potential. Taking into account that the dimensions of molecules are small compared with typical wave lengths of the emitted or absorbed light, one obtains for the so-called *electric dipole transition* (E1) from state $|i\rangle$ to $|f\rangle$ and simultaneous annihilation of a photon $\hbar\omega$ with polarization $\mathbf{e}$:

$$W_{i \to f} = \frac{2\pi}{\hbar} \delta(E_f - E_i - \hbar\omega) \frac{\omega^2}{c^2} A^2 \left| \langle i| \mu \cdot \mathbf{e} |f\rangle \right|^2 \tag{1.16}$$

where $\frac{\omega^2}{c^2}A^2 = E^2 \sim I$ is proportional to the intensity of the incident light wave and $\mu = \mu_e + \mu_N = -\sum e\mathbf{r}_i + \sum Z_k e\mathbf{R}_k$ is the dipole moment of the molecule.

Selection Rules

Within the scope of the Born-Oppenheimer approximation, it was shown that the total wave function of a molecule can be approximated by a product of nuclei-, electron- and spin wave functions $|\psi>=|\Phi(\mathbf{R})>|\phi(\mathbf{r})>|\chi_{spin}>$. By that one obtains for the dipole matrix element $M=<i|\mu|f>$ of an electronic transition $i \to f$:

$$M=<\Phi_i(\mathbf{R})|\Phi_f(\mathbf{R})><\phi_i(\mathbf{r})|\mu_e|\phi_f(\mathbf{r})><\chi_i|\chi_f> \tag{1.17}$$

Here the first factor (actually the square $|<\Phi_i(\mathbf{R})|\Phi_f(\mathbf{R})>|^2$) is called the *Franck-Condon factor* which is determined by the overlap of the nuclear wave functions in the lower and the upper electronic state. The second one is the electronic dipole matrix element: If it equals zero, then the electronic transition is called *forbidden.* Thus, one obtains *selection rules* by checking the condition that each factor is nonzero. In this way, the third factor implies the selection rule for the electron spin.

To check whether a pure electronic transition is allowed or not, one doesn't calculate the integral $<\phi_i(\mathbf{r})|\mu_e|\phi_f(\mathbf{r})>$ by hand but instead one inspects symmetries and uses group theory to determine if this integral can become eventually nonzero: An electronic transition is allowed if the direct product of the symmetry species $\Gamma(\phi_i)\Gamma(\mu_e)\Gamma(\phi_f)$ contains the totally symmetric, irreducible species of the molecule's point group. Applying this rule to, for example, linear molecules with weak spin-orbit coupling (Hund's case (a)), one obtains the following selection rules for E1 dipole transitions:

- $\Delta\Lambda = 0, \pm 1$
- $\Delta S = 0$ (no intersystem crossing)
- $\Delta\Sigma = 0$
- $\Delta\Omega = 0, \pm 1$ (also valid for strong spin-orbit coupling)
- $g \leftrightarrow u$, $u \leftrightarrow g$ (where the parity is defined)
- $\Sigma^+ \leftrightarrow \Sigma^+$, $\Sigma^- \leftrightarrow \Sigma^-$

1.2 Molecules in Solids

1.2.1 Properties of Rare Gas Solids

To characterize transient species spectroscopically, it is important to drastically lengthen their usually very short lifetime under laboratory conditions. In the gas phase, this may be achieved by using a very small pressure to increase the average time between two collisions. However, this approach has the disadvantage that one needs very sensitive examination methods, since the interesting species then exists only at very low density. It is furthermore not possible to work at arbitrary low temperatures, so many energy levels are populated, which makes the assignment of spectra a difficult task. Nevertheless, a synchronous isolation *and* cooling method has been achieved using an adiabatic expansion in a supersonic jet with helium as inert carrier gas [48, 49].

Another extremely successful method to isolate reactive radicals was developed in the fifties by G. C. PIMENTEL et al. by embedding the molecules into transparent solids – the **matrix isolation technique** [15]. Of course, the perturbation of the interesting species by the solid should be as small as possible, so rare gases are used preferably as host material. Due to their closed valence shell, the rare gases are chemically *inert*, i. e. they (at least He and Ne) do not react with the guest species. Generally, the lighter a rare gas is the smaller are the perturbations. This means that helium would be the most appropriate host material, but unfortunately helium needs pressures above 20 bar to become solid. Nevertheless, a interesting technique to isolate molecules in *nano-droplets* of liquid helium has been successfully developed recently [50, 51]. The most important properties of rare gas atoms and solids, regarding matrix isolation spectroscopy, are summarized in the table 1.2.

property	dim.	Ne	Ar	Kr	Xe
atomic diameter	Å	3.0	3.8	4.2	4.6
Lennard-Jones parameter ε	cm^{-1}	24.33	83.98	118.18	195.8
Lennard-Jones parameter σ	Å	2.76	3.41	3.62	4.03
ionization potential	eV	21.56	15.76	14.00	12.13
polarizability	$Å^3$	0.39	1.63	2.47	4.01
lattice constant ($T = 10$ K)	Å	4.467	5.313	5.647	6.132
Debye frequency ($T = 0$ K)	cm^{-1}	75	93	72	64
energy gap	eV	21.69	14.15	11.6	9.28
refractive index		1.28	1.29	1.28	1.49
melting point (P =1013 mbar)	K	24.6	83.3	115.8	161.4
sublimation temperature ($P \approx 10^{-6}$ mbar)	K	10	31	42	58
thermal conductivity ($T = 20$ K)	W/m/K	0.4	1.3	1.2	2
compressibility	10^{-10} Pa^{-1}	8.92	3.73	2.90	2.80

Table 1.2: Properties of rare gas atoms and solids, taken from [52].

To reduce guest-guest interactions, ranging from loose van-der-Waals interaction, through dipole-dipole alignment to strong hydrogen bonding, one typically uses a high dilution (guest:host $\approx 1 : 1000$) so that no electronic bands can emerge from the distinct electronic states of the guest molecules. Nevertheless, the density of guest particles in matrices is much higher than in the gas phase and therefore one can use less sensitive instruments for measurement.

Another prerequisite for potential host materials to allow spectroscopy of guests is *optical transparency.* Rare gas matrices are ideal in this respect, since the low-frequency limit is determined by the *Debye frequency*, below which photons are absorbed through excitation of phonons. On the other side of the optical spectrum, the transparency is limited by the *energy gap*, beyond which electrons can be excited from the filled *valence band* to the unoccupied *conduction band* of the host (actually, the excited electron and the hole in the valence band can form an bound state, the *exciton*, which is slightly lower in energy). In this respect, neon is again the most suitable material and it is therefore used as host material throughout this thesis.

The rare gas solid is held together by weak *van-der-Waals forces* and crystallizes therefore mostly as face centered cubic (fcc) lattice. Neon is known to have a phase transition to hexagonal closed packed (hcp) at 12K [53], and this hcp structure can be also stabilized by impurities. To avoid diffusion of guest molecules in the host material, one has to choose temperatures well below the sublimation temperature.

1.2.2 Guest-Host Interactions and Line Forms

When producing doped matrices by condensation from the gas phase, one can often observe that the guest molecule is embedded in the matrix host in different environmental arrangements, the so-called “*sites*”. Atoms or small molecules may occupy interstitial or, more frequently, substitutional lattice positions, whereas larger molecules may replace several neighboring host atoms. The guest-host interaction potential may thus have several different minima, whereby the energetically most stable site can be reached through thermal activation. This *annealing* has also the advantage that the unavoidable lattice defects heal out and therefore transition lines get sharper. Between the minima, however, there are high barriers especially for larger species so that rotation of the guest is usually not observed.

Due to the guest-host interaction, which fortunately tends to be weak in solid rare gases, matrix isolation spectroscopy shows some characteristic distinctions compared with gas phase spectroscopy concerning the position and form of spectral lines.

Although the chemical inert environment does not change drastically the electronic configuration of a guest molecule, its electronic states are slightly perturbed by weak electromagnetic fields of the nearest neighbors. This gives rise for a small shift of bands, the well known *matrix-shift,* which depends on each guest, host and site, and even the sign of the shift is difficult to predict. Generally, one can observe a red-shift of electronic transitions depending on the dipole moment of the guest and the polarizability of the host [52]. Nevertheless, the shifts of electronic niveaus in neon matrices are, even for free radicals, less then 1 % in average, as examined by JACOX in [54].

The influence of the matrix on the vibrations of the guest is more obvious: Since a guest molecule is locked up in a *cage* via van-der-Waals forces, the vibrational potential strongly increases at larger distances. This has profound influence on the dissociation behavior of molecules which is effectively hindered in matrices - only first-row atoms, and in particular hydrogen, may escape out of the cage. At small amplitudes, however, the effect of the matrix environment on the guest vibrations has little impact, and the shifts of spectroscopic constants like ω_e or $\omega_e x_e$ are also in the range of less than 1 % [55].

When embedding a molecule in a matrix, also the form of spectral lines changes characteristically compared to the form in the gas phase. Due to the coupling of the guest molecule to lattice vibrations of the host, one can observe a temperature dependent broadening of the lines. Much more interesting is the effect of *phonon side bands* (PSB) which appear for example during absorption of a single photon creating/annihilating one or several phonons in addition to the excitation of the molecule. This effect is directly analogous to the *Mößbauer effect [56],* only the nuclei are replaced here by molecules and, instead of X-rays, IR to UV photons are absorbed/emitted. There is a certain probability α that *no* additional phonons are created giving rise to a sharp (and also strong, assuming weak phonon coupling) line, the so-called *zero phonon line* (ZPL).

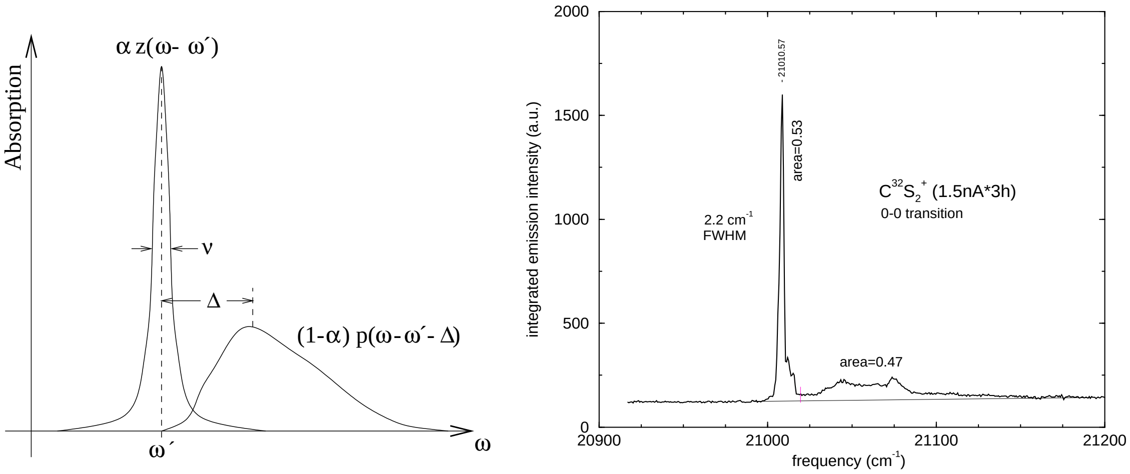

Figure 1.2: Schematic line-form of an electronic excitation of a matrix-isolated molecule (left): The sharp zero phonon line (ZPL) and the broader phonon side band (PSB). Laser excitation spectrum of mass-selected CS_2^+ ions (right) showing the actual line-form with a sharp ZPL.

Fig. 1.2 shows the characteristic form of an electronic transition with phonon coupling: The resulting line consists of a Lorentz-shaped ZPL $z(\omega)$ with area α and the PSB $p(\omega)$ with area $(1-\alpha)$ resembling a Poisson distribution. The blue-shift Δ of the maximum of the PSB relative to the ZPL is called the *Stokes shift* and usually amounts in rare gas matrices to 10-100 cm^{-1}, in close relation to the Debye frequency given in Table 1.2. With the low temperatures existing in rare gas matrices, the width of the ZPL is close to the natural line width determined by the lifetime of the excited state. The probability α that no phonon is created during absorption is well known as the *Debye-Waller factor.* The higher the temperature, the smaller is α, and for $T \to 0$, α reduces to an expressive value

$$\alpha(T=0) = \exp(-S) \tag{1.18}$$

with S equals the number of photons created at the maximum of the PSB. Thus S can be used as a measure for the strength of the coupling of phonons to the guest molecule — S >5 corresponds to “strong coupling” and leads to observation of the PSB only, but *no* ZPL, even for $T = 0$.

1.2.3 Relaxations

Due to the interaction of the vibrational and electronic states of guest molecules with the lattice vibration of the host, not only the line-forms are changed, but completely new *processes of relaxation* become allowed additional to emission of radiation. Under participation of phonons, matrix-isolated molecules may relax non-radiatively to lower states, dissipating the released energy in the lattice. The diversity of possible relaxation pathways is shown in Fig. 1.3 , with radiative (solid) and non-radiative transitions (dashed arrows) drawn into a diagram of energy levels.

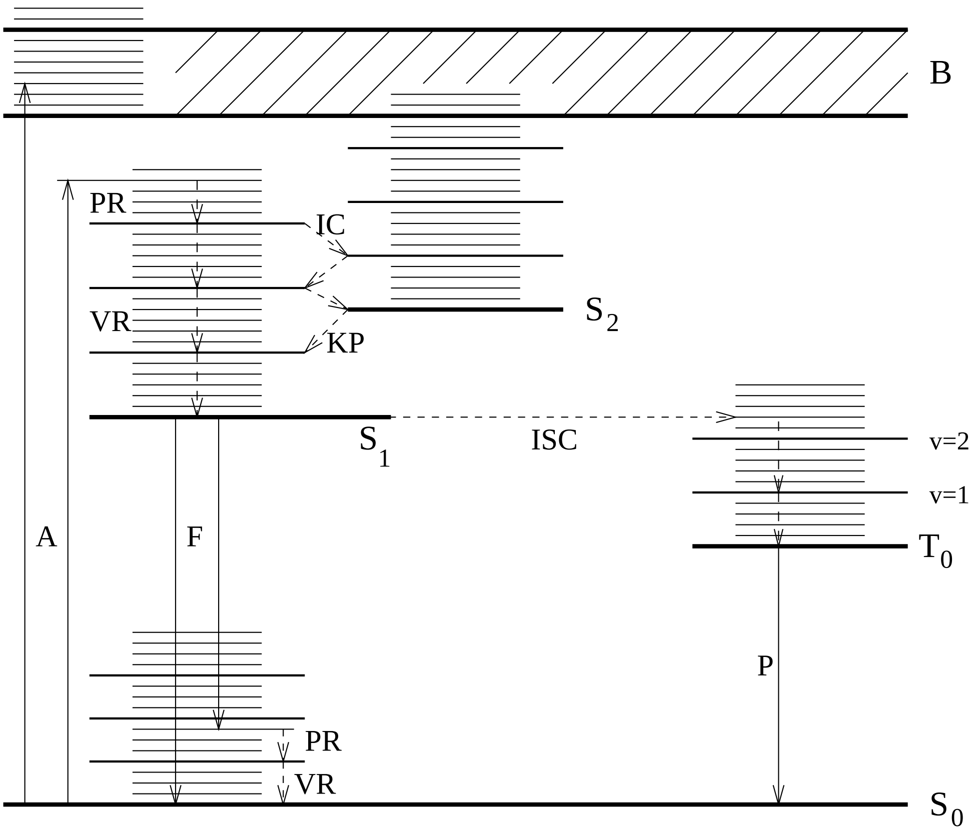

Figure 1.3: Schematic energy levels of a matrix-isolated molecule with different processes of relaxations (non-radiative processes are dashed): S_i, T_i: singlet and triplet states of the guest, ν: vibrations of the guest, B: band of electronic states of the host, $\equiv$: quasi-continuous lattice vibrations of the host, IC: internal conversion, ISC: inter-system crossing, VR: vibrational relaxation, PR: phonon relaxation, KP: cascade process made of several ICs, A: absorption, F: fluorescence, P: phosphorescence

Vibrational relaxations of matrix-isolated molecules depend heavily on the density of vibrational states, i. e. the distances between the vibrational niveaus. For vibronically excited large molecules with a high density of states, one obtains fast relaxation into the vibrational groundstate of an electronic state, from which the most intense emission is observed. Small molecules, on the other hand, with vibrational distances $>$ 500-1000 cm^{-1}, can relax vibrationally only via a *multi-phonon process*. Theoretically, one obtains for diatomic molecules an exponential decrease in the rate of relaxation R with the order $N = \omega_{molecule}/\omega_{phonon}$ of the multi-phonon process [57]:

$$R \propto \exp(-\frac{\omega_{molecule}}{\omega_{phonon}}) \tag{1.19}$$

This **energy gap law**, with $\omega_{phonon} \approx \omega_{Debye} \approx 50 - 100$ cm^{-1}, was later confirmed experimentally for several diatomics [58, 59].

In addition to the transformation of vibrational energy into phonons, the transformation into quanta of rotations can be observed provided that rotation is allowed at all (for example NH [60]). Another interesting process is the inter-molecular, phonon-assisted transfer of vibrational energy between guest molecules, which may occur resonant, as well as non-resonant with the excess energy dissipated by the lattice [61, 62].

Electronic relaxations, as for example *internal conversion* and *inter-system crossing*, proceed in the matrix environment also much more effective than in the gas phase. Particularly the internal conversion between two states of the same spin multiplet intensifies strongly, when a vibrational niveau of another electronic states lies in the proximity of the original electronic state. Also the probability of the spin-forbidden inter-system crossing increases drastically in matrices. We thus were able to observe the strong phosphorescence a $^3\Pi_u \rightarrow$ X $^1\Pi_g$ of the C_3 radical after pumping of A $^1\Pi_u \leftarrow$ X $^1\Pi_g$ and populating the a state via ISC [63].

When two or more vibrational manifolds of different electronic states are interlocked with each other, cascade-like processes may occur in competition with vibrational relaxation. As one can see in Fig. 1.3 (KP), the excitation zig-zags between the vibrational levels of two electronic states, and the rates are governed by phonon Franck-Condon factors and the energy gap law. This *cascade process* was best studied in the case of the CN radical [64], and it can occur even for spin- and parity-forbidden transitions [65, 66] since selection rules are often significantly weakened in matrices.

Chapter 2

Experimental Techniques

In this chapter, the performance of a matrix-isolation experiment, as well as its coupling with mass spectrometry techniques, are described in detail. First of all, the basic methods of measurement ranging from a brief introduction of the Fourier-transform spectrometer to the different procedures to obtain optical spectra are presented. Then the particle sources used in this thesis to produce the species of interest are described and characterized. Starting from the old experimental setup, the new mass-selection, i. e. the quadrupole mass filter and the attached ion optics, and its coupling to the old setup is discussed. Additionally, a short review of studies using mass-selection is presented and finally, the process of deposition of mass-selected ions is examined.

2.1 Methods of Measurement

2.1.1 The Fourier-Transform Spectrometer

Central to our matrix-isolation experiment is the *spectrometer* analyzing the radiation emitted or absorbed from the matrix, in our case a BRUKER IFS 120 HR Fourier-Transform Spectrometer. In principle, it works like a MICHELSON *interferometer* consisting of a beam splitter, one fixed and one movable mirror and a detector measuring the signal intensity in dependence of the position of the movable mirror (see Fig. 2.1).

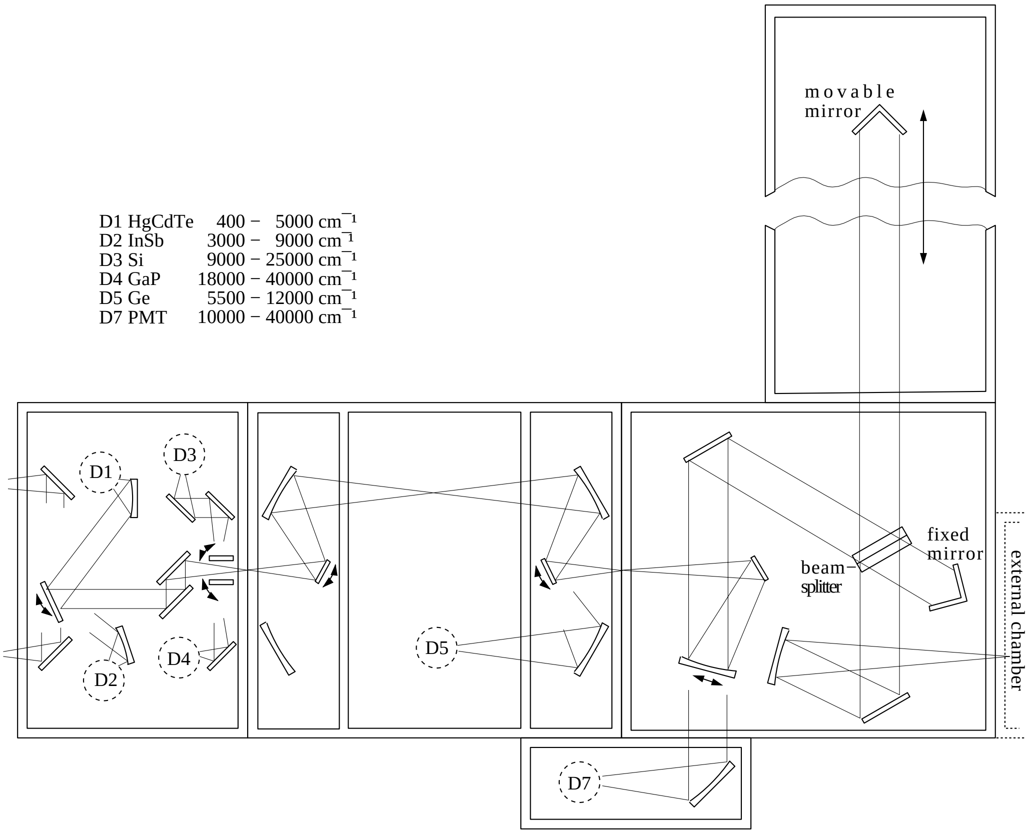

Figure 2.1: Schematic drawing of the IFS 120 HR Fourier-Transform-Spectrometer. Depending on the spectral range, one of four different beam splitters splits the incident light exactly 50:50. One can also choose between 6 different detectors.

Several movable mirrors in the external chamber attached to the spectrometer can choose between light from either internal sources or from three different experiments surrounding this chamber (RMC cryostat with 4.2K, APD (12K) and LEYBOLD (7K)). From there the light is focused onto a selectable aperture and coupled into the interferometer. The light split into two equally intense beams interferes with itself and a detector measures the intensity $I(x)$ of the reunited light as a function of the optical path difference x between the two mirrors.

The position of the movable mirror is measured interferometrically with the aid of a frequency-stabilized HeNe laser beam coaxial to the original light beam. Each time the HeNe laser interferes destructively, the signal of the detector is sampled with 16 bit resolution. The *interferogram* obtained in this way is then transformed digitally into a *spectrum* $S(\nu)$ via *Fast-Fourier-Transformation* (FFT), with the resulting spectra reaching from 0 to the frequency $\nu_{HeNe} = 15797.989$ cm^{-1} of the orange-red line of neon (NYQUIST theorem):

$$S(k\frac{1}{N\Delta x}) = \sum_{n=0}^{N-1} I(n \cdot \Delta x)\exp(2\pi i\frac{nk}{N}) \tag{2.1}$$

To measure absorptions up to the UV range, the sampling frequency is doubled or quadruplicated electronically by a phase-locked loop circuit.

The resolution of the interferometer is determined by the maximum optical path difference ΔL of the two interfering beams. With $\Delta L = 6$ m, our spectrometer reaches a resolution of

$$\Delta\nu = \frac{1}{N\Delta x} = \frac{1}{\Delta L} = 0.0016\,\mathrm{cm}^{-1}$$

at maximum. Since the line-widths of matrix-isolated molecules are usually not sharper than ≈ 1 cm^{-1} (optical transitions, IR vibrations are sharper), the spectra are measured with reduced resolution of 0.1-0.5 cm^{-1} (0.06 cm^{-1} for IR spectra). In general, FT interferometers have several advantages compared to conventional, dispersive spectrometers, as for example grating monochromators:

- Connes: Due to the calibration with the stabilized HeNe laser, an absolute frequency precision of 0.001 cm^{-1} is achieved.
- Jaquinot: Interferometers use circular apertures in contrast to the slits of monochromators ⇒ higher intensity, less noise.
- Fellget: Each point of the interferogram contains all $N = \nu_{HeNe}/\Delta\nu$ frequencies of the spectrum; monochromators measure these frequencies sequentially ⇒ signal/noise is a factor $\sqrt{N}$ better.

Despite all these advantages, one has to adjust carefully the aperture, optical filters and the electronic filters and amplifiers to be able to detect weak emissions in proximity to strong ones, although the analog-digital converter is always operated close to the saturation limit.

2.1.2 Absorption Spectra

Absorption spectra can be measured in the whole range from 500-30000 cm^{-1} using different combinations of broadband light sources (like glow bar (IR) and tungsten lamps), beam splitters (KBr, CaF_2, quartz Vis and quartz UV) and detectors (MCT, InSb, Si and GaP diodes). First of all, one has to measure a reference spectrum $S_0(\nu)$ containing the multiplied frequency responses of light source, mirrors, windows and the detector. After depositing the matrix, a second spectrum $S(\nu)$ is then measured with the light passing twice through the matrix (see Fig. 2.9). According to the **Beer-Lambert law**, one obtains for the absorption

$$A(\nu) = -\log_{10} \frac{S(\nu)}{S_0(\nu)} = c \cdot l \cdot \varepsilon(\nu) \tag{2.2}$$

where l is the optical thickness of the matrix, c the concentration of the absorbing species and $\varepsilon(\nu)$ the molar coefficient of absorption. In the infrared range, the spectrometer has to be evacuated and the remaining optical path flushed with dry nitrogen to avoid disturbing absorptions due to gaseous, IR-active carbon dioxide and water vapor.

2.1.3 Laser Excitation Spectra

The signal/noise ratio of absorption spectra is determined by the subtraction of two almost identical, but slightly noisy values resulting in a value dominated by noise. Therefore it is better to use tunable lasers with a sharp frequency instead of broadband light sources and to measure *not* the transmitted light, but the red-shifted radiation which is reemitted by the absorber into 4π steradian and integrated over the detector bandwidth (which is usually reduced by optical cut-off filters). This procedure, which is shown schematically in Fig. 2.2, has several advantages:

- the total power of the light source is concentrated into a small frequency range

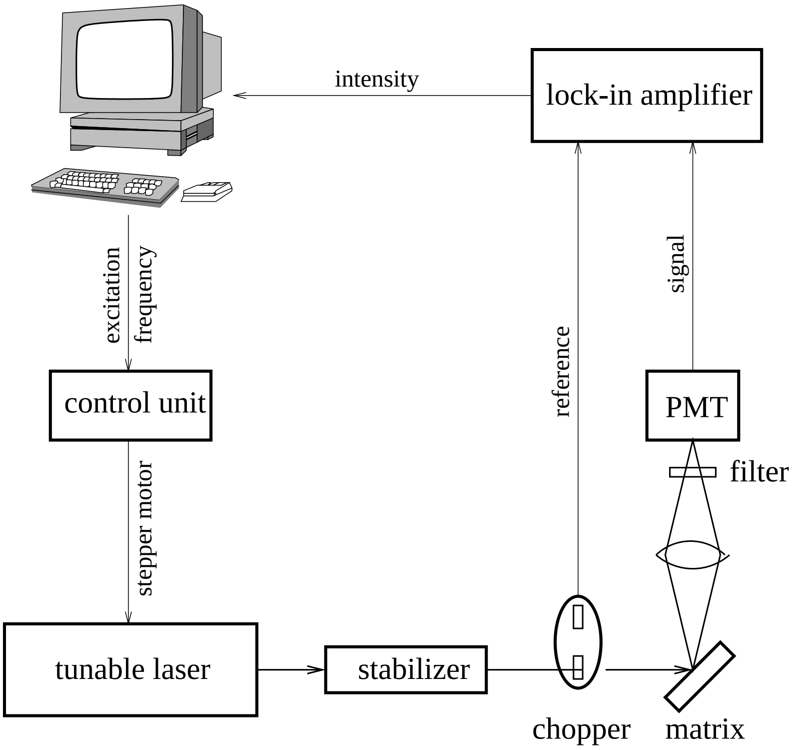

Figure 2.2: Schematic drawing of the setup to measure laser excitation spectra.

- to detect the laser-induced fluorescence, one can use the extremely sensitive photomultiplier and liquid nitrogen cooled germanium detectors
- instead of measuring weak direct currents, one can use the more sensitive *lock-in technique*

This lock-in method works as follows: A computer controlled stepper motor turns the birefringent filter determining the frequency of the tunable laser. The intensity-stabilized laser beam is then modulated by a chopper, focused onto the matrix and the internal parabolic mirror guides the fluorescence light after passing optical filters to the detector. Using the reference signal from the chopper, the lock-in amplifier filters from the detector signal the interesting frequency f_{mod} with a bandwidth of $\approx$ 1 Hz eliminating most of the broadband $1/f$ shot noise. This combination of laser excitation and lock-in technique is easily 3-4 orders of magnitude more sensitive compared to visible absorption and it is therefore preferably used in this thesis to detect the weak amounts of mass-selected ions.

2.1.4 Laser-Induced Fluorescence Spectra (LIF)

In contrast to absorption spectra measuring all species found in the matrix synchronously, *laser-induced fluorescence* (LIF) allows to excite selectively one single species. An allowed electronic transition obtained by absorption or laser excitation spectra is resonantly excited by a tunable laser, and the induced fluorescence is analyzed by the FT-spectrometer. This fluorescence gives additional, sometimes complementary, information about the lower electronic states reached by allowed electronic transitions from the excited state. For example IR-inactive, symmetric vibrations cannot be detected in absorption spectra, but these symmetric modes appear in the LIF spectrum starting from an excited state. Thus LIF is an important aid to identify and to characterize molecules spectroscopically.

type of laser	dye/medium	frequency range [cm^{-1}]
ring laser[a]	Ti:sapphire	9700-14300
standing wave laser[b]	DCM	14300-16000
“	Rhodamine 6G	16000-17600
“	Rhodamine 110	17000-18900
“	Coumarin 6	18200-19100
ring laser[c]	Coumarin 102	19300-21700
“	Stilbene 3	21500-24400
“	Stilbene 1	23800-25000
ring laser[a] with SHG	Ti:sapphire	24000-27400

---

[a] COHERENT 899-21

[b] COHERENT 589-01

[c] COHERENT 899-01, UV pumped

Table 2.1: Available laser systems

To excite molecules in matrices, the following dye and solid-state laser systems pumped by a 5 W or a 20 W (multi-line visible, 6 W multi-line UV) Ar^+-ion laser (COHERENT Innova 70 and Innova 200, respectively) and summarized in Table 2.1 are available. As one can see, almost the complete visible range, as well as the near infrared, is covered by our lasers.

The intensity stabilized laser beam with a typical power of 10 to 100 mW is focused onto the matrix (spot size $\approx$ 1 mm), and the resulting LIF is collected by the internal parabolic mirror and coupled into the FT spectrometer. Direct laser reflections into the spectrometer must be avoided and, additionally, the dominant scattering light, as well as the internal HeNe laser, must be reduced with appropriate optical notch and cut-off filters (low pass) to avoid overloading of the sensitive detectors.

2.2 Sources

Using highly optimized particle sources is crucial for successful experiments in spectroscopy. In spite of the availability of sensitive methods, like laser excitation or laser-induced fluorescence, it turns out that it is frequently very difficult to produce enough amounts of the interesting species to detect and characterize it. This is especially important, when combining mass spectrometry with optical spectroscopy, where one has to detect as small amounts as $\approx$0.1 nmol of the interesting species.

To produce the transients, which are in the focus of interest in our laboratory, several conventional methods are available, for example:

- photolysis [67, 68]
- redox reactions [69]
- reactions in combustion flames[1]
- electrical discharge [20]

In this section, the sources are described which were used to produce the neutral and ionic molecules characterized in this thesis, in particular the laser vaporization, microwave discharge and electron impact (EI) sources.

2.2.1 Laser Vaporization

To produce clusters of, for example, transitions metals it is necessary to vaporize the metal. Refractory solids, however, like tungsten or boron nitride can only be vaporized by very high temperatures of over 3000 K, and such temperatures can be conveniently produced using pulsed lasers. The technique of pulsed laser vaporization has been developed and used in our laboratory since 1980 [70, 71], when BONDYBEY and ENGLISH presented the first fluorescence spectrum of Pb_2 by laser vaporization of solid lead. At the same time SMALLEY et al. examined small metal clusters in a molecular beam which were also produced by laser vaporization [72]. This

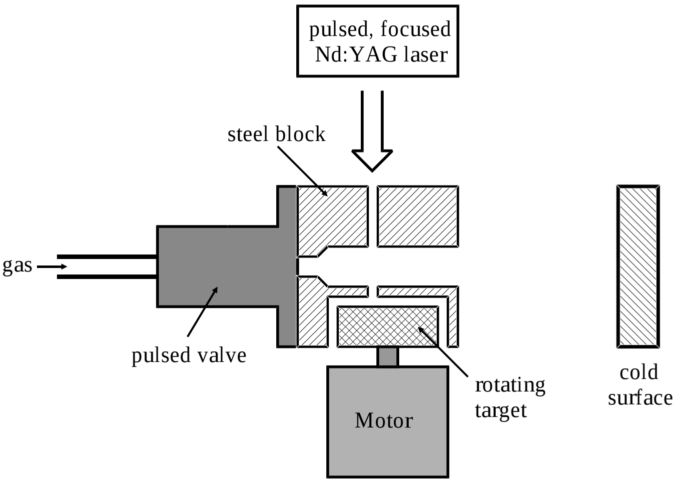

Figure 2.3: The laser vaporization source

method, which was used in the scope of this thesis to vaporize tungsten, trap the tungsten oxides in a solid neon matrix and examine their spectroscopy, will be described briefly in this section.

Fig. 2.3 shows schematically the structure of the laser vaporization unit used in our laboratory; it is described in detail also in [73]. The rotating sample material is vaporized by a pulse of frequency-doubled, focused Nd:YAG laser light (532 nm, 4 ns, $\approx$20 mJ, 10 Hz) which produces a small "plasma plume" on the surface of the target. This plasma is characterized by temperatures of $\approx 10^4$ K and particle densities of $10^{18} - 10^{19}$ cm^{-3} [74, 75]. The laser pulses are synchronized with the opening of a pulsed valve (General Valve, opening time $\approx$0.1 ms) controlling the flow of a carrier gas (usually neon). The laser-induced plasma is swept by the gas pulse, flows through the channel and expands into the vacuum, where the gas cools down in a supersonic expansion allowing the clustering of single atoms [76]. After $\approx$ 3 cm of free expansion, the gas beam is frozen out at the cold surface at $\approx 7 - 8$ K producing matrices of typical 0.1 mm thickness.

Using pure rare gases as carrier, one obtains atoms, ions or cluster of the vaporized substance. Adding reactive gases to the inert carrier gas allows reactions with the plasma and new products are formed. This method was used to produce the tungsten oxides characterized in this thesis by adding 0.2% of oxygen to the neon.

2.2.2 The Microwave Discharge Ion Source

For experiments using the mass-selection a microwave discharge ion source was used. Initial experiments with the available pulsed gas discharge source (named "Putzi" [20]) showed that the average ion current ($\approx$10 pA) was to low to detect anything spectroscopically. It also turned out that this "Putzi" source did not operate satisfactory in cw mode, although it produced higher current in this mode. A breakthrough was then the employment of a cw microwave discharge source: Using CS_2 as precursor gas, we were able to detect in our lab the first laser excitation spectrum of a mass-selected species, the CS_2^+ cation!

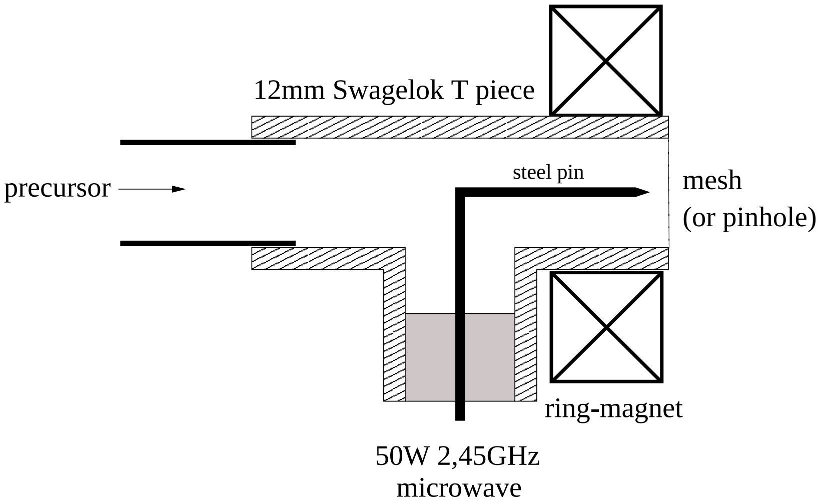

Figure 2.4: Schematic diagram of the microwave discharge source

Fig. 2.4 shows the microwave ion source consisting mainly of a simple 12 mm Swagelok T-piece, with the precursor gas flowing through the collinear sections, and with 50 W of 2.45 GHz microwave power being applied to a needle electrode via the perpendicular arm. The peak of the pin is located 0.2 mm away from the center of a 0.5 mm pinhole. This pinhole allows high enough pressure in the T piece to ignite the discharge, although the pressure in the source chamber was only around $10^{-4} - 10^{-2}$ mbar.

Unfortunately it turned out that, when using carbon containing precursors, the pinhole gets plugged sooner or later by soot. That problem was solved by using a steel mesh instead of the pinhole, requiring a much higher pressure (up to two orders of magnitude) in the source chamber to operate continously. Additionally, the consumption of precursor substance also increased about two orders of magnitude. To overcome this, a ring-shaped magnet was placed around the discharge zone to confine the charged species (mainly electrons) on circular orbits. This allowed to operate the source - once ignited by a Tesla transformer - continously for several hours at quite low pressures of $10^{-4} - 10^{-3}$ mbar in the source chamber with mass-selected ion currents reaching up to 1-2 nA.

This source could be further optimized by changing the geometry of the source to be in resonance with the microwave radiation (now 80% of the applied power are reflected back to the generator). The second enhancement would be the usage of a variable magnetic field to adjust the corresponding cyclotron frequency of the electrons in resonance with the microwave frequency of 2.45 GHz.

The discharge products from the source held at +20 to +40 V (determining the kinetic energy of the ions) are then accelerated towards a 2 mm skimmer held at -20 V yielding a total ion current of up to 100-1000 nA measured at the first Faraday cup F1. A photograph of this ion source using neon as gas is shown in Fig. 2.5.

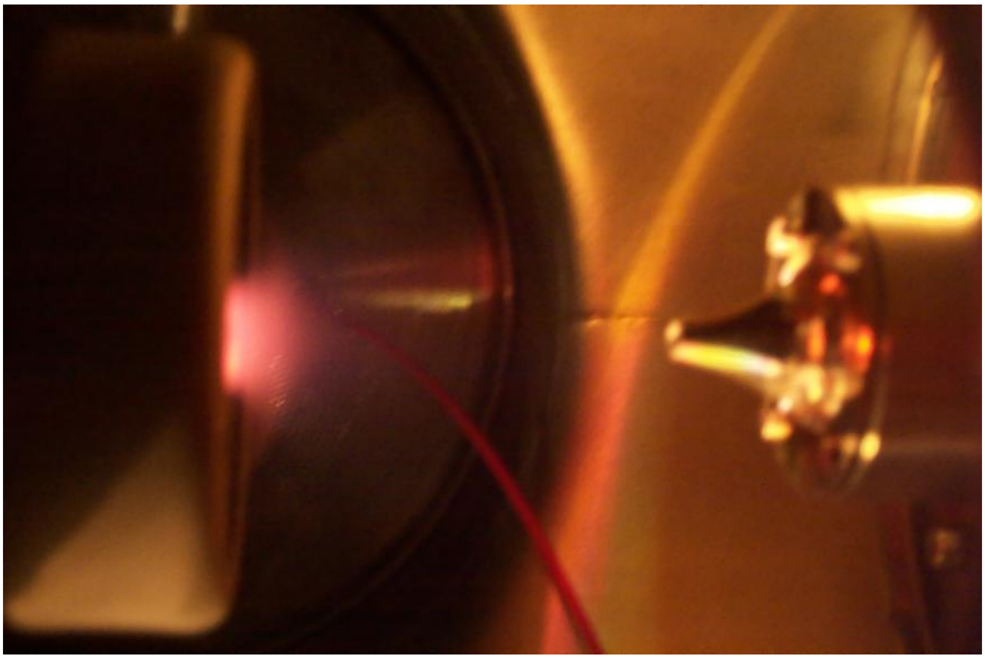

Figure 2.5: Photograph of the source chamber showing the microwave discharge ion source in operation (left) and the skimmer (right) towards which the ions are accelerated.

2.2.3 The Electron-Impact (EI) Ion Source

Another ion source used in this work is the electron-impact ion source which has the advantage that it does not need a continuous discharge to produce ions and therefore it consumes much less precursor substance while yielding even higher ion current as other discharge sources. It was developed in our laboratory within the scope of a “13-Tage Praktikum” and resembles standard EI sources used for example in commercial rest gas analyzers (RGAs) [77, 78].

The setup of our EI source is shown schematically in Fig. 2.6(a) and the electrostatic potential applying optimized voltages is presented in part (b). Electrons emitted from a tungsten filament mounted between the casing and the cage (a stainless steel mesh) and held at -50 V are accelerated towards the cage kept at +40 V. They are confined within the casing kept at -70 V as can be seen in Fig. 2.6(c) where the trajectories of a bunch of electrons are shown. When traversing the cage area with kinetic energy of 90 eV, they occasionally hit a molecule of the precursor gas leading to ionization and/or fragmentation of the molecule. The cross section for ionization is at maximum for a kinetic energy in the range 70-100 eV. The positive ions then “feel” the negative potential of the extraction electrode kept at the same potential as the casing and are accelerated towards the skimmer. Fig. 2.6(d) shows that the ions produced in the cage are completely extracted and well focused by a einzel-lens (at -300 V) onto the entrance hole of the skimmer kept at -30V. All simulations of ion optics were done with the SIMION 6.0 program.

Compared to the microwave discharge source, the EI source shows several important advantages:

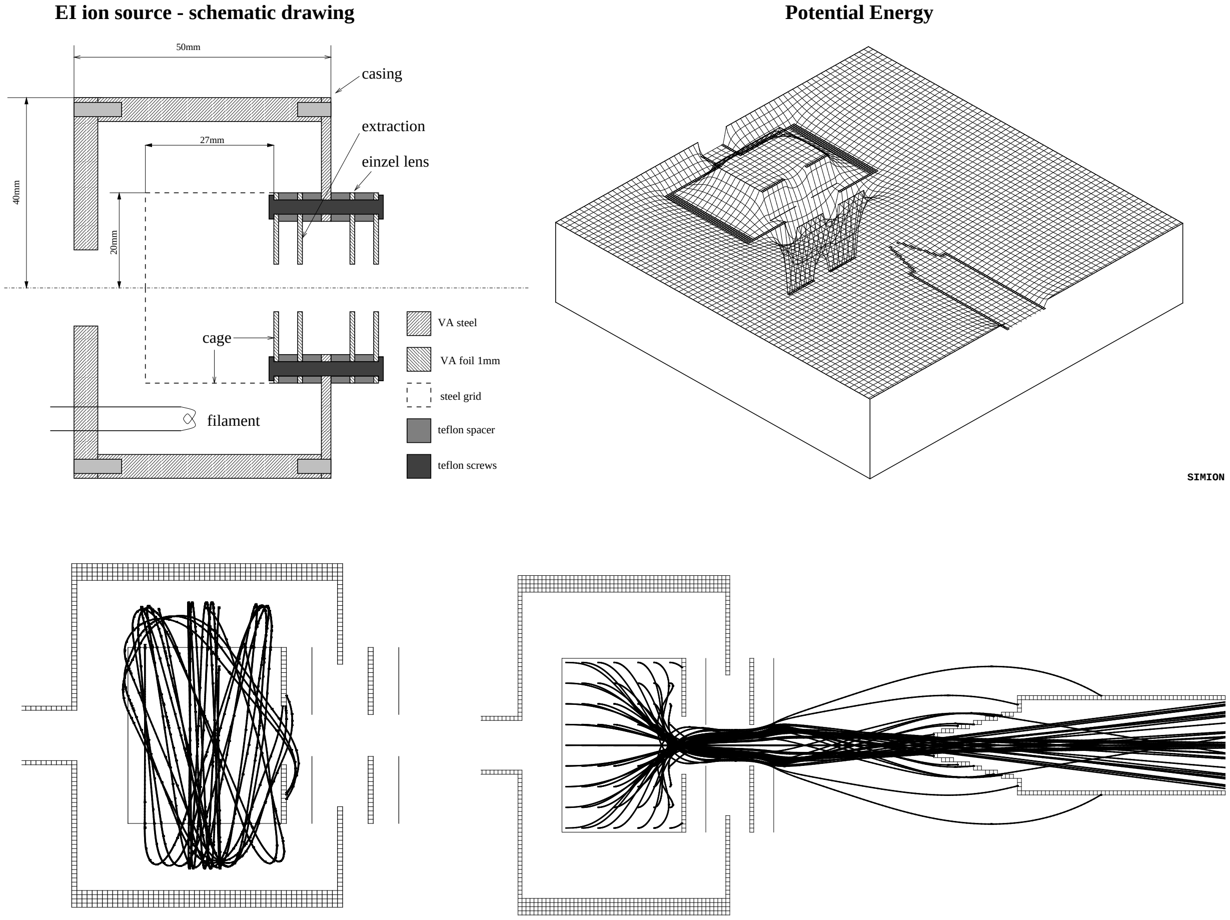

Figure 2.6: The EI ion source. From top left to bottom right: (a) schematic drawing, (b) view of the electrostatic potential, (c) trajectories of a bunch of electrons and (d) trajectories of ions produced in the cage and accelerated towards the skimmer

- low precursor substance consumption
- less pressure in the source chamber ($10^{-7} - 10^{-5}$ mbar) $\Rightarrow$
  the 2 mm skimmer can be removed completely, leading to a 2 cm hole and therefore higher ion currents
- the source can be used as a rest gas analyzer to check the vacuum in the source chamber
- ion currents up to 20 nA (mass-selected) !

Due to the low pressure in the source, which leads to a very small collision rate, this source produces mainly the mother ion and fragment ions, but only few new products are formed by reactions during collisions.

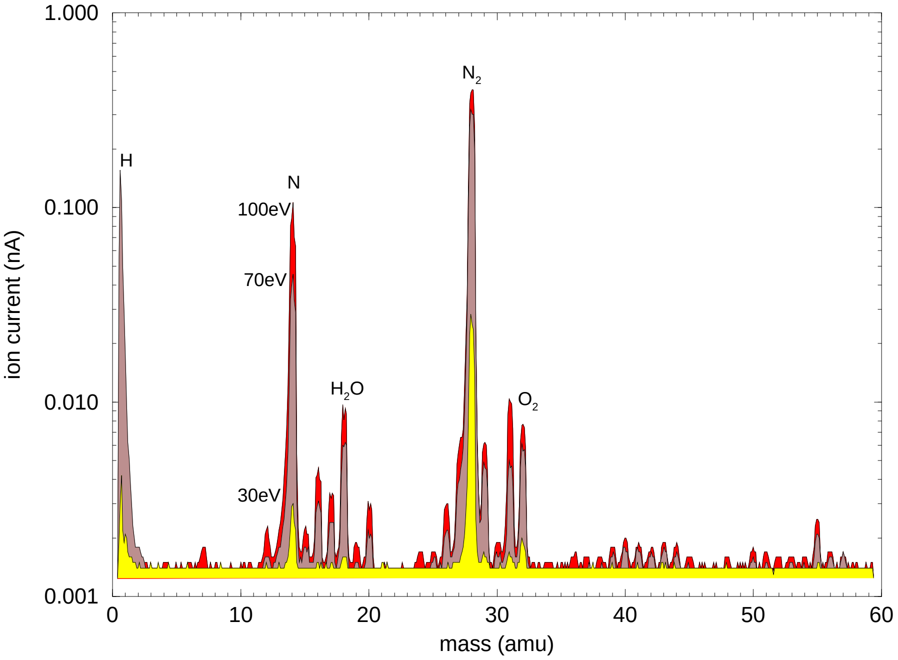

Figure 2.7: The dependence of the EI source ion production on the kinetic energy of the electrons (= 30, 70 and 100 eV) using N_2 (and a rest of air).

Characterization of the EI source.

The dependence of the EI source ion yield on the kinetic energy of the ionizing electrons, which is determined by the filament voltage, is shown in Fig. 2.7 using nitrogen contaminated by a small amount of air. As one can clearly see, the yield of N_2^+ (IP(N_2) = 15.6 eV) is quite independent using energies in the range 70-100 eV, but the ionization cross section decreases tremendously when lowering the energy to 30 eV. Producing the N^+ cation costs additional dissociation energy (8 eV) so that a kinetic energy of 30 eV is just above the threshold to produce N^+ (at 14 amu). Energetically most expensive is the production of N^{2+} ($D_0(N_2) + IP(N) + IP(N^+) = 8.6 + 14.5 + 29.6 = 52.7$ eV), and the kinetic energy of the electrons must be at least 100 eV to detect this doubly charged species at m$=$ 7 amu.

The pressure dependence of the EI source is shown in Fig. 2.8 using for example H_2 as precursor substance and a kinetic energy of 90 eV for the electrons. While the pressure measured in the source chamber was decreased in four steps from 10^{-4} to 10^{-5} mbar, the proton and H_2^+ yield decreases by a factor of $\approx$ 30, whereas the production of H_3^+ is reduced by about three orders of magnitude. This clearly shows the strong pressure dependence of the H_3^+ production rate which is determined by the collision rate (proportional p^2) in the ion source.

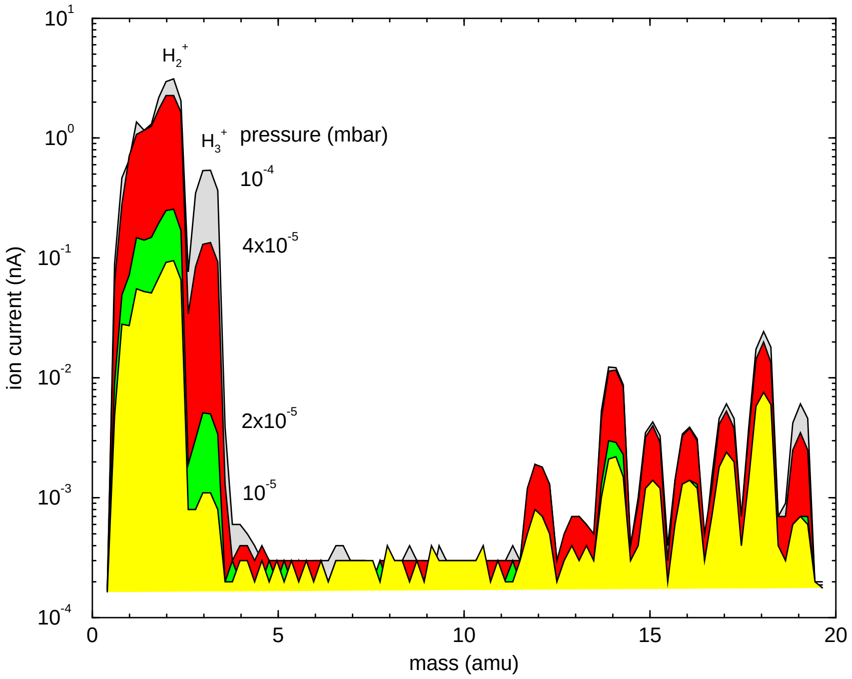

Figure 2.8: The dependence of the EI source ion yield on the precursor (here H_2) background pressure. One can clearly see the p^3 dependence of the H_3^+ ion yield.

2.3 The Old Apparatus

The old experimental setup, used in this thesis to examine the tungsten oxides and the new rare gas compounds, is described briefly in this section, but more detailed descriptions are given in [73, 21]. After removing the source flange attached to this old setup, it serves also as cryostat for the new mass-selection experiment.

Central to matrix-isolation experiments are the cryostat and the surrounding vacuum chamber. In our setup, shown schematically in Fig. 2.9, we use a closed-cycle LEYBOLD RGD 5/100 refrigerator to cool the silver-coated copper substrate which serves as cold surface for matrix deposition down to 6.8-7.8 K. These two temperatures are measured by two Si-diodes, the colder one mounted directly at the cold finger of the cryostat and the other one mounted at the substrate holder, diametrical to the first one. The real temperature of the substrate lies between these two values, and it can be adjusted by a heater controlled by a LEYBOLD LTC 60. To lower the temperature, both cold finger and the substrate holder are surrounded by a radiation shield. The whole cryostat and the attached cold surface is mounted rotatable around the vertical axis to allow deposition of matrices from one direction (here from the left) and to allow optical access from the other one.

The vacuum chamber consists of standard ISO-K vacuum parts and is pumped by a 240 l/s turbo pump (BALZERS TPH240 with pre-pump DUO1.5a) reaching a final pressure of $\approx$

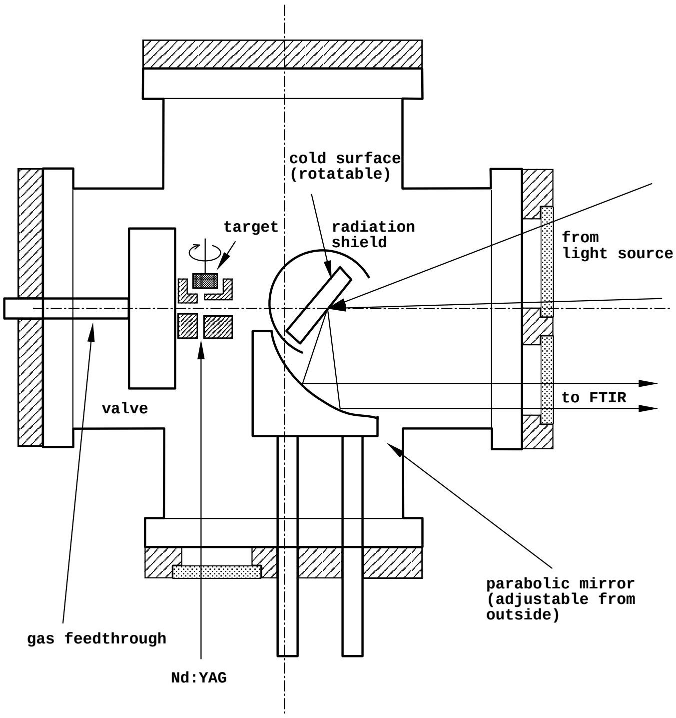

Figure 2.9: Horizontal cut through the vacuum chamber of the cryostat. One can see the optical path for the measurement of absorption spectra using an internal parabolic mirror and, to the left, the attached laser vaporization source.

2×10^{-6} mbar (without cryo pump, $\approx 2 \times 10^{-7}$ mbar with running cryostat). A gas mixing system with an absolute pressure gauge is attached to the chamber to purify gaseous precursor substances by pump-freeze cycles and to mix them later on with the matrix rare gas in arbitrary ratios. Modified blind flanges attached to the central 6-way cross (DN100 ISO-K) serve mainly as holder for the internal parabolic mirror and for different sources and allow optical access to the matrix via KCl salt windows. The flange which holds the source can be replaced easily to use different sources like pulsed discharge, laser vaporization or dual sources to produce layered sandwich matrices. Using rotatable linear feedthroughs, one can adjust the internal mirror to maximize the amount of light reaching the FTIR spectrometer.

2.4 The Mass-Selection

2.4.1 General

Absorption spectra obtained with the old setup without mass-selection frequently showed a lot of new, unknown spectral features whose carrier(s) is(are) difficult to identify. In particular using a discharge source with carbon-rich precursors producing all kind of carbon compounds resulted in rich spectra which can only be interpreted with the help of tedious and time-consuming correlation or isotopical substitution experiments [79].

One possibility to remedy this problem is the introduction of a mass filter between the source, which produces the different species, and the matrix, where the species are spectroscopically characterized. Introducing this so-called *mass-selection stage* has several advantages compared with the old, conventional setup:

1. Real-time optimization of the source and the ion optics:
   With the old setup, an optimization cycle consisting of matrix deposition and spectroscopical investigation takes at least one hour. The new mass-selection setup, on the other hand, permits the real-time optimization of 10-20 parameters which determin the ion yield by simply measuring the ion current after mass-selection.

2. Avoidance of disturbing impurities:
   Using for example carbon and nitrogen containing precursors with the discharge source always resulted in the production of the CN radical. It can be non-resonantly excited in a broad spectral range disturbing the emission spectra of the desired species. Including a mass filter furthermore reduces the guest-guest interactions by simple discrimination of the unwanted species.

3. The mass information:
   Of course, knowing the mass of a species facilitates its identification!

Besides these apparent advantages, the mass-selection shows also some more or less severe disadvantages:

1. Losses of ion current:
   - only 5-30 % transmission through mass filter, depending on the resolution
   - additional losses by passage through three small apertures
2. When using too high kinetic energy:
   - Problem of fragmentation
   - Matrix damage during deposition of the ion beam

The latter problems will be discussed in detail in section 2.4.5.

To filter masses, several different methods are available. Generally the dispersive mass filters can be divided in spacial and in temporal methods:

1. Spacial mass filters:
   - WIEN filter: $\mathbf{E}\perp\mathbf{B}$, resolution $\Delta m/m$ from 10^{-2} to 10^{-3}
   - MATTAUCH mass spectrometer (resolution 10^{-7})

2. Temporal filters

    - Time-of-flight spectrometer (TOF)
    - current RETOFs with resolution up to 10^{-4}

Besides these dispersive methods there exist also some filtering techniques which do not fit in the above scheme, as for example ion cyclotron resonance (ICR, resolution 10^{-6}) and quadrupole mass filters with resolution up to 10^{-3}; the principle of operation of the latter is shown in detail in section 2.4.3.

By using temporal mass filters, which allow only pulsed operation resulting in diminished transmission, one can obtain a complete mass spectrum per shot. These filters are very suitable for pulsed sources, but to use them in combination with continuous sources, one has to sacrify a large part of the average ion current. For continuous operation, on the other hand, one can use either a spacial filter or a quadrupole mass filter. We decided to use a quadrupole mass spectrometer (QMS), since it does not have mechanical parts (slits) and it is used as standard mass filter in commercial rest gas analyzers and is therefore available for a reasonable price. Furthermore a QMS allows easy computer-controlled operation in both continuous and pulsed mode.

Mass-Selection Studies in Rare Gas Matrices

The first successful studies of mass-selected species in the matrix were reported some ten years ago almost simultaneously by several groups. RIVOAL and coworkers, have modified an apparatus in Lausanne originally intended for gas phase cluster studies, and interfaced it to a cryostat for matrix spectroscopy [80, 22]. In the earliest experiments aimed at deposition of mass selected Ag_3^+ and Ni_3^+ clusters the currents were apparently too low for optical detection, but over the following few years the apparatus was steadily improved by changing the experimental parameters and source geometry [81, 82]. The cluster ions were produced by means of sputtering with a 10 mA primary beam of 20 keV Kr^+ ions, analyzed in a quadrupole mass filter and deposited with krypton matrix gas on a sapphire window. The ions were directed to the window with the help of an accelerating field and an electrostatic lens, and after deposition neutralized by electrons from a tungsten filament. While in the early experiments fragmentation presented some problem, after further refinements it was possible to observe the UV absorption spectra of neutral silver clusters up to n=39 [83, 84].

LINDSAY, one of the investigators of the above study, LOMBARDI, and coworkers then constructed a new apparatus at CCNY (City College of New York), employing first a Wien velocity filter in place of the quadrupole mass spectrometer. Even though this filter had the disadvantage of relatively low mass resolution, this represented no problem in studies aimed at M_n^+ metal clusters, where only clusters with varying values of n have to be separated. They are using the same CORDIS ion sputter source as RIVOAL, HARBICH et al. Over the following years, these workers have reported series of interesting studies of the absorption and resonance Raman spectra of numerous metal dimers and small clusters, including V_2 [85], W_2 [86], Ta_2 [87], Hf_2 [88], Re_2 [89], Co_2 [90], Zr_3 [91], Ta_4 [92], Ni_3 [93], Nb_3 [94], Rh_2 [95], Ru_2 [96], Hf_3 [97] and Pt_2 [98].

Another apparatus for mass selected studies was developed at Michigan State University by LEROI and ALLISON, who used a quadrupole filter from a modified residual gas analyser [77]. In their early studies they were able to reproduce LIF spectrum of the CS_2^+ ion in solid argon, but only the parent carbon disulfide and diatomic CS could be detected in the infrared, an observation which the authors explained in terms of neutralization of the ion accompanied by fragmentation to CS + S [25]. These authors have more recently reported that the ion yield could be greatly enhanced by adding small quantities (0.1 %) of CO_2 to the matrix gas, which then traps the electrons and suppresses the ion-electron recombination [99]. They then succeeded in recording the infrared spectra of several ions, including CF_3^+ [100] and CS_2^+ [101] and CO_2^+ [99] in solid argon and neon matrices.

A whole series of highly successful investigations of mass selected species in the matrix is due to MAIER and coworkers, who used the technique to investigate numerous carbon chain species, which are of considerable importance in astrophysics and for interstellar chemistry. They generate the carbon chain molecules in a hot cathode discharge source, using suitable precursor molecules, usually acetylene or its derivatives diluted by helium or argon [102, 23, 103]. The accelerated ions are focussed by electrostatic lenses, and after selection in a quadrupole mass filter they are guided onto the matrix surface. The deposited mass selected species were then investigated in solid neon matrices by visible or UV absorption spectroscopy using a wave-guide absorption technique. The spectra obtained in this way for the HC_kH^+ [104, 105], $HC_{2n}CN^+$, and $NCC_{2n}CN^+$ [106] ions provide information complementary to our LIF studies on the same systems [107, 108]. Recently, they used an electron impact source to produce the anions of the above mentioned linear chain molecules. After characterization of the anions, an electron was photo-detached and the corresponding neutral species have been studied [109, 110]. They also used sputtering of a graphite target to generate and deposit ionic $C_n^{\pm}$ cluster species, and record their spectra. Particularly exciting are their observations and assignment of the electronic absorption spectra of neutral and anionic carbon clusters, C_n, and C_n^-[111, 112, 113]. In their spectra of the anions they detected a whole series of close coincidences with frequencies of the so called diffuse interstellar bands, which provided first really solid evidence for solving the long-standing mystery of their origin [114, 115].

Quite recently, MOSKOVITS and coworkers started to use a mass-selection apparatus similar to LINDSAY's setup to study transition metal clusters. In the beginning, they examined the direct synthesis of metal cluster complexes by deposition of mass-selected iron clusters with excess CO as ligand [116]. Using resonance raman spectroscopy, they were later able to characterize Ag_5 [117], Ag_3 and Fe_3 [118] in solid argon.

The Setup of the New Mass-Selection Experiment

The apparatus constructed in our laboratory is similar to MAIER's successful setup [102] - a schematic drawing of our setup is shown in Fig. 2.10. We have also decided to use a quadrupole mass filter, which unlike for instance time-of-flight filters, allows both pulsed and cw operation. The ion source in the figure is the microwave discharge source described in section 2.2.2. The discharge products from the source held at +20 V pass through a grid and are accelerated towards a 2 mm skimmer held at -20 V.

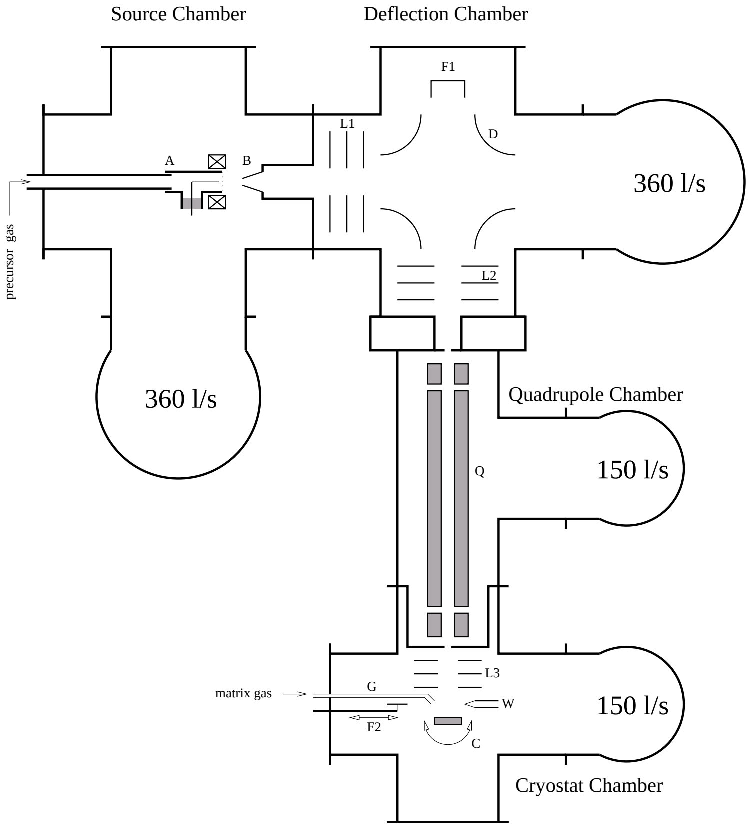

Figure 2.10: Schematic of the experimental apparatus for mass-selected matrix studies, with microwave discharge ion source (A), skimmer (B), first electrostatic lens (L1), deflection unit (D), first Faraday cup (F1), second lens (L2), 12mm triple stage quadrupole mass filter (Q), final lens (L3), rotatable cold-surface (C), matrix gas inlet (G), movable Faraday plate (F2) and the tungsten filament (W).

The pressure in the source chamber evacuated by a 360 l/s turbo-molecular pump is 10^{-4} - 10^{-2} mbar, whereas without running source 2x10^{-7} mbar are reached. The whole vacuum system of source, deflection and quadrupole chamber consists of standard ISO-K chambers and flanges with diameters of 160 mm and 100 mm, respectively. The achieved end pressure of 2x10^{-7} mbar is quite good for this kind of vacuum system and is far enough for our ion beam experiments, since the average free path between two collisions is approximately 1000 m at 10^{-7} mbar.

The ionic species exiting the skimmer into the deflection chamber are focused with the help of an einzel lens L1 and deflected 90° in a quadrupole electric field. After the skimmer, the source chamber and the deflection chamber are separated by a gate valve which allows to change or repair the ion source without venting the whole apparatus. A second lens, L2, then focuses the ions upon the entrance aperture of a quadrupole mass filter, with the undeflected neutrals being pumped by a second 360 l/s pump. The potentials applied to the different electrodes, as well as the trajectory of the ion beam, are discussed in the next subsection.

The commercial triple stage HIDEN HAL/3F quadrupole filter with 12 mm rods has a specified mass range up to 500 amu, a resolution $<$ 1 amu and is described in detail in section 2.4.3. The custom modified filter has 7 mm entrance and exit apertures, and is differentially pumped by a 150 l/s pump. Its exit aperture reaches into the cryostat chamber to be as close to the cold surface as possible. The mass selected ion beam is then focused onto the matrix by means of a lens L3 and deposited simultaneously with the matrix gas, neon in the present case. The substrate, a silver coated copper plate is held at $\approx$7 K by the LEYBOLD closed-cycle refrigerator. Taken from the old setup, the whole cryostat chamber is reused in the new experiment, only the flange holding the movable Faraday plate has been replaced.

To maintain overall neutrality of the matrix, and avoid building up space charges and stray fields, the matrix was sprayed by electrons from a hot tungsten filament held at approximately -100 V. We experimented with alternating the ion and electron deposition, but in the end continuous operation proved to be most efficient, with optimal results being obtained with the electron current being about five times the ion current.

In order to optimize the experiment, the ability to measure the ion current is essential. For this purpose, one Faraday cup (F1) permitting measurement of the total ion current is located in the deflection chamber. A second, removable detector (F2) close to the cold surface allows measuring the mass selected ion current. The weak currents are amplified by a FEMTO DLPCA 100 current amplifier and digitized in the mass filter control unit. Currents as low as 100 fA can be easily detected and we obtain mass spectra with S/N better than 10000:1. With the mass filter

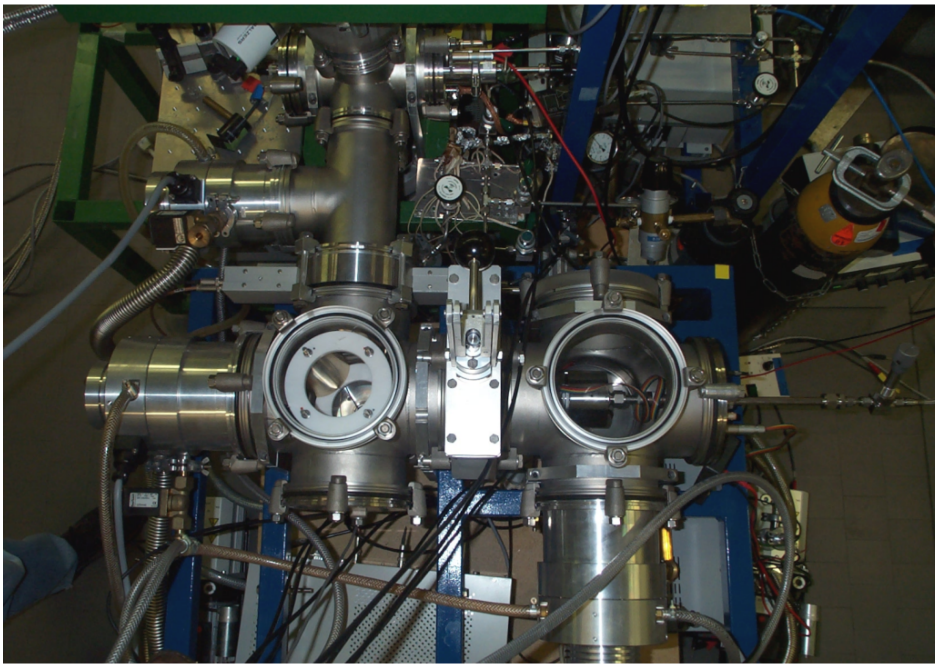

Figure 2.11: Photograph of the new experimental setup: To the right bottom, one can see the source chamber (including the EI source) connected via a gate valve to the deflection chamber (bottom, left). The subsequent T-piece contains the quadrupole mass filter and is attached to the cryostat chamber (top, left) with the FTIR spectrometer (hidden) following in the background.

set to the desired mass, all the experimental parameters can be adjusted for maximum current. With our microwave discharge source we could produce mass-selected currents of up to 1-2 nA and with the new EI source mass-selected currents of up to 20 nA (H_2^+) have been recorded.

After deposition, the matrix is rotated 120° and then the matrices are characterized spectroscopically using the IFS 120 HR Fourier transform spectrometer, equipped with beam splitters and detectors for the 500 - 30000 cm^{-1} spectral range. A photograph of the new experiment showing the mass-selection attached to the cryostat is presented in Fig. 2.11.

2.4.2 Ion Optics

Before designing mechanical drawings of ion-optical parts, it is advisable to perform *computer simulations* of the parts to get a feeling of how electrodes determine the electrostatic potential and how this potential influences the trajectories of “flying” ions. Furthermore, doing simulations allows the optimization of ion optics without changes in the “hardware” and one obtains information about the optimized voltages applied to the different electrodes, which is useful when one has to choose and order appropriate voltage supplies.

Theoretical background To calculate the electrostatic potential of a given arrangement of charged electrodes, one has to find solutions of the static MAXWELL equations which explicitly contain the electric field $\mathbf{E}$:

$$\begin{aligned} \nabla \cdot \mathbf{E}(\mathbf{x}) &= \frac{1}{\varepsilon_0}\rho(\mathbf{x}) && (2.3) \\ \nabla \times \mathbf{E}(\mathbf{x}) &= 0 && (2.4) \end{aligned}$$

Here the first equation, called the GAUSS law, states that the source of the electric field is the charge density $\rho(\mathbf{x})$, and from the second equation follows that the field can be expressed as a gradient of a scalar potential $\phi(\mathbf{x})$, $\mathbf{E} = -\nabla\phi(x)$, leading to the combination

$$\nabla \cdot (\nabla\phi) = \left(\frac{\partial^2}{\partial x^2} + \frac{\partial^2}{\partial y^2} + \frac{\partial^2}{\partial z^2}\right)\phi = -\frac{1}{\varepsilon_0}\rho \tag{2.5}$$

which is known as the POISSON equation. Since the free space between the electrodes is (almost) free of charges, one can set $\rho = 0$ reducing equation (2.5) to the LAPLACE equation

$$\left(\frac{\partial^2}{\partial x^2} + \frac{\partial^2}{\partial y^2} + \frac{\partial^2}{\partial z^2}\right)\phi = 0 \tag{2.6}$$

To solve this equation numerically, the continuous potential $\phi(x, y, z)$ is “sampled” at equally spaced discrete points with distance h, $\phi_{ijk} = \phi(x_0 + ih, y_0 + jh, z_0 + kh)$ leading to

$$\left(\frac{\phi_{i+1jk} + \phi_{i-1jk} - 2\phi_{ijk}}{h^2} + \frac{\phi_{ij+1k} + \phi_{ij-1k} - 2\phi_{ijk}}{h^2} + \ldots\right) = 0 \tag{2.7}$$

Rearranging this equation, one obtains an expressive equation for the “center point” ϕ_{ijk}

$$\phi_{ijk} = \frac{1}{6}\left(\phi_{i-1jk} + \phi_{i+1jk} + \phi_{ij-1k} + \phi_{ij+1k} + \phi_{ijk-1} + \phi_{ijk+1}\right) \tag{2.8}$$

i. e. the potential equals at each point the average of the potential of all neighboring points. This equation is iteratively applied to all points of the electrode-free space until subsequent changes become negligible which means that convergence has been achieved.

Using the potential obtained by this procedure, one can simulate the trajectory $\mathbf{x}(t)$ of charged particles by solving numerically the equation of motion applying the LORENTZ force

$$m\ddot{\mathbf{x}} = \mathbf{F} = q(\mathbf{E} + \dot{\mathbf{x}} \times \mathbf{B}) \tag{2.9}$$

It is interesting to note that the trajectories of particles with different masses have the same form providing they start from the same point, same direction and they have the same kinetic energy. The numerical calculation of the potential, as well as the simulation of trajectories, were performed using the commercial SIMION-3D program [119] and some results are presented in the next subsection.

Results The results of the ion optics simulation are presented in the same sequence as the ions fly through the apparatus. Hence the first calculation simulates the ion beam emitted from the source through the skimmer, then the entering into the deflection chamber through a gate valve and, finally, the focusing by the first einzel lens L1, as shown in Fig. 2.12.

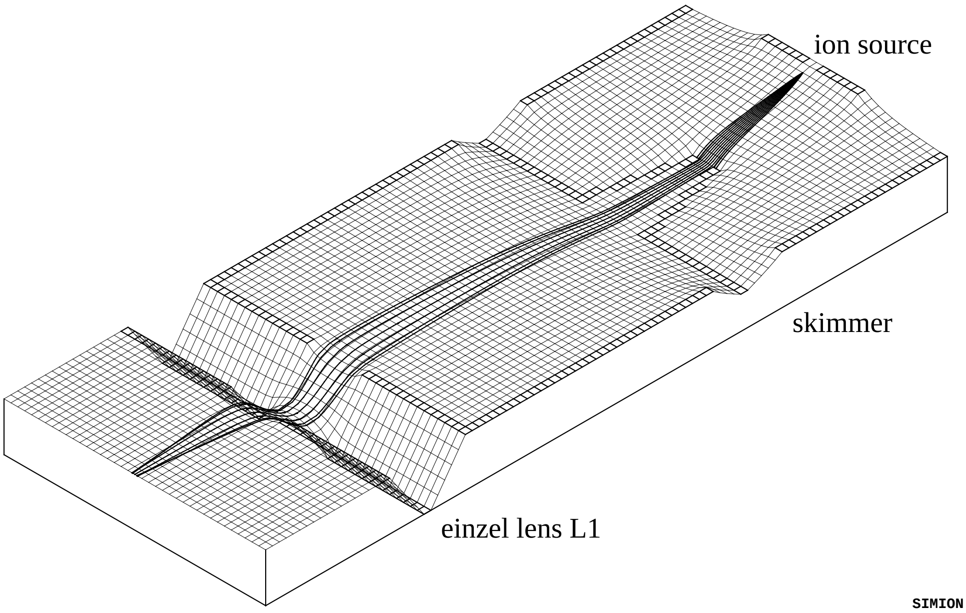

Figure 2.12: Simulation of the ion source (kept at +20 V, determines the kinetic energy) and the skimmer (-20V) in the source chamber (= mass potential = 0 V), as well as the transition through the gate valve into the second chamber with the first einzel lens L1 (center electrode at -60 V).

Here, the ion source (for example the microwave discharge or the laser vaporization) is kept at +20 V determining the kinetic energy of the ions which are emitted with negligible thermal energy. Then the ions are accelerated towards the skimmer held at -20 V for maximum ion current. A higher negative potential of the skimmer has the effect that more ions are “sucked” into the skimmer, but this has also the disadvantage of a stronger beam divergence after the skimmer. After approximately 10 cm of “free flight” through the open gate valve, the beam enters the first einzel lens L1 mounted in the deflection chamber. This lens is necessary to make a parallel beam out of the divergent one, and as one can clearly see, applying for example -60 V to its center electrode is enough for a short focus length of $\approx$ 7 cm. This focus length of electrostatic einzel lenses is proportional to kinetic energy / center voltage.

In contrast to the first simulation, which is a relatively simple two dimensional problem with cylinder symmetry, the following simulation requires a real *3D* calculation: The simulation of the ion beam in the second chamber, the so-called “deflection chamber”. A horizontal cut through the deflection unit in the plane of the ion beam is presented in Fig. 2.13, showing the corresponding electrostatic potential. The deflection unit consists of four 90° sectors, cut from a 100 mm brass tube (25 cm long), and appropriately arranged to generate an electric quadrupole field which deflects the ion beam by a right angle. Attached to the deflection unit are two einzel lenses at the entrance (L1) and at the exit (L2); the latter one focuses the beam into the quadrupole mass filter.

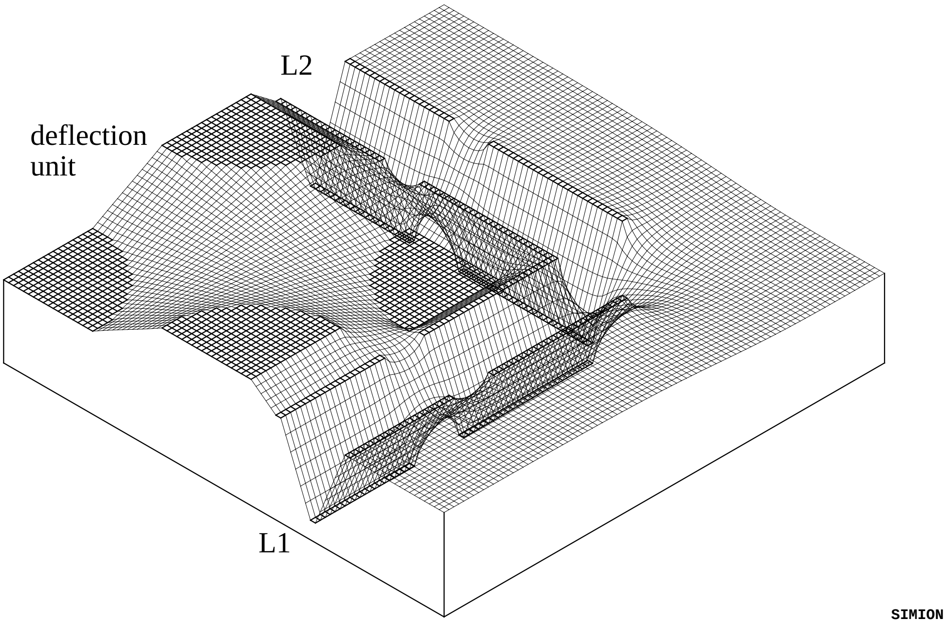

Figure 2.13: The electric potential of the quadrupole deflection unit including the einzel lenses L1 and L2, applying +/- 17 V to the quadrupole electrodes and -60 V to the center electrode of the lenses.

In Fig. 2.14, the three-dimensional geometry of the deflection unit is shown, including the trajectories of two different bunches of ions with the same energy and the same potentials on the electrodes. The left part shows a horizontal fan of ions with a kinetic energy of 20 eV, whereas the right part shows a vertical fan. As one can clearly see, both fans are well deflected (practically no losses) by a right angle with the horizontal one having a focus in the center of the deflection unit.

It is interesting to note that the deflection voltage applied to two adjacent electrodes (here 34 V) must be approximately 1.7 times the kinetic energy (in electron volts) of the ions to obtain a 90° deflection angle. This relation allows the easy determination of the actual kinetic energy of the ions. Furthermore, one can see that the lens L2 focuses the beam well into the small entrance aperture of the following QMS with a diameter of only 7 mm. The variable deflection voltage can be adjusted to sweep horizontally over the aperture and to optimize the ion current measured after mass-selection. When reversing the polarity of the deflection unit, the beam is bent in the opposite direction allowing the measurement of the total ion current at Faraday cup F1.

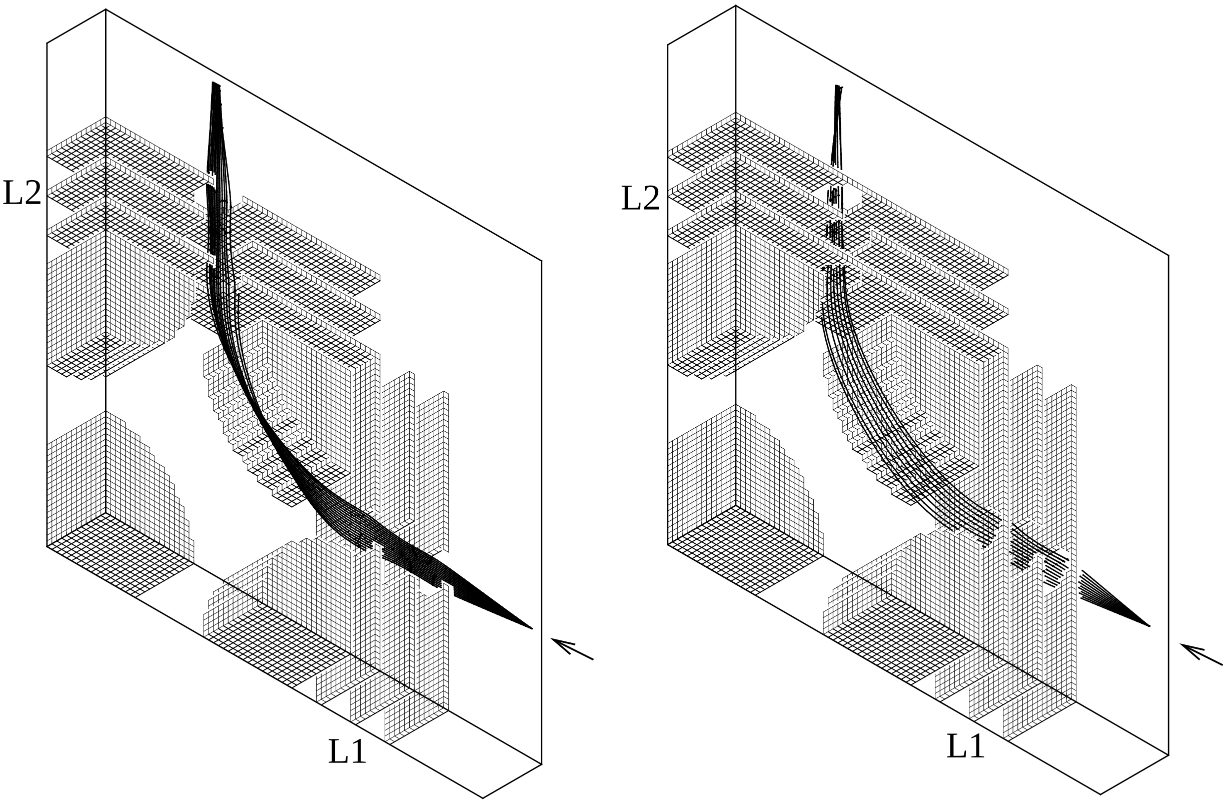

Figure 2.14: Simulation of the trajectories of a horizontal (left) and a vertical fan-like bunch of ions (right) flying through the deflection unit with a kinetic energy of 20 eV and starting from the right side at the bottom.

2.4.3 The Quadrupole Mass Filter

Principle of operation

Central to the principles of operation of an quadrupole mass spectrometer (QMS) is the geometry of the quadrupole field. An electric quadrupole field is expressed by its linear dependence on the coordinate position

$$\mathbf{E} = E_0 \begin{pmatrix} \alpha x \\ \beta y \\ \gamma z \end{pmatrix} \tag{2.10}$$

where α, β, γ are weighting constants and E_0 is a position independent factor which may be a function of time. This field is constrained by the GAUSS law (2.3) so that $\alpha + \beta + \gamma = 0$ which may be satisfied the simplest way by for example

$$\alpha = -\beta;\ \gamma = 0$$

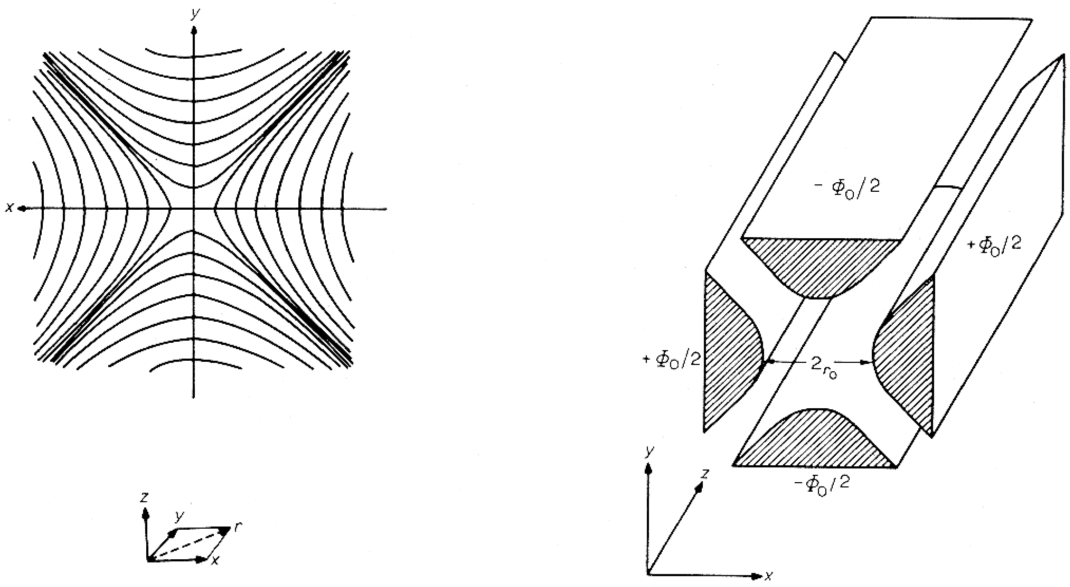

Figure 2.15: Equipotential lines of a quadrupole field (left) and the electrode structure (right) to generate it. These are the ideal quadrupole mass filter electrodes having hyperbolic cross-sections. From Ref. [78]

By integrating the resulting field, one obtains for the corresponding potential

$$\phi = -\frac{1}{2} E_0 \alpha (x^2 - y^2)$$

and the equipotential lines are shown in Fig. 2.15(left). They are sets of hyperbolae in the xy plane with a four-fold symmetry axis about the z axis. Such potentials are easily generated by a set of four hyperbolic cylinders with adjacent electrodes oppositely charged as shown in the right part of the same figure. The hyperbolic rods are replaced in practice by round rods approximating the quadrupole field, but these rods introduce field distortions affecting the resolution of the QMS which is discussed in detail in [78], chapter V. Assuming that the voltage between the electrodes is Φ_o and the distance between opposite rods is $2r_0$, then the potential becomes to

$$\phi = \frac{\Phi_0(x^2 - y^2)}{2r_0^2} \tag{2.11}$$

Using this potential ϕ, one obtains three decoupled equations for the ion motion

$$\begin{aligned} m\ddot{x} &= -\frac{e\Phi_0}{r_{0^2}}x && (2.12)\\ m\ddot{y} &= +\frac{e\Phi_0}{r_{0^2}}y && (2.13)\\ m\ddot{z} &= 0 && (2.14) \end{aligned}$$

After injecting ions in the QMS along the z axis, the motion in the xz and yz planes is given by (2.12) and (2.13), respectively. Assuming a constant potential applied to the electrodes (the DC case), the motion in the xz plane is simply a harmonic oscillation, whereas in the yz plane, the ions diverge from the z axis. On the other hand, if Φ_0 is a periodic function of time, the ions are alternately attracted/deflected from the z axis resulting in stable trajectories in both planes providing the period is short enough (the AC case, which is used as ion guide).

In combining the DC and the AC case, using $\Phi_0 = U - V\cos(\omega t)$, the quadrupole can be used as a mass filter applying appropriate voltages U and V with frequency $\omega$to the rods. The equations of motion of a mass filter can now be expressed as

$$\frac{\partial^2}{\partial\tau^2}u \pm (a - 2q\cos 2\tau)u = 0 \tag{2.15}$$

where $\tau = \omega t/2$, u represents either x or y and defining

$$a = \frac{4eU}{m\omega^2 r_0^2},\ q = \frac{2eV}{m\omega^2 r_0^2}$$

Equation (2.15) is the MATHIEU equation in its canonical form whose properties, and in particular the stability of its solutions, are well known. Depending on the value of a and q, the MATHIEU equation has stable solutions as shown in Fig. 2.16(left). Areas with stable motion in both x and y directions can be used as mass filter.

The nature of the ion motion in the yz plane is illustrated at the right side of Fig. 2.16 showing several points in the stability diagram with the initial conditions being $u(0) = 1$ and $\dot{u}(0) = 0$:

a. the point $q = 0.55,\ a = -0.1625$ close to the lower limit of the first region of stability (in y direction); the periodicity is π

b. the point $q = 0.55,\ a = 0$ within the first stability area. The trajectory is complex with periodicity $> 2\pi$ but stable.

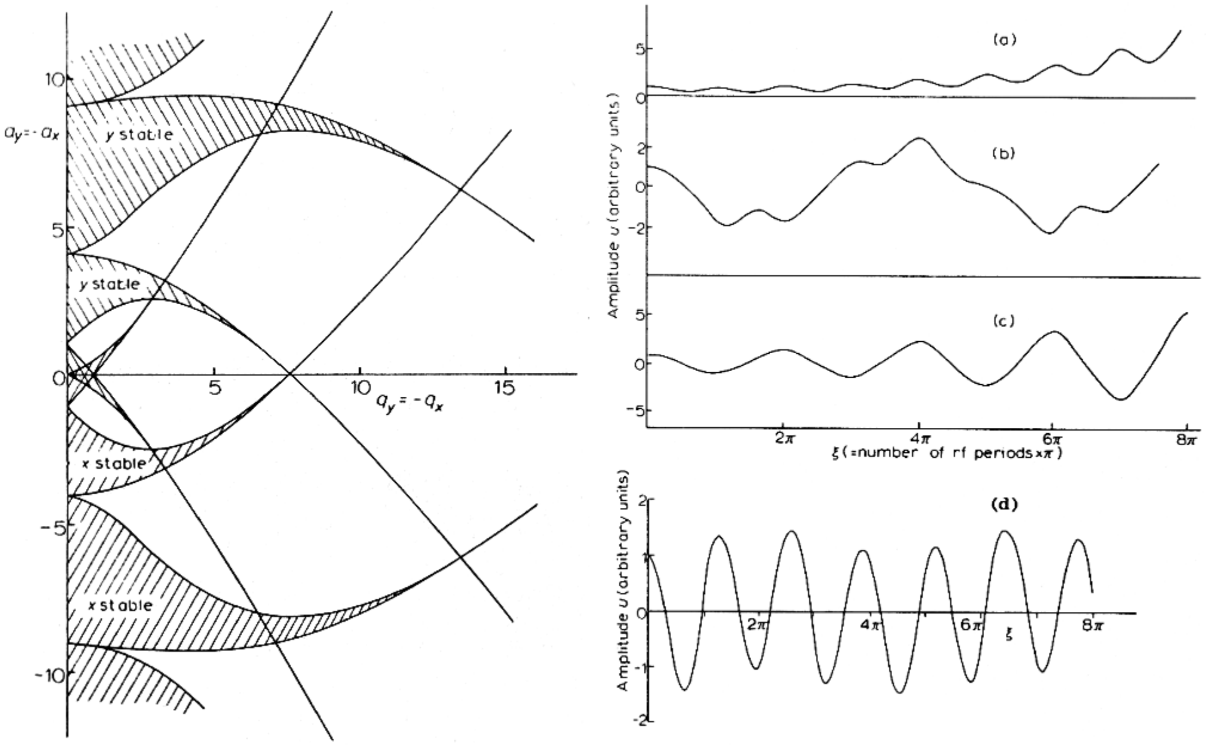

Figure 2.16: The Mathieu stability diagram of a quadrupole (left) showing regions of simultaneous stability in the x and y directions, as well as some ion trajectories for several points in the stability diagram. From Ref. [78]

c. the point $q = 0.55,\ a = 0.425$ near to the upper limit of the first stability area; periodicity= 2π

d. $q = 0.55,\ a = 2.5$ within the second region of stability.

A magnified part of the stability diagram, the first region of stability for both x and y directions is shown in Fig. 2.17. The peak of this region at $q = 0.706,\ a = 0.237$ is usually used to obtain mass resolution. For fixed $U,\ V,\ \omega$ and r_0, all ion masses (m/e) lie on the same line of constant a/q which is called the mass scan line or operating line. Now only those ion masses which intersect the peak of the stability region have stable trajectories and will pass through the filter. By increasing the U/V ratio, the operating line becomes steeper and approaches the tip of the stability region which leads to a narrowing of the range of masses passing through the filter. By this way, the resolution of the filter can be varied electronically by simply adjusting the U/V ratio leading to a trade-off between transmission and resolution. Keeping the rf frequency ω fixed in resonance with the "cavity", mass spectra are usually scanned by varying the magnitude of U and V but keeping the U/V ratio constant in order to maintain a constant mass resolution.

For common commercial QMSs, the available choice for the rod diameter d_{rod} and the AC voltage V is somehow limited. The rod diameter, which is connected to r_0 by $d_{rod} = 2.296 r_0$ to get the best approximation of the quadrupole field, has acceptable values in the range 5-20 mm

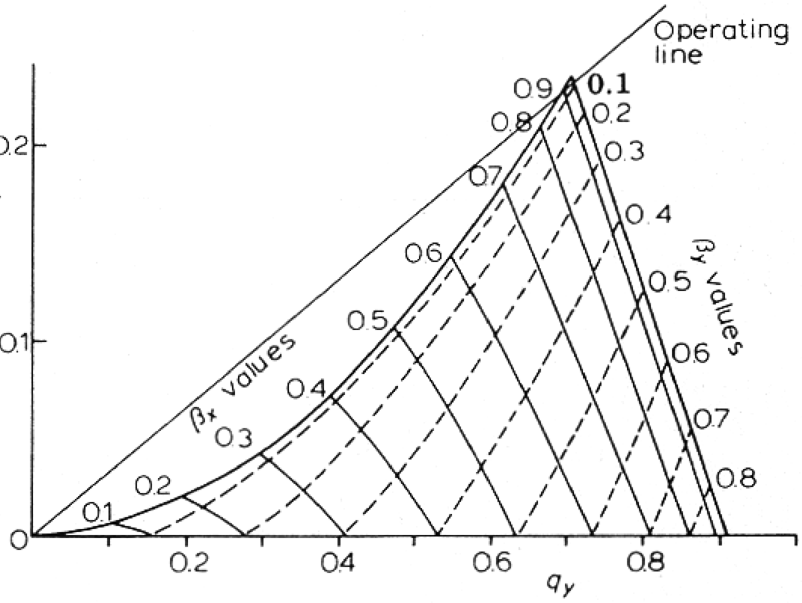

Figure 2.17: The lower stability region normally used in mass filter operation showing iso-β lines for the x and y directions and a typical operating line. From Ref. [78]

and V is of the order 3000 V. The rf frequency ω, which determines the maximum mass $\propto \omega^{-2}$ and the resolution $\frac{m}{\Delta m} \propto \omega^2$ in opposite directions, is usually set in the range 500 kHz - 10 MHz allowing mass ranges up to the order of 1000 amu.

The HIDEN HAL/3F Quadrupole Mass Spectrometer

The HAL/3F QMS from HIDEN Analytical was chosen because HIDEN was the only company which offered a custom modified QMS for a reasonable price and has a local branch office here in Germany. The HAL/3F consists of a HAL IV controller (with RS232 interface to a PC), a separate rf generator, an EPIC mass analyzer (with 12mm rods, triple stage filter, custom modified mounting flange and electrical feedthroughs) and the software HAL MASsoft.

The HAL/3F has the following specifications:

design	12 mm rods for enhanced transmission, triple stage for better line profile
mass range	1-500 amu
resolution	better than 0.5 amu throughout the mass range
transmission	up to 30% (not including losses due to apertures, etc) depending on resolution
scan speed	200 amu/s or 55 mass channels/s
ion energy	$\approx$ 10 eV (determined by the ion source)

Being the heart of HIDEN's commercial rest gas analyzers (RGA), the EPIC quadrupole mass filter is mounted on a special DN160 ISO-K flange (containing the electrical feedthroughs) without the ion source and detectors used for RGAs. It has 7 mm entrance and exit apertures and is differentially pumped, in our experiment, by a 150 l/s turbo pump to get rid of the discriminated ions.

The MASsoft software allows several different methods to obtain mass spectra:

- *Profile:* the mass range is scanned continuously with sub-amu resolution
- *Bar:* the mass range is scanned in 1 amu steps
- *MID:* Multiple Ion Detection, arbitrary masses are scanned sequentially
- *Shut down:* the QMS stays fixed at a certain mass; used for ion deposition and for optimizing the source and ion optics

After measuring a mass spectrum, the spectrum is exported as a xy-ASCII file and transfered to a UNIX workstation for further analysis.

2.4.4 Mass Spectra

In this subsection, some mass spectra are presented as an example to show the resolution of the QMS or to demonstrate the characteristics of different ion sources. Two mass spectra have been presented already on pages 29 and 30, respectively, to characterize the electron impact ion source.

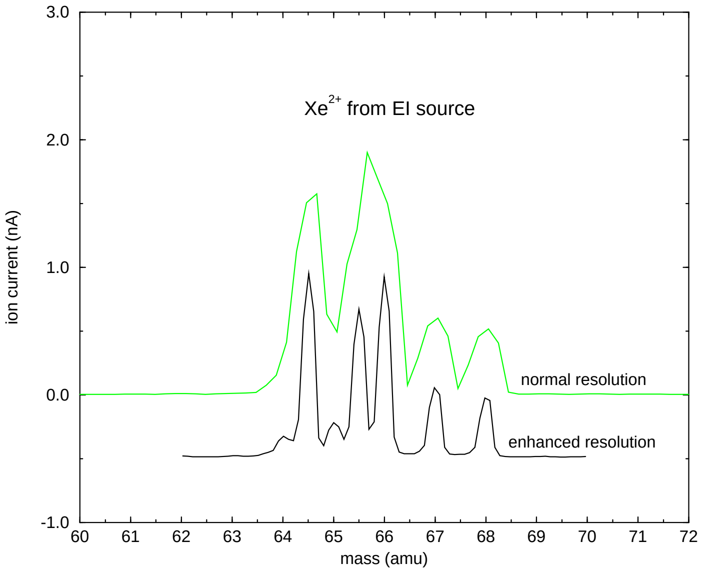

Figure 2.18: Xe^{2+} ions from the EI source using 80 eV electrons to ionize the xenon. This diagram clearly shows the sub-amu resolving power of the HAL/3F QMS separating well the different isotopes of xenon with the most abundant ones distributed at masses 128(2%), 129(26%), 130(4%), 131(21%), 132(27%), 134(10%) and 136amu (9%).

The example spectra shown in Fig. 2.18 using xenon with its rich isotopical structure as precursor substance illustrate the resolving power of the HIDEN HAL/3F. Here, 80 eV electrons have been used to double-ionize the xenon showing the characteristic isotopical pattern of the natural abundance of xenon. Apparently, peaks of neighboring masses, which are separated 0.5 amu, are well resolved.

In Fig. 2.19, the microwave discharge source is characterized comparing the pinhole nozzle (foreground) with the mesh (background), see section 2.2.2 . One can clearly see that using the mesh instead of the pinhole generally increases the ion yield by a factor of ≈ 3 and that, due to the higher pressure in the source, N_4^+ is more readily produced when using the pinhole. This figure, as well as Fig. 2.8, exemplifies the great signal/noise ratio of almost 5 decades achievable by this combination of QMS, Faraday detector and sensitive current amplifier.

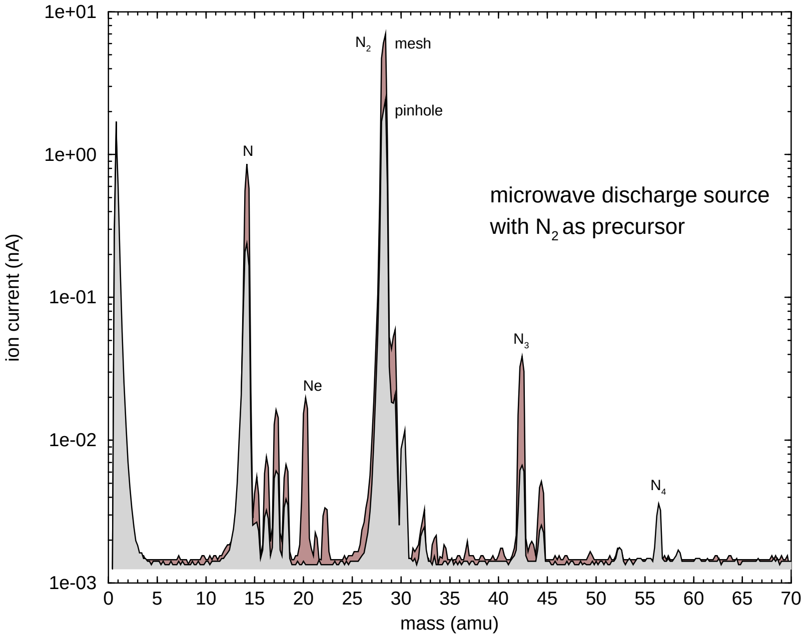

Figure 2.19: Mass spectra from the microwave discharge source using N_2 as precursor gas comparing the pinhole nozzle (foreground) with the replacing mesh (in the background).

A final mass spectrum, shown in Fig. 2.20, illustrates the attempts to combine our laser vaporization source with the mass-selection. Ablating a niobium target using 20 mJ pulses of 532 nm Nd:YAG laser light and neon with 5 bar background pressure, the monomer and niobium monoxide cations are produced but no higher clusters were detected. Unfortunately, the observed average currents of ≈ 10 pA are much to weak for spectroscopic investigations, although peak currents of up to 50 nA with 20 μs length could be observed. A vaporization laser with high repetition rate (≥ 1000 Hz instead of 10 Hz) would be necessary to efficiently combine this source with the mass filter

Additional mass spectra using CS_2 and C_6F_6 as precursor substances are presented in chapter 7 dealing with the corresponding cations.

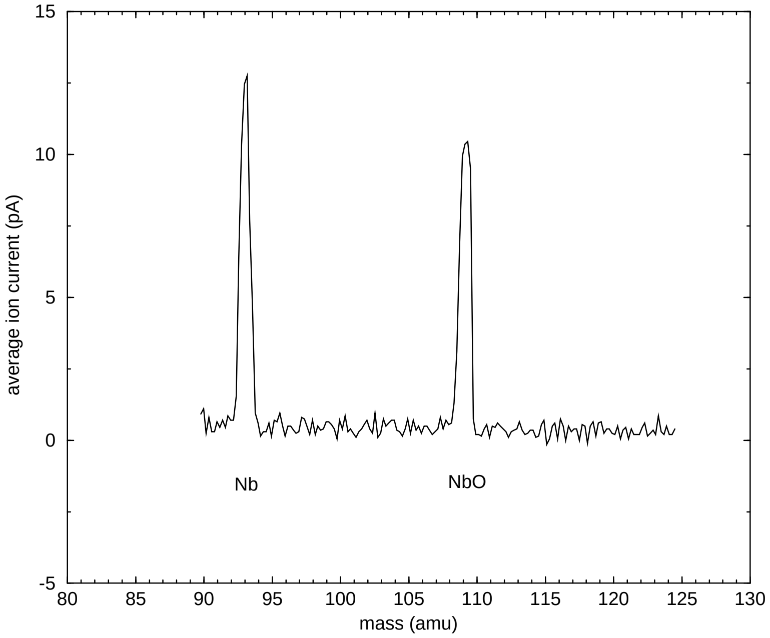

Figure 2.20: Mass spectrum of laser vaporized niobium. The NbO peak is due to oxides on the surface of the target.

2.4.5 Deposition of Mass-Selected Ions

Since there is a trade-off between low kinetic energy and high ion beam current, the mass-selection is usually performed at relatively high kinetic energy of 50-1000 eV. Although our quadrupole mass spectrometer works best for 10 eV energy, optimized ion currents are reached at 30-50 eV without significantly reducing the resolution. After mass-selection, it is difficult to slow down the ions below some 10 eV. An ion reaching the surface of for instance solid neon with an energy of > 10 eV can easily fragment, and the problem of *soft-landing* the ions and their fragmentation is discussed in detail in [24]. Due to the low van-der-Waals bond energy of 3.7 meV between neon atoms, it can also "melt" some 3000 matrix atoms, or cause the evaporation of about 500, which in turn can lead to enhanced diffusion. The incoming ion can penetrate deep into the solid, resulting in aggregation and reactions with other species already present in the matrix, thus defeating the major aim of matrix isolation. A final problem lies in the space charge resulting from accumulation of the charged species in the nonconducting rare gas matrix [25]. This may result in stray electric fields deflecting the molecular ion beam and further complicating the ion deposition.

Following mass selection, the ion beam is focused onto the matrix substrate by means of a further einzel lens L3. The ion beam is deposited on the substrate simultaneously with the matrix gas, neon in the present case. In order to maintain the overall neutrality of the matrix, and avoid building up space charges and stray fields, the matrix was sprayed by electrons from a hot tungsten filament held at negative potentials of up to $U_{Fila} = -200$ V. We experimented with alternating the ion and electron deposition, but in the end continuous operation proved to be most efficient, with optimal results being obtained with the electron current maintained at about five times the ion current.

The process of ion deposition is shown schematically in Fig. 2.21. The non-conducting matrix surface is irradiated by electrons from the filament and it is charged negative until the surface reaches the same potential as of the filament. Additional electrons are now deflected by the negative potential of this space charge zone — an *equilibrium* has been reached. Arriving ions, which have an initial kinetic energy of $E_i = 20$ eV, are accelerated towards the matrix and hit the surface with the final energy $E_f = E_i + e|U_{Fila}| = 220$ eV. In this way, the voltage of the neutralizing filament has important influence on the damage done to the matrix by the impact of the ion beam which will be discussed in detail in this subsection.

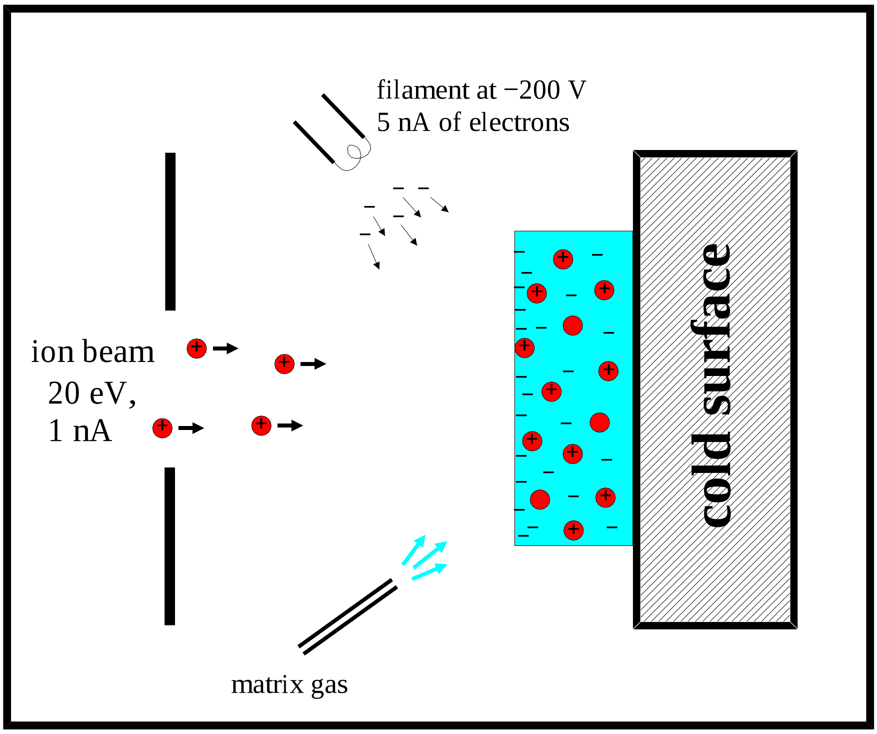

Figure 2.21: The process of ion deposition: The mass-selected ions with kinetic energy of 20 eV are codeposited with electrons and excess matrix gas. The electrical neutrality of the matrix is maintained in an equilibrium process and occasionally, some ions may be neutralized.

The electrons from the filament are trapped at lattice defects or at impurities and may occasionally neutralize some mass-selected cations. A quantitative analysis, to be presented later, shows that at least $\approx 20\%$ of the mass-selected ions survive the deposition process. When warming up the matrix, the trapped electrons are released again and recombine with positively charged partner emitting *thermally stimulated luminescence* (TSL). The released electrons can even escape from the matrix surface, the resulting *thermally stimulated exo-electron emission* (TSEE) can be measured easily with a Faraday plate close to the matrix surface. All these effects and the question of the thermal stability of charged centers in rare-gas matrices were studied extensively in our laboratory in collaboration with the Institute for Low Temperature Physics in Kharkov, Ukraine [120, 121].

Matrix Damage and Multiple Sites in the $C_6F_6^+$ $B^2A_{2u} \leftrightarrow X^2E_{1g}$ Spectroscopy

Laser excitation spectra of two different samples, each resulting from 3 h deposition of a beam current of ≈1 nA at mass 186 amu, are shown in Fig. 2.22. The difference between the two is in the energy of the ions impinging upon the matrix, which is estimated to be 220 eV for the top spectrum but considerably lower (20 eV) for the bottom one. While the bottom spectrum resembles the spectrum reported in a previous study [122] where the ions were generated by in situ vacuum UV ionization of neutral hexafluorobenzene, in the top spectrum where the ions were deposited with higher kinetic energy, each of the strong vibronic bands of hexafluorobenzene seems to be replaced by a group of several bands. Clearly, while in the sample where the beam was deposited with lower energy, as well as in the photo-ionized sample there is one dominant site, denoted by A, in the sample deposited with higher energy there are several *"sites"*, that is the cations occur in the neon matrix in several different local environments. The most intense subsidiary sites are denoted by the letters B and C, and can be seen to occur, albeit weakly, also in the bottom spectrum.

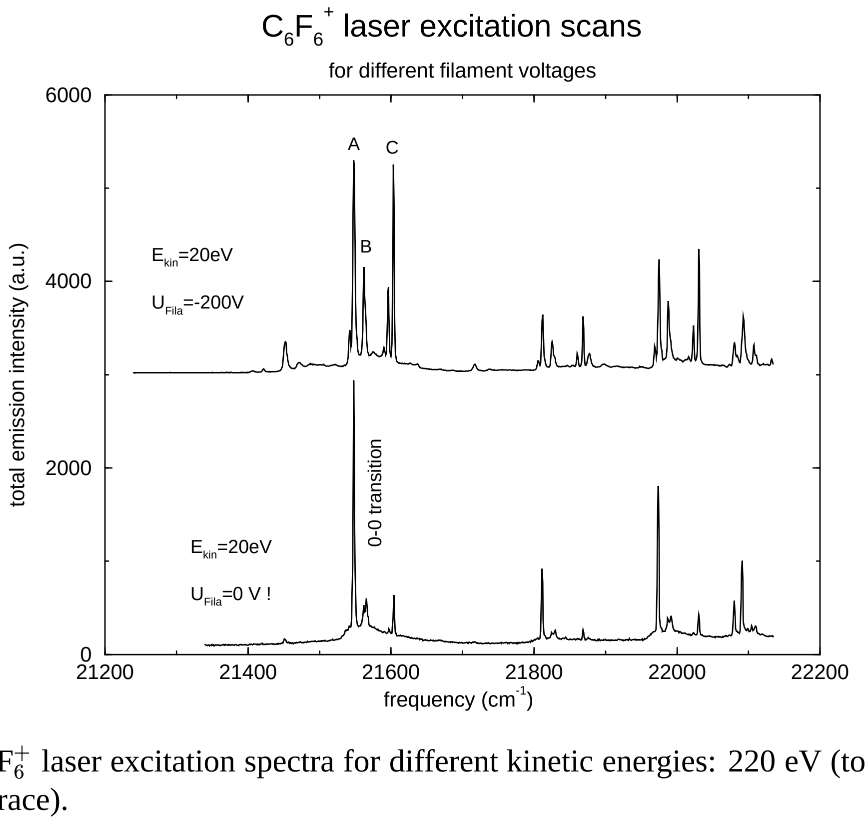

Figure 2.22: $C_6F_6^+$ laser excitation spectra for different kinetic energies: 220 eV (top trace) and 20 eV (bottom trace).

The fact that the origin of the additional bands is inhomogeneous, is confirmed by examining the emission spectra: exciting the B and C bands, which are blue shifted by 16 and 33 cm^{-1}, respectively with respect to the A bands, results in fluorescence whose origin is shifted by the same amount. The presence of several similar "spectra" shifted by similar amounts both in emission and excitation spectrum is a characteristic symptom of several distinct sites, that is in the present case the A, B and C bands correspond to the $C_6F_6^+$ cations "perturbed" by a slightly different local environment. The almost complete absence of the multiple sites from the spectra produced by *in situ* ionization, and their presence, and dependence of ion energy in the case of ions deposited from the gas phase suggests that they are the result of matrix damage due to the ion bombardment.

Some time ago we have noted that also in the case of matrix isolated linear carbon chain ions of the type X-C_n-Y^+ (where X and Y can be for instance H or CN), there exists a considerable difference between the spectra of ions produced in situ, and of the same ions deposited from a mass selected ion beam. While in situ study in our laboratory yielded very sharp bands, the ion beam deposited samples by Maier et al. gave usually bands with more that 100 cm^{-1} widths [104]. We have previously suggested [123] that this difference is probably due to matrix damage, and the present results, observing an analogous effect for quite different type of ions clearly provides support for this point of view.

Quantitative Analysis of Mass-Selected Ion Concentration

An visible absorption spectrum of a sample resulting from a codeposition of $\approx$3 nA current at mass 132 amu with pure neon for 3 h shows clearly the known visible absorption of the 1,3,5-$C_6H_3F_3^+$ radical cation. The strongest 0-0 origin band located at 21769.6 cm^{-1} exhibited an integrated absorbance of 0.094 cm^{-1}, and it was followed to higher energies by weaker vibrational structure. While numerous molecular ions were previously studied, relatively little is known about the achievable ion concentration. In the case of mass selected beam deposition, the extent to which the gas phase ions actually reach the sample, and survive the recombination, fragmentation and other reaction which can occur in the matrix or on its surface is therefore of considerable interest.

In the present experiments, there are in fact two independent ways in which one can estimate the ion concentration, or at least establish its limits. In the first place, by knowing the ion current reaching the matrix and the deposition time, one can easily compute the number of moles of the sample, and compare it with the number of moles of the simultaneously deposited matrix gas. For the column density, one obtains thus

$$c \cdot l = \frac{n}{A} = \frac{I\Delta t}{eN_A A} = 10^{-10}\,\frac{\mathrm{mol}}{\mathrm{cm}^2} \tag{2.16}$$

This easy computation in the experiment with the 1,3,5-$C_6H_3F_3^+$ gives a molar concentration of about 0.9-1x10^{-9}, that is one part per billion (ppb), provided no ion-electron recombination, or other reactions destroying the ions take place. Very similar numbers were in this way also obtained for the other molecular ions studied in this work.

There is, however, a second, independent way, in which the ion concentration can be estimated. The fully allowed B-X transition in the 1,3,5-$C_6H_3F_3^+$ cation is known to have in the matrix a lifetime of about τ =50 ns. This value exhibits little dependence on temperature, does not change appreciably when the molecule is deuterated, and is only slightly shorter than the gas phase lifetime. It is therefore very likely that non-radiative processes are insignificant, and the lifetime is basically radiative. Under this assumption, one can use the integrated absorbance from the obtained spectra to compute the ion column density, and obtain again from the known thickness of the matrix the ion concentration:

$$c \cdot l = \frac{8\pi c_0 \nu \tau}{N_A} \int A(\nu)\, d\nu \simeq 2.7 \cdot 10^{-11}\, \frac{\mathrm{mol}}{\mathrm{cm}^2} \tag{2.17}$$

with $\nu = 22000$ cm^{-1} and the integrated absorbance $\int A(\nu)d\nu \simeq 1$ cm^{-1}. While again the uncertainties in a number of the values entering the computation are relatively high, one obtains cation concentrations of the order of 0.1-0.3 ppb. Comparison of the numbers obtained in the two independent ways suggests, that approximately 20 % of the ions survive the deposition process. Consistent with this assessment, that recombination should not be dominant, is the observation that while we could observe weakly the absorption of the CS_2^+ cation, the absorptions which could be attributed to either neutral CS_2 or to the CS fragment were apparently too weak for detection, see section 7.3.1.

Part II

Tungsten Oxides in Solid Neon

Chapter 3

Vibronic Structure of Tungsten Oxides

> *Wenn man alle Gesetze studieren sollte,*
> *so hätte man gar keine Zeit,*
> *sie zu übertreten.*
>
> JOHANN WOLFGANG VON GOETHE

Tungsten oxides isolated in solid neonmatrices were generated using the pulsed laser vaporization technique, and their absorption as well as laser induced fluorescence spectra (LIF) were examined. A clearly resolved tungsten isotopic structure permits unambiguous spectral assignments. With the help of near infrared emission, several low lying electronic states of WO are observed and characterized. The symmetric stretching frequency of the triatomic WO_2 is identified, and the structure of the molecule is discussed.

3.1 Introduction

Transition metals and their compounds represent a challenge both to experiment and theory[124]. The presence of the partially filled d-electron shell usually leads to a complex electronic structure with a large number of low energy states, and a very rich spectroscopy. The interactions between them often perturb and complicate the spectra and make their interpretation difficult. For a meaningful theoretical treatment a large number of electronic configurations has to be considered. While a number of oxides and other simple compounds of the first and second row transition metals has been studied[125, 126, 127, 128, 129, 130], much less known are the heavy third row species. As a consequence of the lanthanide contraction, they frequently exhibit similarities to the second row species, but as a result of relativistic effects they also differ in many properties appreciably from their lighter relatives[131].

Tungsten and many of its compounds are high melting, refractory materials, whose vaporization requires temperatures ranging up to 3000 K, and this makes their gas phase studies experimentally difficult. An early gas phase visible emission study in the fifties revealed several electronic transitions of diatomic WO, and yielded for the lowest state, presumably the ground state, a vibrational frequency ($\Delta G_{1/2}$) of about 1055 cm^{-1} [132]. A decade later Weltner and McLeod (WM) examined the absorption spectra of tungsten oxides in solid rare gases [133]. They obtained the matrix isolated species by vaporizing from an inductively heated cell either the tungsten oxides directly, or by vaporizing the metal in the presence of gaseous oxygen. Two infrared absorption bands they observed, a strong one at 928 and a "medium" strength one at 992 cm^{-1} , were assigned to tungsten dioxide, based mainly on the observed frequency shift in an ^{18}O isotopic experiment. They also observed long series of absorption bands near 7890 Å, and identified them as progressions in the bending frequency of the triatomic WO_2 .

The infrared absorption of the diatomic WO was, on the other hand, not clearly identified, but numerous strong absorptions clearly due to WO were observed in the visible. Weltner and Mc Leod assigned the observed bands to seven distinct electronic transitions of WO, some of them clearly due to the systems previously observed in the gas phase. For the fundamental vibration of the WO ground state, which they believed to be of $^3\Sigma^-$ symmetry, they recommend as the best available value the $\Delta G_{1/2}$ frequency of 1055 cm^{-1} derived from the previous gas phase emission studies. The infrared spectra of several tungsten oxides in matrices were later reexamined by Green and Ervin [134].

Some ten years after WM, Samoilova *et al.* (SEG) produced WO in the gas phase by a flash-photolysis of $W(CO)_6$ in the presence of oxygen, and observed numerous further visible bands which they attribute to ten separate systems [135]. With the help of a sample enriched to 97% with the ^{186}W isotope they were able to analyze rotationally 14 of the observed bands to obtain the moments of inertia and bond lengths of WO in several of the electronic states.

Even more recently Nelin and Bauschlicher have investigated the lowest electronic states of WO theoretically by ab initio techniques, and compared their results with the isovalent MoO and CrO species [136]. They concluded that like its lighter relatives, WO has a $^5\Pi$ ground state, with a number of predicted very low lying electronic states.

A number of years ago we have demonstrated that high temperature molecular species for spectroscopic studies can be very conveniently generated by laser vaporizing a suitable solid precursor in the presence of an inert carrier gas, and also shown that the method is readily applicable not only to gas phase work [70], but also to matrix isolation studies [137]. In the present manuscript we employ this technique to revisit the spectroscopy of tungsten oxides. We show that with the help of modern high resolution FT-IR instruments not only the oxygen, but also the tungsten, isotopic structure can be clearly resolved, and this is extremely helpful in assigning and analyzing the matrix spectra. We also find that when excited by lasers, WO fluoresces in the neon matrix efficiently. Using laser induced fluorescence (LIF), we obtain extensive new information about the electronic structure of WO, and extend its spectroscopy into the near infrared region, beyond the regions studied in previous work.

3.2 Experimental

In the experiments described here, the matrix samples were prepared by vaporization of the tungsten solid using about 30 mJ of pulsed, frequency–doubled Nd-YAG laser light. A tungsten foil (99.96%, chemPUR) was electro–eroded into a 13 mm dia. x 0.5 mm thick disk. The laser pulses were synchronized with the opening of a pulsed valve controlling the flow of a neon carrier gas (99.998%, Messer-Griesheim) mixed with 0.2% oxygen (or $^{18}O_2$), and focussed upon the rotating disk, located tangentially to a 3 mm diameter flow channel. The laser–induced plasma was swept by the inert carrier gas flowing through the channel, and expanded into the vacuum enclosure of the cryostat.

About 2.5 cm downstream from the orifice of the expansion channel, both the neon carrier gas and the products (oxides) of laser vaporization are frozen onto a silver coated copper mirror cooled to about 6 K by a closed-cycle refrigerator (Leybold RGD 580). Typically, the disk is ablated for 1–2 hours at a repetition rate of 10 Hz and a neon backing pressure of 5 bar. The matrix is then studied spectroscopically using a Bruker IFS 120–HR Fourier transform spectrometer. Absorption spectra are measured from 600–30000cm^{-1} with equal or better than 0.5cm^{-1} resolution. The matrix fluorescence is excited by an argon–ion laser pumped, tunable cw dye laser or a Ti:sapphire laser. The sample emission is focussed upon the entrance aperture of the FT spectrometer, and detected, depending on the spectral range, either with the help of a photomultiplier, or using a liquid-nitrogen cooled germanium, indium antimonide or mercury cadmium telluride detector.

3.3 Tungsten monoxide, WO

3.3.1 Infrared absorption

As noted above the infrared absorption of the diatomic WO could not be clearly identified in the previous matrix investigation of tungsten oxides by Weltner and McLeod. In our present investigation the WO absorption is clearly observed, and its assignment confirmed not only by the ^{18}O isotopic substitution, but also by resolving clearly the tungsten isotopic structure, as shown in Fig. 3.1. The measured neon matrix frequencies of 1056.98 and 1001.77 cm^{-1} for

$^{186}W^{16}O$ and $^{186}W^{18}O$ respectively are in excellent agreement with the values deduced from the electronic absorption data of Samoilova *et al.* of 1056.7 and 1002.1 cm^{-1} , respectively.

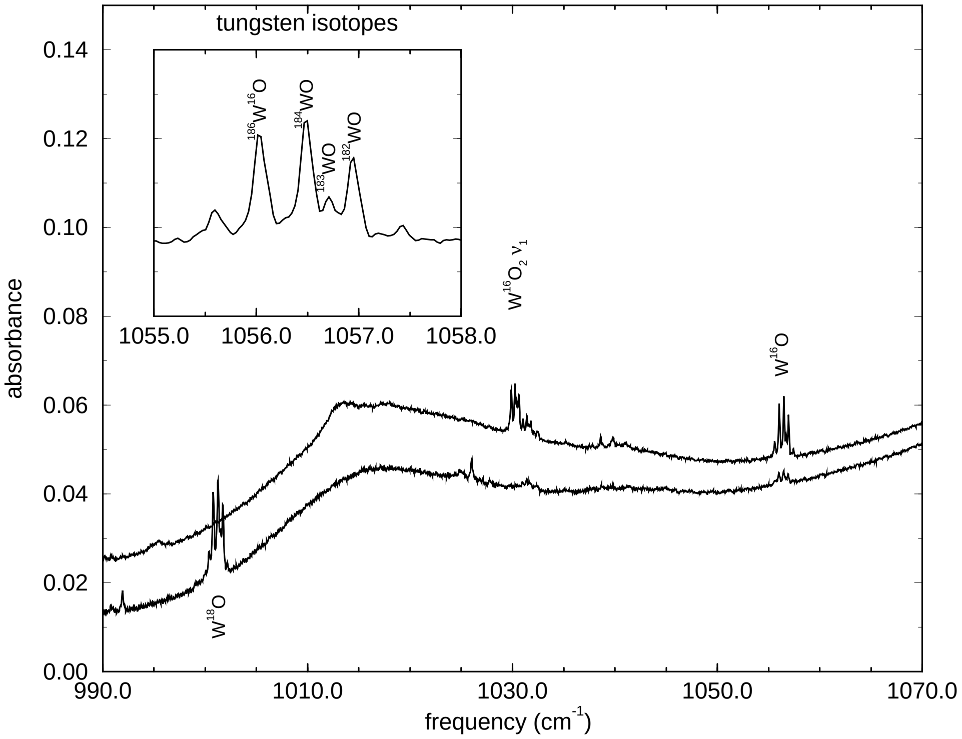

Figure 3.1: The IR absorption of tungsten oxides. The main traces show the absorption of tungsten oxides using $^{16}O_2$ (upper one) and $^{18}O_2$ (lower). One can easily see the bands due to WO (at 1056 and 1002 cm^{-1}) and the symmetric vibration of $W^{16}O_2$ at 1030 cm^{-1} . The insert shows the vibration of $W^{16}O$ with isotopical resolution.

Adjustment of the force constant results in a fit of the observed infrared absorptions of eight isotopic species of WO with a mean square deviation of less than 0.08 cm^{-1} , and yields a force constant of 9.679 mdyne/Å. This value is nearly twice that of diatomic CrO, but according to relatively fragmentary previous studies it is apparently considerably closer to the force constant of MoO [138], a finding consistent with the above mentioned similarity in properties between the second and third row transition metals, which is closer than that between first and second row metals.

3.3.2 Absorptions in the Visible Range

We have also reexamined the spectra in the visible region, and where our data overlap with those of WM, as well as with the gas phase data of SEG, our observations shown in Fig. 3.2 are in essential agreement. WM reported in this range seven electronic states which they denote A-G

[133], and we will adhere in our discussion to their notation, even though, as will be discussed below, we detect a number of states at lower energies. Modern FT instruments provide a more reliable frequency calibration than older grating instruments, and some of the bands reported by WM deviate by up to 5 cm^{-1} from our measurements. The higher sensitivity and improved signal to noise ratio also enabled us to extend the observations and observe numerous weaker bands undetected by the previous investigators. The X-A system can for both oxygen isotopes be followed, using the vibrational assignment of WM from $v' = 3 - 8$, and for the highest vibrational levels the tungsten isotopic structure is clearly resolved. We also detect an additional weak progression in the near UV, with an origin at 26972.7 and a vibrational frequency of 901 cm^{-1} . This H' state is, however, clearly not identical with the H state reported by SEG.

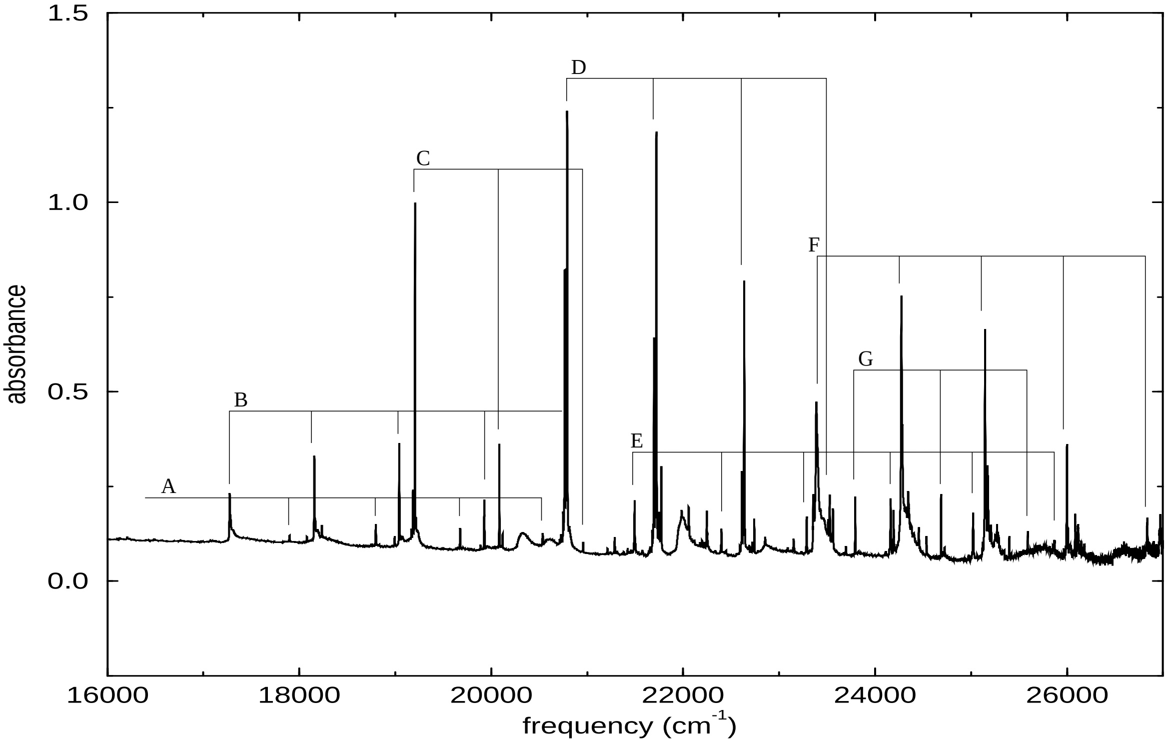

Figure 3.2: Visible absorption of W^{16}O in solid neon. The electronic systems are designated according to Weltner.

As already noted by Weltner, while most of the observed bands of the W^{18}O molecule can be reasonably well fitted to obtain spectroscopic constants, the spectra of the normal isotopomer are more erratic, apparently due to perturbations resulting from interactions between the A, B, and C states, as well as between the E and F states. In addition to the relatively strong absorption bands reported by WM, numerous weak sharp bands throughout the visible region, and in particular above 21000 cm^{-1} , are also detected. While these can be assigned without ambiguity to the WO molecule, since, as will be discussed below, they also appear in the laser excitation spectrum of the WO fluorescence, they apparently do not belong to any of the known states, and must be caused by the presence of other electronic states in this spectral region.

3.3.3 Near Infrared Transitions of WO

Since numerous very low lying electronic states are expected for tungsten oxides, we have extended our studies into the near infrared range below 12000 cm^{-1} using Ge and InSb infrared detectors. A most prominent group of five vibrational progressions clearly due to diatomic WO appears close to 7500 cm^{-1} , see upper trace of Fig. 3.4. Their T_{00} values are 7403.8, 7443.0, 7527.6, 7708.1 and 8007.6 cm^{-1} , and they exhibit very similar vibrational frequencies ω_e of about 950 cm^{-1} , with almost exactly the theoretically expected isotopic shift of $\rho = \nu(^{16}O)/\nu(^{18}O) = 1.055$. These near NIR absorptions are almost two orders of magnitude weaker than those in the visible spectrum.

Two additional pairs of transitions appear at higher energies. For the first pair, with T_{00} at 10880.0 (weak) and 10919.3 cm^{-1} (somewhat stronger) very weak $v' = 1$ levels could also be detected, with the vibrational frequencies matching again almost perfectly the theoretically expected isotopic shift. For the other pair with T_{00} at 11966 and 12030 cm^{-1} , only the $v' = 0$ origin was detectable. These two pairs of closely spaced bands may be due to WO in two different matrix sites. At still higher energies the spectrum is obscured by strong WO$_2$ absorptions, but one can still detect a sharp band at 14143.4 cm^{-1} , which does not fit into the WO$_2$ pattern. The assignment of all these bands to diatomic tungsten oxide was confirmed by their appearance in the laser excitation spectrum to be discussed in the following sections.

3.3.4 Electronic Fluorescence of WO in the Visible Range

Since fluorescence spectra can often provide valuable information complementary to absorption studies, we have excited the WO-containing matrices at a variety of frequencies ranging from about 12000 to 25000 cm^{-1} . Whenever the laser was tuned to one of the absorption bands assigned to WO a strong fluorescence was indeed observed, and we have recorded laser induced fluorescence (LIF) spectra at a number of excitation wavelengths. The structure of the visible fluorescence depends sensitively upon which band is excited, with some levels emitting efficiently, and others being absent. The observed pattern is indicative of a complex, isotopically dependent relaxation pathway, involving the vibrational manifolds of the numerous electronic states present in this region. While one can observe strongly resonant fluorescence from some levels, others are conspicuously absent.

For instance, when one excites the $v' = 0$ F-state level of the W^{18}O sample at 23387.61 cm^{-1} , there is no unrelaxed resonant emission. One observes a weak emission from $v' = 0$ E, $v' = 0$ D, and a long progression originating in $v' = 6$ A. There is no emission from $v' = 5$ or 4 of the A state, but weak progressions from $v' = 3$ and 2 A are observable. In addition, numerous bands are detectable, which have no obvious assignment. Two relatively weak progressions starting at 20265.41 and 19377.74 cm^{-1} exhibit a lower state vibrational frequency $\Delta G_{1/2} = 1004$ cm^{-1} distinctly different from the ground state X ($\Delta G_{1/2} = 1001.7$ cm^{-1}), and must be due either to a perturbed “site”, or terminate on levels of a very low lying electronic state of

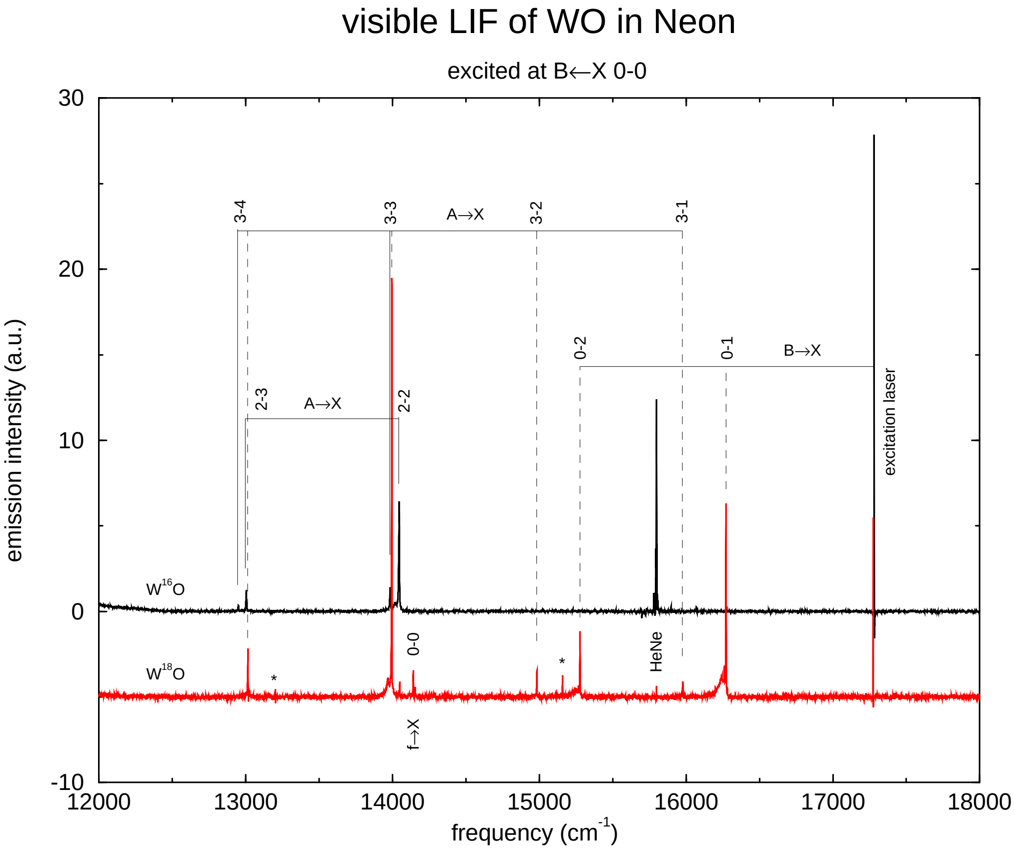

Figure 3.3: Visible LIF of tungsten oxide excited at the B $v = 0$ level at 17281.1 ($W^{16}O$) and 17273.9 cm^{-1} ($W^{18}O$), respectively. Both isotopomers show strong progressions originating from the $v' = 2, 3$ levels of the A state, with v'' in the range of 1 to 5. For $W^{18}O$, also the B → X transition, as well as unrelaxed emission from the B state into the ground state ($v'' = 0 - 2$) is observed. Peaks denoted with an asterisk could not be assigned yet.

WO, less than 3122 cm^{-1} above the X state. It appears that for excitation at higher energies, the spectra are rather complex and difficult to interpret in detail. The relaxation obviously involves additional electronic states not directly observed in absorption.

When absorptions at lower energy are excited, the emission spectra become simpler and easier to assign. Thus after excitation of the $v' = 0$ level of the B state of $W^{18}O$ at 17273.9 cm^{-1} (shown in Fig. 3.3), both unrelaxed emission of the directly excited level into the $v'' = 0$, 1, and 2 levels of the ground X electronic state, as well as emission from lower levels populated by nonradiative processes is observed. A weak progression from a level at 16980.4 cm^{-1} into the $v'' = 1 - 4$ is again the above mentioned $v' = 3$ A fluorescence. Careful examination of our absorption spectrum reveals, in fact, that the $v' = 3$ A absorption unobserved by WM appears very weakly in absorption also, at 16980.44 cm^{-1} . For both oxygen isotopes we could identify weak emission from both the $v' = 3$ and $v' = 2$ levels of the A-State. Surprisingly, however, contrary to the usual situation where the lowest vibrational levels are most prominent in fluorescence, no emission which could be attributed to either $v' = 0$ or $v' = 1$ was detected.

WM observed for the A state only levels with $v' \geq 4$, and they base their vibrational assignment on isotopic shifts. They note, however, that while the $W^{18}O$ spectrum can be reasonably well fitted, the normal $W^{16}O$ is clearly strongly perturbed due to the above discussed interactions with the B and C-states. In view of the unusual relaxation behavior, we have retried to fit the A-X transition data using the new information obtained in this work, in particular the $v' = 2$ and $v' = 3$ emission progressions. When all the data obtained for both oxygen isotopes, which included A state levels $v' = 2 - 8$ and ground state progressions up to $v'' = 8$ were used to derive Morse potentials for both states, a very poor fit was obtained. The root mean square error was ≈ 20 cm^{-1} , with some observed bands deviating more than 60 cm^{-1} from the calculated position. The mean deviation could be somewhat reduced (RMS error ≈ 16 cm^{-1}) by decrementing the A state vibrational assignment of WM, but the quality of the fit remained very poor. If the $v' = 4, 5$ and 6 A of the $W^{16}O$ isotope were given zero weight in the fitting, the remaining data were fitted with RMS error < 1 cm^{-1} . All the transitions involving the excluded $v' = 4, 5,$ and 6 $W^{16}O$ A-state levels were computed 15, 44, and 73 cm^{-1} respectively higher than observed. We conclude that the WM vibrational assignment is correct, and the $v' = 4 - 6$ levels of the normal isotopomer are strongly perturbed, as they proposed.

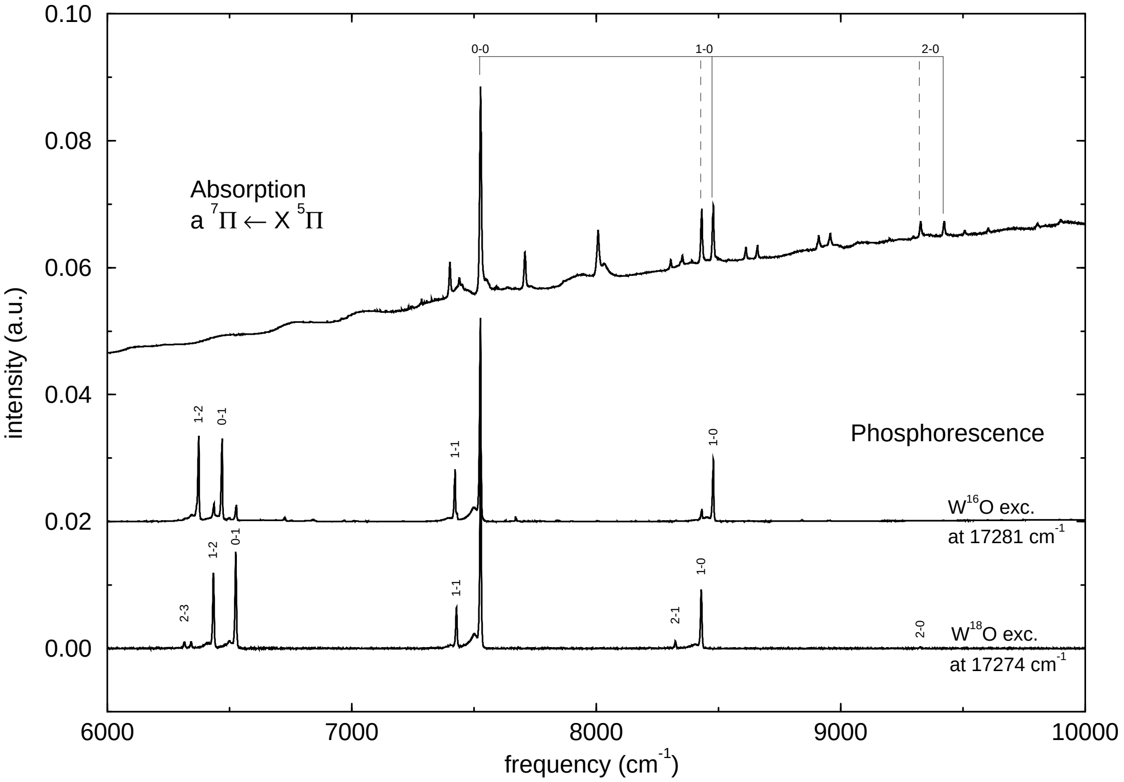

Figure 3.4: NIR absorption and phosphorescence of tungsten oxide. The upper trace shows progressions of several NIR states, with the strongest absorption, denoted a($^7\Pi$) $\leftarrow$ X$^5\Pi$, occurring at $T_{00} = 7527.8$ cm^{-1} . The lower two traces display the phosphorescence originating from the "a" state of both tungsten oxides, obtained after excitation of the B $v = 0$ state.

For all the excitation wavelengths one observes not only the visible fluorescence, but also a strong emission in the near infrared range. Unlike the visible fluorescence, the near infrared emission is relatively simple, and essentially independent of the specific level excited. Representative spectra recorded with excitation of the B-X 0-0 transition (B0 band) at 17281 and 17274 cm^{-1} for $W^{16}O$ and $W^{18}O$, respectively, are shown in Fig. 3.4. From the five transitions detected in the absorption spectrum, only the strongest one with an origin at 7527.6 cm^{-1} appears in emission. Interestingly, the infrared spectrum of the heavier ^{18}O isotopomer is at least an order of magnitude more intense, reflecting the isotopically dependent relaxation pathway, so that in fact the $W^{18}O$ emission appears with appreciable intensity even in samples of natural isotopic abundance.

As explained in detail in chapter 4 devoted to the WO relaxation, the NIR fluorescence spectra show that the WO vibrational relaxation is relatively slow even in excited electronic states, and not only $v' = 0$ but also vibrationally excited levels appear. In the case of the stronger $W^{18}O$ fluorescence levels up to $v' = 3$ are detected in emission, and the spectra can be detected with an InSb detector down to about 3300 cm^{-1} in the infrared, with the progressions in the ground state vibrational frequency extending up to $v'' = 5$.

State[a]	T_e [cm^{-1}]	ω_e [cm^{-1}]	$\omega_e x_e$ [cm^{-1}]
X $^5\Pi$	0.0	1064.47	3.998[b]
a ($^7\Pi$?, red site)[c]	7454.3	957.9	3.27
a ($^7\Pi$?)[c]	7578.6	959.6	3.76
b ($^7\Pi$?)[c]	7761.1	958.7	3.55
c ($^7\Pi$?)[c]	8062.1	956.1	3.26
d[c]	10938.7	1022.3	
e[c]	12075.4	970.5	
f[c]	14132.7	1084.3	
A ($^5\Sigma$ or $^7\Sigma$?)	14116.9	1051.2	10.84
B	17336.9	929.5	-1.07
C	19267.5	932.6	2.76
D (red site)	20799.8	996.8	8.22
D	20821.4	998.7	8.51
E	21538.2	971.3	8.49
F	23439.4	955.4	9.52
G	23852.7	934.2	-5.1
H’[cd]	27037.3	931.6	13.15

Table 3.1: Molecular constants of $^{184}W^{16}O$

---

[a] symmetries as proposed by Nelin & Bauschlicher [136].

[b] $\omega_e y_e = -0.0034$ for the X $^5\Pi$ ground state.

[c] previously not observed.

[d] not identical with Samoilova’s H state [135].

3.3.5 Electronic Structure of WO

The ab initio work of Nelin and Bauschlicher suggests a $^5\Pi$ ground state for WO, and their SCCI calculation predicts the lowest excited electronic state to be $^7\Pi$ near 7400 cm^{-1} . The work gives, however, no indication of the magnitude of the spin orbit multiplet splittings, which must surely be quite substantial. Thus the splitting between the two components of the X $^2\Delta$ ground state of TaO is over 3500 cm^{-1} [139]. Our fluorescence spectra and the vibrational relaxation process in the ground state give no direct evidence of any participation of the other components of the multiplet. The group of states in the infrared near 7500 cm^{-1} lies almost exactly at the energy predicted for the $^7\Pi$ state, but this may be at least partially fortuitous. The appearance of five different origins in this spectral range is due to the existence of WO in two distinct sites in neon; there are at least three different states in this range, and these may well be components of the multiplet state.

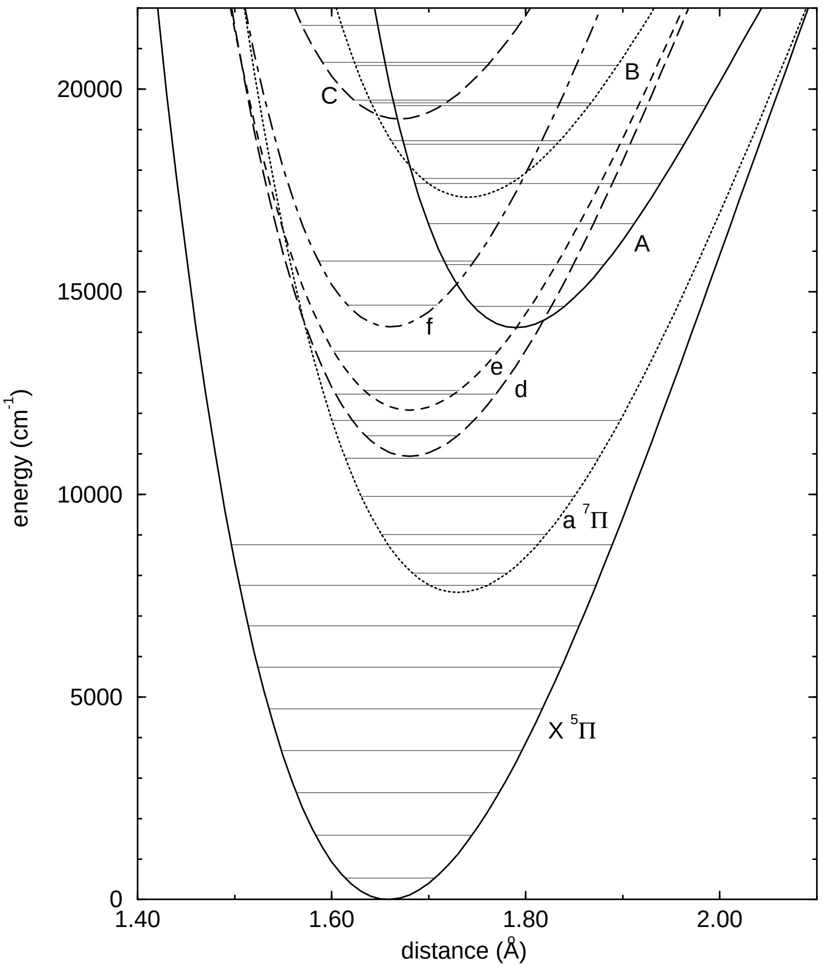

Figure 3.5: W^{16}O potential curves and vibrational levels in the range 0 - 22000 cm^{-1}. The r$_e$'s are obtained by Franck-Condon analysis or are taken, where available, from Samoilova et al. [135].

The theoretical work also predicts two additional states, $^5\Sigma$ and $^7\Sigma$, in the visible at 17500 and 16000 cm^{-1} , respectively. Our work, as well as the previous studies of WM and SEG, suggests a whole multitude of states in this spectral region. A list with all the molecular constants of WO observed in these experiments is given in Table 3.1 and a diagram of the WO energy level structure is presented in Fig. 3.5. A detailed interpretation and assignment of the states in this range would require more theoretical work, and in particular state-of-the-art calculations taking into account spin orbit interactions and other relativistic effects.

3.4 Infrared Absorption and Structure of WO_2

As noted before, Weltner and McLeod assigned in the matrix infrared spectrum bands at 928 (strong) and 992 cm^{-1} (medium), with counterparts in the ^{18}O experiments at 883 and 941 cm^{-1} , respectively, to ν_3 and ν_1 vibrational fundamentals of WO_2 . The same two absorptions were some 15 years later also detected by Green and Ervin [134]. These authors also assign two absorptions to the mixed $^{18}OW^{16}O$ in the heavier rare gas matrices, but fail to identify them in a neon matrix. They also comment on some inconsistencies in the assignment, with the ν_3 and ν_1 exhibiting unusual differential shifts from Kr to Ne matrices.

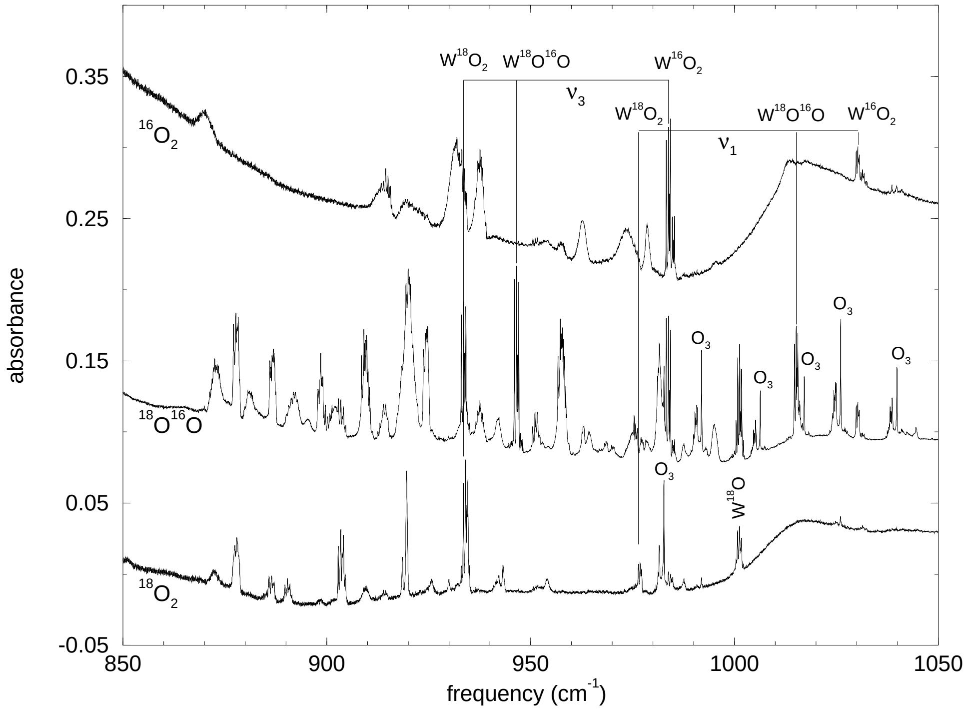

Figure 3.6: Infrared absorption of W_xO_y in neon. The three traces show the absorption spectra of different matrices using pure $^{16}O_2$ (top), a statistically scrambled mixture of $^{16}O_2$ and $^{18}O_2$ (50:50, middle), and pure $^{18}O_2$ (bottom).

The well-annealed samples produced by our pulsed deposition technique have the advantage of yielding a well-resolved isotopic structure, which is of great assistance in assigning the observed bands. In the top trace of Fig. 3.6 one can see a strong band at 984 cm^{-1} , which exhibits the distinct "fingerprint" of a species with a single W atom. All the major isotopic components are fully resolved (28.6% ^{186}W, 30.7% ^{184}W, 14.28% ^{183}W, and 26.3% ^{182}W, with the individual frequencies at 983.26, 983.87, 984.19 and 984.50 cm^{-1}), and the band shifts appropriately to 934 cm^{-1} in an experiment employing ^{18}O. On the other hand, the "strong" 928 cm^{-1} band of WM is not detected at all, with only a rather poorly defined broad feature with a maximum near 931 cm^{-1} appearing in this region. This feature, which appears with varying intensities relative to the 984 cm^{-1} band, is not consistent with assignment to WO_2 , and is likely to be due to a larger molecule with probably more than one tungsten atom.

If the WO_2 molecule were linear, centrosymmetric, then the symmetric ν_1 vibration would be infrared-inactive, but the observation of a long bending progression in the visible absorption spectrum, as well as our DFT calculations using GAUSSIAN 94 [40], indicate that WO_2 is bent, suggesting that the symmetric stretch should be observable.

A careful search of the spectra in Fig. 3.6 revealed a somewhat weaker band near 1030 cm^{-1} , shown in the top trace, which shifted to 977 cm^{-1} in an experiment using ^{18}O (bottom trace), with both bands again exhibiting the isotopic splitting signature of a compound with a single tungsten atom. The relative intensities of the features at 1030 and 984 cm^{-1} apparent in the spectra are consistent with the intensity ratio for ν_1 and ν_3 vibrations predicted by the density functional calculations (50 and 134 km/mol), and also the observed frequencies agree reasonably with the computed values of 1078 and 1023 cm^{-1} . The spectrum in the bottom trace of Fig 3.6 also shows weakly the $W^{16}O_2$ bands due to normal oxygen present as an impurity.

A normal coordinate analysis using the above values of ν_1 and ν_3 of both $W^{16}O_2$ and $W^{18}O_2$ predicted frequencies near 1015 and 945 cm^{-1} for the $^{18}OW^{16}O$ isotopic molecule. These absorptions were then indeed easily found and identified in experiments using a statistically scrambled mixture of $^{16}O_2$ and $^{18}O_2$. In a spectrum shown as the middle trace of Fig. 3.6, a 50:50 isotopic mixture was used, with complete scrambling being confirmed by the presence of all six possible isotopic species of ozone in the appropriate intensity ratios [140]. New bands due to $^{18}OW^{16}O$, which are completely absent in the experiments using either pure $^{16}O_2$ or unscrambled $^{18}O_2$ - $^{16}O_2$ mixtures, appear within a couple of wavenumbers of the predicted values. As expected for a statistical mixture, they are about a factor of two stronger than the absorptions of the pure isotopic species. Interestingly, in this case the ratio of the $\nu_3 : \nu_1$ intensities is only about two, which is undoubtedly the result of the isotopic asymmetry of the molecule. Due to the different masses, the two stretching frequencies partially uncouple, and have now to some extent the character of $W^{16}O$ and $W^{18}O$ stretching, rather than pure symmetric and asymmetric modes. The assignment of the $^{18}OW^{16}O$ bands is again unambiguously confirmed by their fully resolved tungsten isotopic structure.

We show several of the WO_2 bands at higher resolution in Fig. 3.7, identifying the tungsten isotopic species. As expected, the isotopic ν_1 symmetric stretching vibration exhibits a considerably smaller isotopic splitting than the asymmetric ν_3 . Shifted about one cm^{-1} to the blue of the highest frequency isotopic line (due to ^{182}W), one can see that the tungsten isotopic pattern is weakly repeated. This is due to a slightly blue-shifted minor site, which appears with a some-

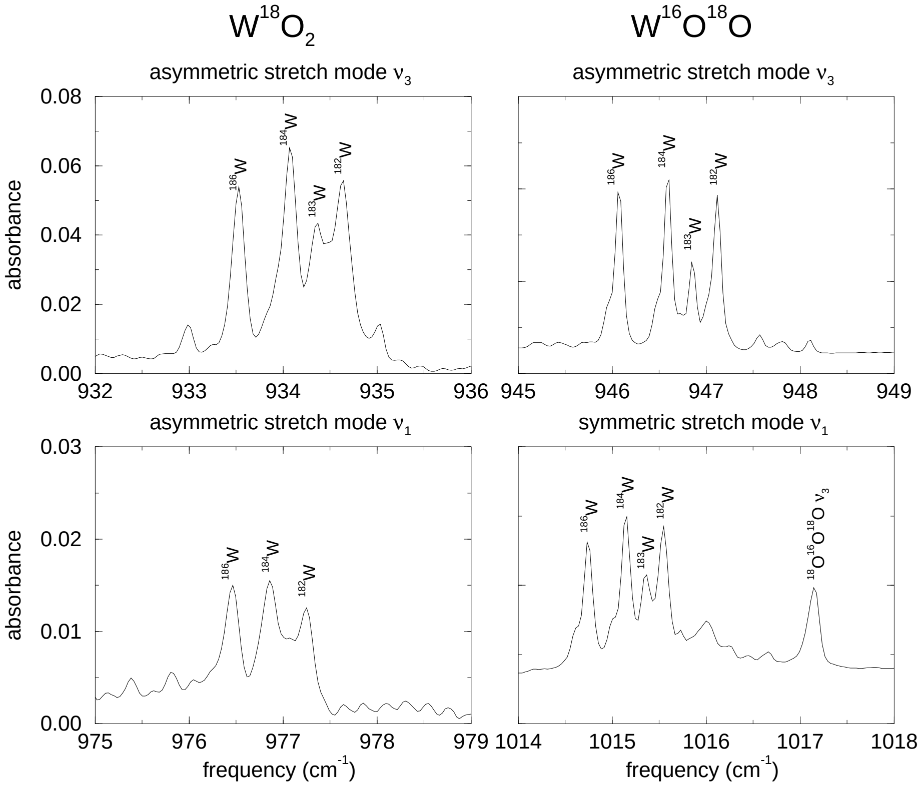

Figure 3.7: Enlargements of the ν_1 and ν_3 absorption bands of $W^{18}O_2$ and $W^{18}O^{16}O$. Here, one can see in detail the characteristic isotopic splitting of tungsten in the WO_2 molecule.

what variable intensity ratio relative to the major site, depending on the exact sample history and deposition conditions.

As noted above, if WO_2 were linear centrosymmetric, then the ν_1 vibration would be infrared-inactive in the pure isotopic molecules, and should also exhibit no tungsten isotopic splitting, since it involves no motion of the central tungsten atom. On the other hand, as the molecule becomes bent, the vibration gains activity and concurrently, the isotopic splitting should appear and increase, since the stretching mode now also involves a motion of the tungsten. The isotopic pattern and shifts are consequently a sensitive function of the bond angle, and we have included the measured ν_1 and ν_3 vibrational frequencies for all the twelve observed WO_2 isotopic species in a global adjustment of the force constants. It turned out that the observed isotopic shifts could indeed be correctly reproduced only with the OWO angle in the range of 95-105°. This is in excellent agreement with the 104° value predicted by our DFT calculation for the bonding angle in the WO_2 ground state.

We list the observed vibrational frequencies of the WO_2 stretching vibrations of the nine major WO_2 isotopic species in Table 3.2. The global fit of the vibrational spectrum data yields force constants of $k_r = 8.812$ mdyne/Å and $k_{rr} = 1.892$ mdyne/Å, which reproduce all the combined isotopic data (for 12 isotopic species) with an rms deviation of less than 0.6 cm^{-1} .

isotopic composition	ν_1 vibration		ν_3 vibration	
	calc.	obs.	calc.	obs.
16-182-16	1031.46	1030.64	984.36	984.31
16-184-16	1031.10	1030.25	983.83	983.79
16-186-16	1030.75	1029.88	983.31	983.28
16-182-18	1016.15	1015.55	946.92	947.12
16-184-18	1015.75	1015.14	946.39	946.59
16-186-18	1015.37	1014.74	945.88	946.08
18-182-18	976.47	977.25	933.83	934.64
18-184-18	976.09	976.86	933.28	934.08
18-186-18	975.71	976.46	932.73	933.53

Table 3.2: Comparison of observed and fitted frequencies (in cm^{-1}) of the ν_1 and ν_3 vibrations of the major WO_2 isotopomers

Even more importantly, the tungsten isotopic shifts are reproduced to 0.02 cm^{-1} , that is basically within the experimental accuracy limited by the observed widths of the isotopic lines. The computed stretching force constant is only slightly lowered compared with that of the diatomic oxide, $k_r = 9.679$ mdyne/Å. A comparison of our experimental and theoretical constants of WO_2 with the results of Weltner and Green is summarized in Table 3.3.

	Neon (this work)	Neon (Weltner [133])	Krypton (Green [134])	Theory[1] (DFT, this work)
$\nu_1[\text{cm}^{-1}]$	1030.2	992	975.5	1078
ν_2 $[\text{cm}^{-1}]$	≈380 [2]			378
ν_3 $[\text{cm}^{-1}]$	983.8	928	937.2	1023
∠(OWO)	99°		114°	104.4°
r(O-W) [Å]				1.686
k_r [mdyne/Å]	8.812		7.961	
k_{rr} [mdyne/Å]	1.892		0.581	

Table 3.3: Comparison of molecular monstants of the $^1A_1$ ground state of $^{184}W^{16}O_2$

---

[1] calculations were performed with Gaussian94 [40] using the B3LYP method with the LanL2DZ relativistic-core-potential basis set and additional d orbitals for the oxygens resulting in a singlet A_1 symmetry for the ground state.

[2] obtained from a progression in the bending vibration in the extremely broadened emission of WO_2 after excitation of the A state at 12670 cm^{-1} .

3.5 Summary

Absorption and fluorescence spectra of WO and WO_2 were investigated in the spectral region ranging from the infrared to the UV. Besides the WO states previously detected by Weltner and McLeod, several other states were identified in the near infrared range. Due to the unusually slow relaxation of the diatomic oxide, there is observed, besides fluorescence from several visible electronic states, emission from the low lying electronic states in the infrared, and extensive ground state vibrational emission is observed, providing a wealth of spectroscopic information, and spectroscopic constants of nearly unprecedented accuracy for a matrix molecule. Spectral lines of tungsten oxides in solid neon are unusually sharp, so that even the tungsten isotopic structure is clearly resolved. This facilitates the assignments and analysis of the spectra, and allowed us to identify in the infrared spectrum unambiguously the symmetric stretching vibration ν_1 of WO_2 . The spectroscopic information thus obtained is analyzed, discussed and tabulated.

Chapter 4

Relaxation and Vibrational Fluorescence of WO

Studies of laser induced fluorescence of tungsten oxides in solid neon at 6 K provide interesting insights into the mechanisms of WO relaxation. The relaxation occurs by inter-electronic cascade between the vibrational manifolds of excited electronic states, reaching eventually the $v = 7$ of the ground electronic state. Remarkably, for the heavy WO oxide the non-radiative processes are surprisingly inefficient, with relaxation in the ground state apparently occurring predominantly by sequential vibrational fluorescence. The relaxation pathways of WO are discussed and compared with relaxation in lighter, first row molecules exemplified by CN.

4.1 Introduction

Low temperature rare gas solids are a very useful medium for studies of molecular relaxation and non-radiative processes [141, 142, 143, 60]. While relaxation in the condensed phase is usually fast, often proceeding on a picosecond or even sub-picosecond timescale, at low temperatures in solid rare gases it often slows down remarkably. In small molecules often vibrationally unrelaxed hot electronic fluorescence is observed, and in particular in the ground states of light molecules the nonradiative relaxation may be very slow. In a number of light molecules, mostly involving hydrides or simple compounds of first row elements, vibrational fluorescence was also observed and investigated [144, 145, 146, 147, 62, 148]. The diatomic CN is an example of a molecule which exhibits a very slow relaxation and for which intense vibrational fluorescence is observed [149].

Relaxation for molecules involving heavier elements is usually very efficient, and even in electronic spectra one mostly sees only vibrationally relaxed fluorescence or phosphorescence. Particularly in transition metals, with their dense manifold of electronic states, fast relaxation is usually the rule, and only in relatively few cases is extensive hot fluorescence detected. The spectroscopy and photophysics of the oxides of the third row transition metal tungsten were examined in detail in Chapter 3. Rather surprisingly we have observed that, in spite of the essential differences between the two molecules, the energy relaxation in WO parallels the processes previously detected in CN [64, 150]. Extensive vibrationally unrelaxed emission from several electronic states is observed, and even more surprisingly, quite intense ground state vibrational fluorescence is easily detectable. Our observations of the WO relaxation behavior are the subject of this chapter.

4.2 Experimental

Tungsten and its oxides are high-melting, refractory materials, and their vaporization required temperatures ranging up to 3000 K. We here employ a technique developed in our laboratory more than a decade ago [70], laser vaporization of the metal in the presence of a large excess of cold carrier gas, neon gas being used to grow the matrix. The frequency-doubled pulses of an Nd-YAG laser (30 mJ) used to vaporize a tungsten target are synchronized with the opening of a fast valve admitting pulses of the carrier gas. The valve with opening times of 0.1 ms is operated with a backing pressure of 5 bar of a 500:1 mixture of neon with O_2 (or $^{18}O_2$). The neon gas with the products and oxides formed in the vaporization fixture are then condensed on a 6 K silver coated copper substrate.

The deposits are examined spectroscopically with the help of a Bruker IFS 120 HR FT instrument with a spectral range from 500 to 30 000 cm^{-1}. Spectra have been recorded with resolutions of 0.5 cm^{-1} and 0.06 cm^{-1} (IR). To excite the sample fluorescence, either an argon ion laser pumped dye laser, or a Ti-Sapphire laser were used. A PMT detector was used in the visible and UV range, while germanium and indium antimonide detectors were available for studies in the near infrared range.

4.3 Results and Discussion

4.3.1 Fluorescence and Relaxation of the Excited WO Electronic States

Fluorescence spectra can often provide a valuable complementary contribution to absorption studies. As explained in the experimental section, we have used our tunable laser sources to excite the neon matrix absorptions due to WO. Such an excitation at a variety of frequencies ranging from about 10000 to 25000 cm^{-1} resulted in a fairly strong visible and near infrared fluorescence, whose intensity and spectral distribution depended sensitively upon the excitation wavelength, and upon the isotopic species excited. While some levels were emitting efficiently, others were conspicuously absent, indicative of a complex isotopically dependent pattern of relaxation. This relaxation process is quite complex, and involves vibrational manifolds of the numerous electronic states present in this region, both those observed in absorption, and probably of other, "dark" states. Rates of such interelectronic relaxation processes are known to depend sensitively upon the quantum mechanical coupling between the different electronic states, but also on the "energy gap" between the relaxing levels, and are often governed by the presence of accidental resonances or near resonances.

When the lower energy levels at the red end of the spectrum reported by Weltner [133] are excited, the fluorescence is relatively simple and easy to understand. Thus exciting the sample in the $v = 0$ level of the W^{18}O in the B state of Weltner at 17273.9 cm^{-1} , one observes emission from the excited level into $v'' = 0$, 1, and 2 levels of the ground electronic state, as can be seen in the lower trace of Fig. 3.3. A further progression originating from a level at 16980.4 cm^{-1} into the $v'' = 1 - 4$ ground state levels can also easily be identified as being due to the $v' = 3$ A state level, 293.5 cm^{-1} lower in energy. The 19680.44 cm^{-1} is also seen weakly in absorption, although not previously observed by Weltner. Excitation of the corresponding $v' = 0$ B state level of W^{16}O (17280.5 cm^{-1}), on the other hand produces almost no B-state emission, but mainly weak emissions from the $v' = 3$ and 2 A-state levels. Owing to the isotopic shift, in the W^{16}O the $v' = 3$ A level is only 150 cm^{-1} below $v' = 0$ B, and the smaller energy gap results in a more efficient depopulation of the B state.

As one proceeds towards higher energies, the fluorescence gets progressively more complex. As one can see in Fig. 4.1, excitation of the $v' = 2$ D (22635.9 cm^{-1}), produces not only a weak resonant emission from the excited level, but extensive relaxed fluorescence from a number of other levels. No emission is seen from $v' = 1$ D, but several bands originating from $v' = 0$ E (21493.0 cm^{-1}) and a fairly strong progression from $v' = 0$ D (20789.3 cm^{-1}), and a weaker one from $v' = 0$ B (17274.1 cm^{-1}). Another rather long progression originates from the A6 level (19675.5 cm^{-1}), and extends down to 11867.9 cm^{-1} into the $v'' = 8$ ground state. In addition to the clearly identifiable progressions, numerous very weak, sharp bands are observed confirming that in addition to states previously detected by Weltner, several other "dark" or very weakly absorbing states must be present in this region, and participate in the relaxation process.

It may be noted that some weak bands appearing in the absorption spectrum are due to "site effects". The bands due to "sites" are, however, easily identified, since unlike excitation of WO in the "main" site, their excitation results in spectrally shifted emission bands. Thus all the bands of the D progression exhibit a much weaker satellite some 24 cm^{-1} lower in energy, whose

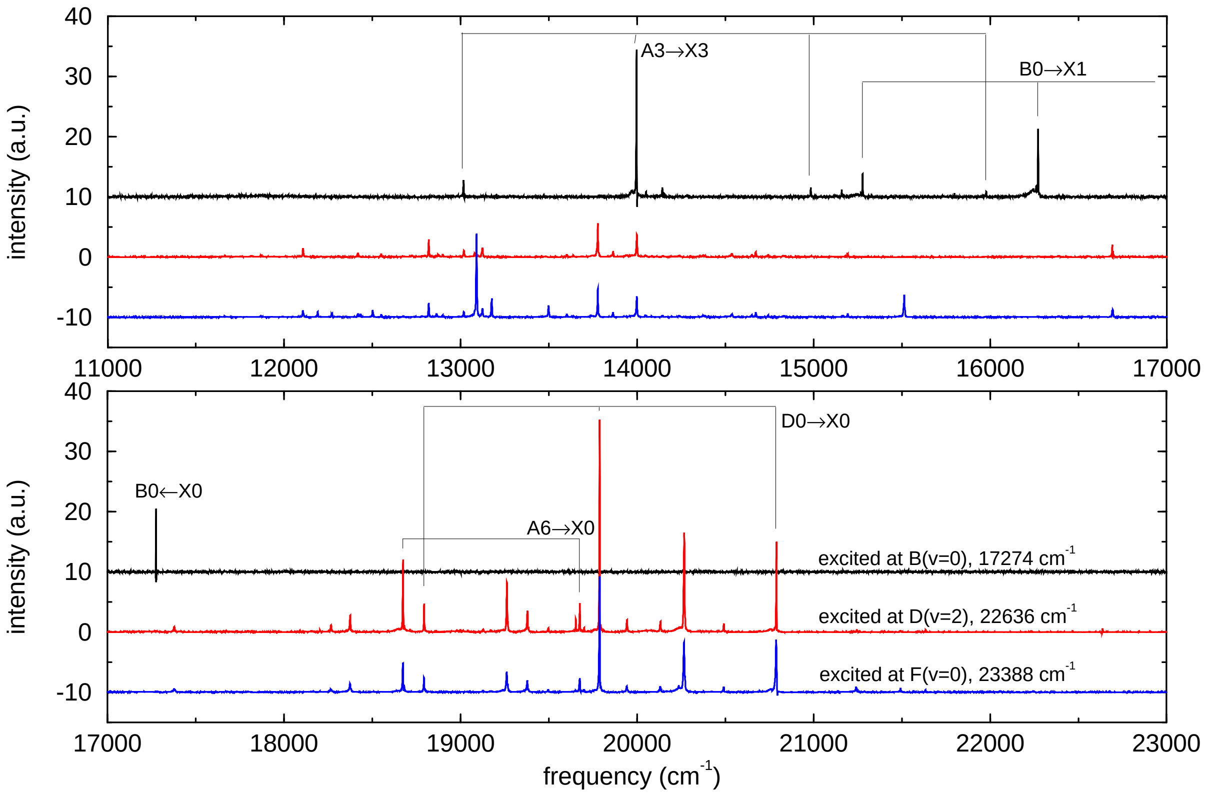

Figure 4.1: Laser induced fluorescence spectra of $W^{18}O$ excited at $v = 0$ B (top), $v = 2$ F (middle) and $v = 0$ F electronic state (bottom). The most prominent progressions which could be assigned to known states are shown.

excitation produces fluorescence bands uniformly shifted by the same 24 cm^{-1}.

4.3.2 Infrared Phosphorescence

When the visible bands are excited, one observes not only visible fluorescence, but also a strong emission in the near infrared range, clearly due to the band system also observed in absorption. Representative spectra obtained with the Ge detector by tuning the exciting laser to the B-X 0-0 transition (B0 band) at 17281 and 17274 cm^{-1} for $W^{16}O$ and $W^{18}O$, respectively, are shown in Fig. 3.4. Unlike the visible fluorescence, the emission appearance is essentially independent of which of the vibronic bands of the visible or near IR progressions is excited by the laser, and from the multiple "systems" detected in the absorption spectrum, only the strongest one with its origin at 7527.6 cm^{-1} appears. As already noted above, it may be due to the "spin forbidden" phosphorescence from the $^7\Pi$ state , although Λ is probably not well defined in a molecule as heavy as WO. In contrast with the visible fluorescence, the near infrared emission is relatively simple, and easy to analyse to yield the molecular constants of the "a" state. Interestingly, the infrared spectrum is at least one order of magnitude more intense in the heavier $W^{18}O$ isotopic molecule, which appears with appreciable intensity even in the natural isotopic abundance samples.

The spectra show that vibrational relaxation of WO in neon is relatively slow even in the electronically excited "a" state, since not only $v' = 0$, but also emission originating from vibrationally unrelaxed levels is observed. In the case of the stronger $W^{18}O$ fluorescence, levels up to $v' = 3$ are detected in emission, and the spectra can be followed with an InSb detector down to about 3300 cm^{-1} in the infrared, with the progressions in the ground state vibrational frequency extending to $v'' = 5$. The relaxation of the lighter $W^{16}O$ is apparently more efficient, and the corresponding emission appreciably weaker. In this case, besides the vibrationless level only $v' = 1$ emission is observed.

4.3.3 Vibrational Fluorescence of WO

At the very red end of the spectrum obtained with the indium antimonide detector one can observe starting at around 3000 cm^{-1} a slowly rising background, which reaches a maximum near 1900 cm^{-1} and then drops to zero due to a cutoff of the InSb detector, see Fig. 4.2. This broad maximum is clearly due to the high energy end of "black body" radiation from the room temperature apparatus walls. Superimposed over this maximum one can see in the experiment employing natural abundance oxygen three strong absorptions at 2312.4, 2330.6 and 2347.4 cm^{-1}, as well as a group of eight moderately strong emission bands at 1991.5, 2007.8, 2024.1, 2040.4, 2056.6, 2072.7, 2088.8 and 2104.9 cm^{-1}. The three absorption bands are clearly due to three isotopic species of carbon dioxide, $C^{18}O_2$, $^{16}OC^{18}O$, and $C^{16}O_2$, probably formed due to oxygen reaction with a minor carbon impurity in the tungsten target.

The emission bands are readily identified as vibrational overtone fluorescence of diatomic WO, with the eight strong bands being the 9-7, 8-6, 7-5, 6-4, 5-3, 4-2, 3-1 and 2-0 transitions, and in addition, also the very weak 10-8 bands are detected. This assignment is quite unambiguous, and is further confirmed by the clearly resolved tungsten isotopic structure. In an experiment with 18-oxygen, the appropriately shifted 7-5, 6-4,... , 2-0 bands are observed. A careful examination of the region around 3000 cm^{-1} revealed also the $\Delta v = 3$ sequence. Finally, as one can see in Fig. 4.3, the $\Delta v = 1$ transitions could easily be observed between 1000-1100 cm^{-1} using a mercury-cadmium telluride detector.

Several additional observations can be made in connection with these IR emission spectra. In the first place, it appears that besides inefficient relaxation, there is also little evidence of energy transfer between the WO molecules. In the case of long lived vibrationally excited molecules one often observes rather efficient energy transfer, evidenced by accumulation of the excitation in the heavier isotopic species, e.g. $C^{18}O$ or ^{13}CN [62]. The low temperature of the matrix favors exothermic processes, resulting in the flow of energy to the heavier isotopomers with smaller vibrational spacing. Examination of the spectrum indicates that the isotopic ratios from the highest level observed, $v'' = 8$, down to $v'' = 2$ remain relatively constant.

In the second place, the rates of nonradiative vibrational relaxation usually increase rapidly with increasing vibrational quantum number. If the observed sequence of $\Delta v = 2$ bands was the result of a competition between radiative and nonradiative processes, one might expect the intensity of the emission bands to decrease with the increasing vibrational quantum number, as the higher levels are progressively more efficiently depopulated nonradiatively. The fact that the

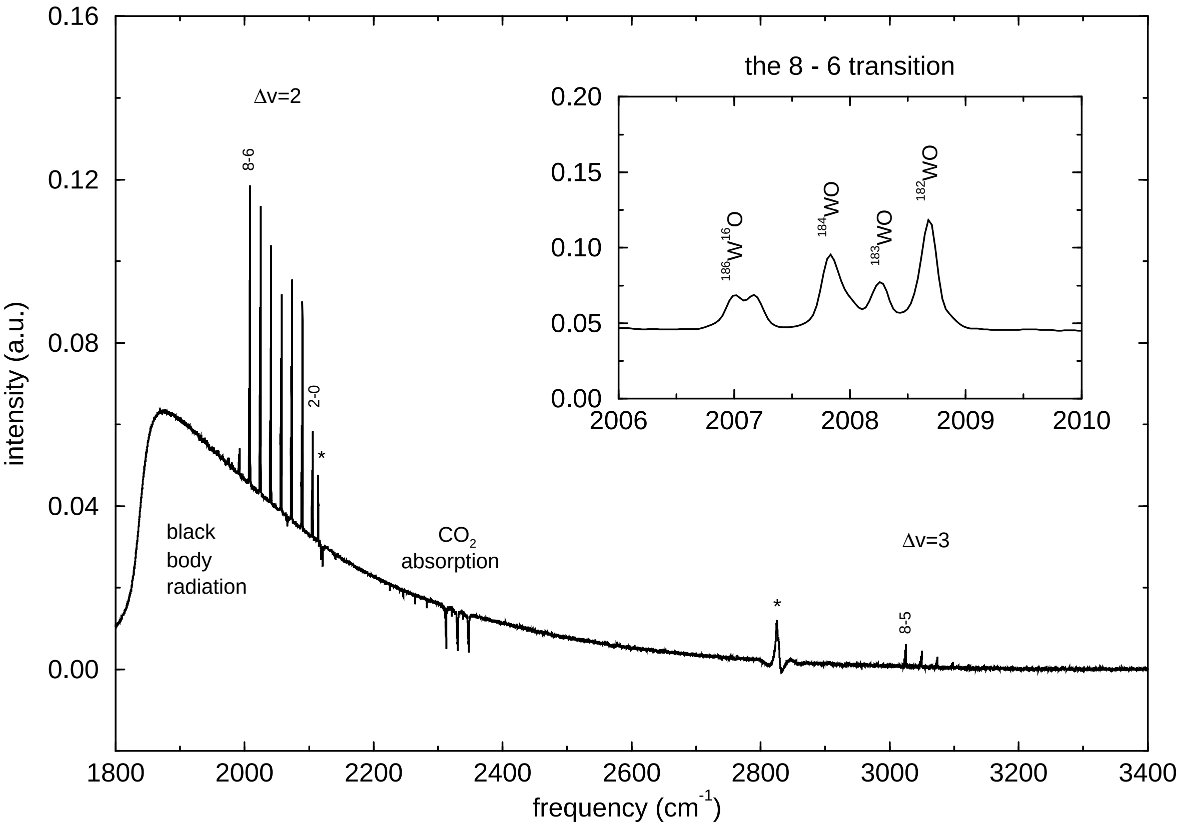

Figure 4.2: Vibrational overtone fluorescence of W^{16}O. The main trace displays the $\Delta v = 2$ and the weaker $\Delta v = 3$ transitions of ground state W^{16}O in solid neon. Superposed by black body radiation, the 9-7, 8-6,... ,2-0 bands are easily observed. The 8-5, 7-4, 6-3 and 5-2 transitions appear near 3000 cm^{-1} with about one order of magnitude weaker intensity. The insert shows the strong 8-6 transition with tungsten isotopical resolution. Peaks denoted with an asterisk are probably due to impurities.

intensities are from $v'' = 8$ down to $v'' = 2$ relatively constant would seem to suggest that the relaxation in the WO ground state may be purely radiative.

A third observation involves the doubling of all the bands due to the ^{186}WO isotopic molecule, see the insert in Fig. 4.2. This doubling into two bands with comparable intensities separated by about 0.2 cm^{-1} is quite reproducible, and is observed for both oxygen isotopic species. We have at this point no explanation for the origin of this doubling. All three major isotopic species of tungsten ^{182}W, ^{184}W, and ^{186}W have a nuclear spin of 0.

As noted above, the visible bands of WO exhibit, in agreement with Weltner, strong interstate interactions and perturbations, so that only the W^{18}O spectrum can be reasonably fitted to obtain the spectroscopic constants of the excited states. On the other hand, employing the appropriate isotopic relationships, the ground state vibrational data including some 80 transitions for eight different isotopic species of WO, and involving levels up to $v'' = 9$, can be almost perfectly fitted. A Morse potential with ω_e = 1064.65 cm^{-1} and $\omega_e x_e$ = 4.046 cm^{-1} (for the ^{184}W^{16}O isotopomer)

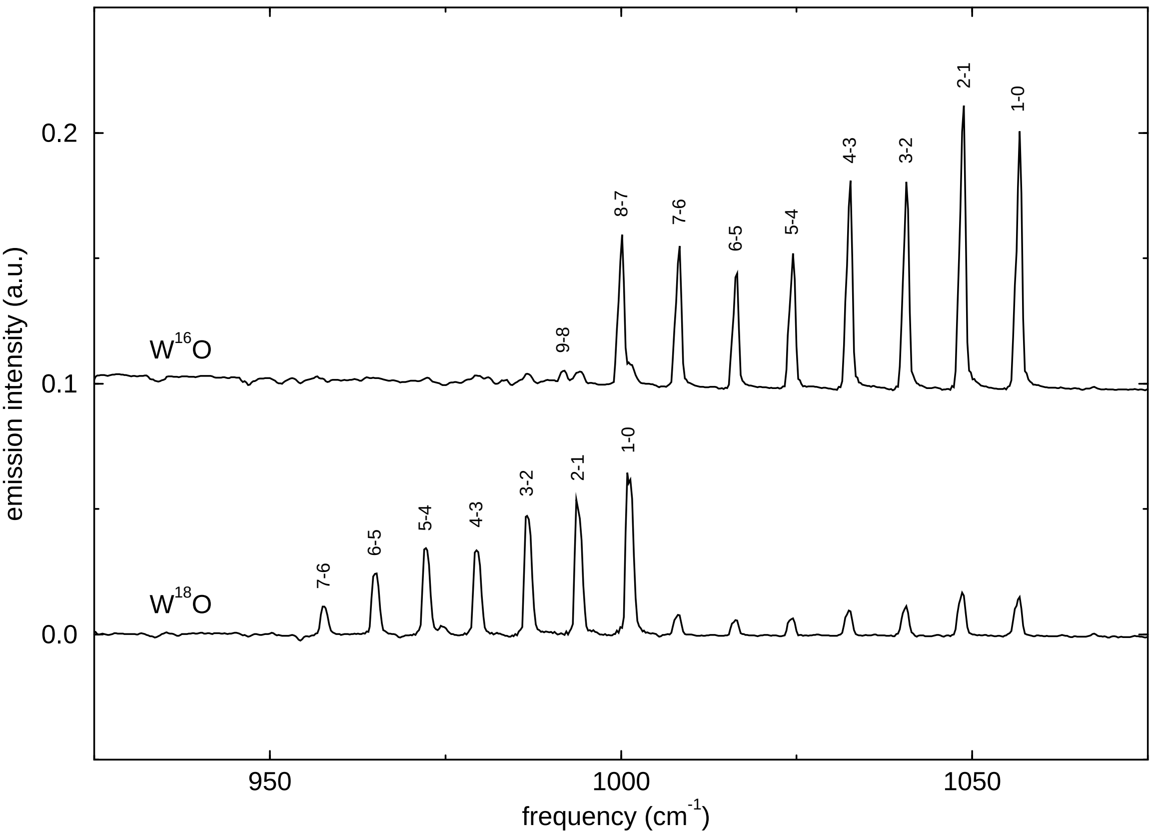

Figure 4.3: Vibrational fluorescence of tungsten oxide in neon. The two traces show the $\Delta v = 1$ ground-state emission of $W^{16}O$ and $W^{18}O$ after excitation at B $v = 0$. The spectra, measured with a mercury cadmium telluride detector, are background corrected by subtracting the dominating black-body radiation.

reproduces the observed levels with a RMS deviation of <0.09 cm^{-1}. While a somewhat better fit (RMS < 0.03 cm-1) is obtained with $\omega_e y_e$ = -0.0034 cm^{-1} (the other constants change slightly to ω_e = 1064.49 cm^{-1} and $\omega_e x_e$ =3.998 cm^{-1}), inclusion of $\omega_e z_e$ or higher terms results in no further improvement.

4.3.4 X-State Vibrational Relaxation of WO

The observation of ground state vibrational fluorescence of WO is rather surprising for at least two reasons. In the first place, while one occasionally observes vibrationally unrelaxed fluorescence in electronic transitions of similar matrix isolated small metal containing molecules, such observations in the infrared are quite uncommon. In view of the much lower oscillator strengths and longer radiative lifetimes associated with vibrational transitions, vibrational fluorescence is usually observed only for hydrides and very light molecules involving first row atoms, with high vibrational frequencies usually above 1500-2000 cm^{-1}. In the second place, the ground state potential of WO is relatively harmonic, and therefore one might not expect strong overtone transitions.

Unfortunately we are not equipped for the direct measurement of the vibrational lifetimes. Estimating absolute emission quantum yields is always difficult, but semiquantitative consideration of the observed band intensities suggests that it is very high, and that for every excited molecule several IR photons may be emitted. Such a high quantum yield of vibrational emission indicates that the nonradiative relaxation of WO ground state vibrational levels must be exceedingly slow. The fact that they are long in the WO case is, however, also demonstrated by the fact that absorptions originating in excited vibrational levels can easily be detected. An inefficient energy transfer between the light neon atoms and the much heavier WO molecule might be a contributing factor. In many molecules where strong vibrational fluorescence is observed, e.g. OH, NH, CH_3F or hydrogen halides, it has been demonstrated that the relaxation involves a V-R process, with the rotational modes of the guest molecule being the primary acceptors of the vibrational energy [151]. The rotational constants of WO are very much smaller ($B_e \approx 0.415$ cm^{-1}) and the rotations probably contribute little, since very high rotational levels would have to be involved.

The appearance of the overtones in the vibrational spectrum will, of course, be aided by the v^4 dependence of the coefficient of spontaneous emission, which will favor the $\Delta v = 2$ and 3 transitions by factors of 16 and 81, respectively, and thus counteract the harmonic oscillator selection rules. Even though the mechanical anharmonicity of WO is small, the overtones can be favored by electric anharmonicity. The WO molecule may be fairly ionic, but at larger distances it dissociates into neutral atoms, and its dipole is surely not a linear function of r.

To the best of our knowledge, vibrational infrared emission from small metal compound molecules has previously not been detected. The observed relaxation processes, where absorption of a single visible photon is followed by emission of a series of IR photons seems thus far to be unique. It may be noted that similar processes, that is UV pumping, followed by an internal conversion and ground state vibrational fluorescence are thought to be responsible for the so-called unidentified infrared emission bands (UIE), with polycyclic aromatic hydrocarbons (PAH) beeing the suggested carriers [152, 153]. The search for emission of these species in neon matrix might be of interest. The excellent signal to noise ratio, and clearly high quantum yields of infrared fluorescence observed in WO raise the question if such a behavior might not be much more widespread, and if studies of vibrational emission could not provide a useful general tool for characterizing small metal oxides, carbides or nitrides.

4.3.5 Pathways of Relaxation of WO in Solid Neon

One of the molecules for which strong infrared emission has been detected, and whose relaxation in matrices has been most extensively investigated is probably the CN radical. Even though the properties and electronic structures of the two molecules could hardly be much more different, and while WO has a vibrational frequency about half of that of CN, the relaxation pathways of the two molecules in the matrix are remarkably similar. In the higher energy region, the relaxation proceeds in both molecules by an interelectronic process involving the vibrational manifolds of several excited electronic states. Thus as in the CN the excitation zig-zags between the B $^2\Sigma$ and A $^2\Pi$ electronic states [150], also WO cris-crosses in the visible between the several electronic states available at that energy. This relaxation behaviour is shown schematically in Fig. 4.4. The nonradiative interelectronic transitions are dominated by accidental level degeneracies and the rates are governed by Franck Condon factors and the energy gap law.

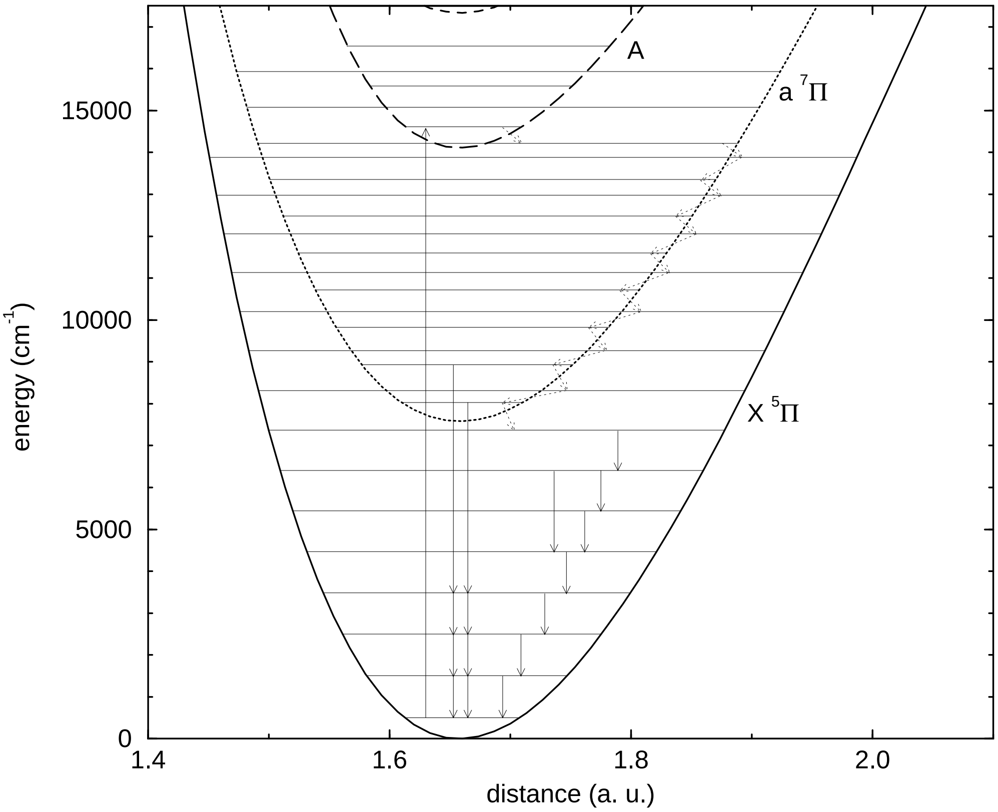

Figure 4.4: Schematic relaxation pathways of W^{18}O in solid neon after excitation of the A $v = 0$ state. Solid arrows denote radiative transitions, whereas dotted arrows denote nonradiative transitions. For the sake of simplicity, several low-lying electronic states were ommited.

When the lowest excited electronic state, the A $^2\Pi$ state in the CN or the "a" WO state is reached, the process slows down further, and in both molecules extensive vibrationally unrelaxed, "hot" emission, is observed [64]. In CN it was shown that rather than proceeding directly down the vibrational manifold of the A state, further relaxation occurs exclusively by repeated crossings between the vibrational levels of the A $^2\Pi$ state, and the nearest X $^2\Sigma$ ground state levels. Similarly it is almost certain that also in the lowest a ($^7\Pi$?) excited state of WO the relaxation proceeds by an interelectronic mechanism. In the light CN molecule the A $^2\Pi$ spin orbit constant is relatively small (A= -52.64 cm^{-1}), with relaxation between the components being extremely fast, and the splitting has little effect upon the relaxation in the matrix. While in WO the spin orbit effects are surely much larger, and the components of the widely separated "septet" state could be involved in the relaxation, it appears very likely that here ground state levels are involved, too.

After the relaxation reaches the vibrationless $v' = 0$ level of the lowest electronically excited state, only one intramolecular nonradiative process is possible: crossing into one of the nearby ground state levels. From that point on the interelectronic channel is closed, and the molecule can only relax intrastate, either nonradiatively, or by emitting infrared photons. Thus in the case of CN, the $v'' = 4$ X $^2\Sigma$ ground state level is populated from $v' = 0$ A $^2\Pi$. Further relaxation proceeds by sequential infrared fluorescence, and the ground state $v'' = 1 - 4$ levels appear strongly in emission. In $W^{18}O$ the vibrationless $v' = 0$ a ($^7\Pi$?) level occurs 7529.39 cm^{-1} above the X $v'' = 0$ level, with the nearest ground state vibrational level being at 6857.7 cm^{-1}, 671.69 cm^{-1} lower in energy. Quite analogous to the CN relaxation, as discussed above, the highest level from which vibrational infrared fluorescence is observed is $v'' = 7$. Clearly also here further relaxation apparently occurs by sequential vibrational fluorescence.

As noted above, in contrast with the heavier isotope, in $W^{16}O$ the a-state emission is weaker, and conversely, the vibrational emission considerably more efficient. An explanation is easily found by examining the vibrational level structures of the two oxygen isotopic species, which also provides further support for the relaxation in the lowest a ($^7\Pi$?) proceeding, as in CN, via the ground state vibrational levels. While in $W^{18}O$ the $v' = 0 - 3$ are located 671, 623, 576 and 526 cm^{-1} above the closest ground state level, for $W^{16}O$ the numbers are 300, 252, 205, and 158 cm^{-1}, see Fig. 3.5. This provides an easy explanation for the fact that stronger emission and more extensive vibrationally unrelaxed fluorescence are observed in the heavier $W^{18}O$ molecule. The smaller energy gaps in $W^{16}O$ result in a much more efficient relaxation into the ground state vibrational manifold, while conversely the larger gaps in $W^{18}O$ lead to enhanced phosphorescence, bypassing the excited ground state levels.

The involvement of the ground state in a-state relaxation is then directly evidenced by the observation of emission from levels above $v' = 0$ a ($^7\Pi$?). As noted above, also $v' = 8, 9$, and very weakly also $v' = 10$ X levels, located 779, 740, and 701 cm^{-1} above the $v' = 2$, 1 and 0 a state levels, are seen in emission in $W^{16}O$. These relatively large "energy gaps", combined with poor Franck Condon factors make reverse transition into the a-state once the crossing into the X-state has occurred inefficient, and vibrational emission becomes competititve. On the other hand, in the heavier isotope the corresponding gaps are only 360, 320, and 280 cm^{-1}, respectively. This makes the reverse crossing into the a-state more efficient compared with direct sequential radiative vibrational relaxation within the ground state.

4.3.6 Intrastate vs. Interstate Relaxation

As described above, the relaxation in the quite dissimilar molecules, CN and WO, proceeds in both cases via the same interelectronic mechanism, and similar observations have been made for a variety of other systems. In fact, even when the energy gaps for the two processes are comparable, the interstate process is in general much more efficient. As explained previously, the physical reasons are to be found in Franck Condon arguments applied to the local phonon modes, and to the response of the lattice to the change of state of the guest. The nearby lattice atoms experience little change when the guest molecule changes its vibrational state. This is evidenced by vibrational spectra of guest molecules, which mostly exhibit only strong "zero phonon lines", and little evidence of phonon sidebands.

On the other hand, the electron density distribution in the neighborhood of the guest molecule changes much more drastically when an electronic transition takes place, for instance from a Σ to a Π state. This again is usually evidenced by the much more prominent phonon sidebands associated with electronic transitions. Thus in the optical A $^2\Pi$ (unknown char) X $^2\Sigma$ transition in matrices, rather strong phonon sidebands are observable. In the case of WO, the phonon wings are weaker, but clearly observable. These same Franck Condon factors which channel energy into the lattice phonons during optical transition between the two electronic states also facilitate the corresponding nonradiative relaxation process.

4.4 Summary

Pathways of relaxation of electronically excited WO molecules in solid neon at 6 K were investigated. In spite of the much lower vibrational frequency, and entirely dissimilar molecular properties and structure, the pattern of relaxation processes resembles those found in the much lighter CN radical. The relaxation occurs by interelectronic cascade between the vibrational manifolds of excited electronic states, reaching eventually the $v'' = 7$ of the ground electronic state. The nonradiative processes in the ground state are surprisingly inefficient, with relaxation apparently occurring predominantly by sequential vibrational fluorescence.

Part III

Rare Gas Compounds

Chapter 5

Photodissociation of Hydrogen Halides

> *Wer es einmal soweit gebracht hat, daß er nicht mehr irrt,*
> *der hat auch zu arbeiten aufgehört.*
>
> MAX PLANCK

Spectra of hydrogen halides, their oligomers and complexes with the heavier rare gas atoms, xenon and krypton, and their photolysis were investigated. The monomers exhibit rotational spectra with a prominent broad R(0) line, and very sharp, weak Q(0) line. Their rotational constants are considerably lowered compared with the gas phase. The YH species hydrogen bond readily to form rigid oligomers or complexes with Xe or Kr, which in general exhibit sharp zero phonon line spectra of nonrotating molecules, with clearly resolved halogen isotopic structure. The nonrotating polymers photolyse at 193 nm more efficiently, but the $\mathrm{YH}\cdots\mathrm{Rg}$ complexes less efficiently than the monomers, with the photolysis of the dimers yielding $\mathrm{BrH}\cdots\mathrm{Br}$ “hydrogen dihalide” products. Annealing and diffusion result in formation of the HXeY rare gas compounds, and partial recovery of the YH monomers, but only very weak reformation of the $(\mathrm{YH})_n$ oligomers. The mechanisms of the photolysis, annealing and diffusion processes are discussed.

5.1 Introduction

Solvents have a considerable effect upon the dynamics and photochemistry of dissolved species, and the weakly interacting low temperature rare gas matrices provide a very simple model system for both experimental [154, 155] and theoretical [156, 157, 158, 159] investigations of these effects. The condensed environment provides an energy sink for dissipating the excess energy of a photoexcited molecular or atomic guest, and the solvating shell can affect, and in fact prevent molecular photodissociation. Early studies of this "cage effect", for instance in halogens in rare gases, have revealed that even for moderately high energy excess of 2-3 eV the caging is in many cases essentially complete, and no detectable permanent dissociation takes place. On the other hand, already the trailblazing experiments of Milligan and Jacox have shown that with a sufficiently large energy excess the cage effect can be overcome, and at least atomic hydrogen can exit the lattice cage [160]. In fact, one of the standard methods for generating a variety of radicals and other transient species is to select a precursor containing one more hydrogen atom than the desired target molecule, and subjecting it to vacuum UV photolysis, usually with the α-Lyman 121.6 nm hydrogen line.

The widespread availability of intense, energetic UV sources, coupled with progress in computer hardware and software permitting now meaningful theoretical modelling of many body systems and their dynamics, have led to renewed interest in the cage effect [158, 161, 162]. While guest molecules or atoms in solid rare gases represent particularly simple, tractable systems [17], the importance of cage effect studies extends well beyond low temperature matrices, and has implications for the photochemistry of solutions, radiation damage in solids, and many other phenomena of considerable practical importance.

Most of the studies thus far have treated the simplest systems: a molecular guest present in the host lattice as an interstitial or much more often substitutional impurity [163]. When one deals in the matrix with strongly interacting systems, for instance hydrogen bonded species such as hydrogen halides, preparing truly isolated molecules is a non-trivial task, and unless one takes special precautions, and goes to extremely low concentrations, an isolated single substitutional impurity is more an exception than the rule. Even at dilutions of $1{:}10^4$ a significant fraction of the guests tends to be complexed, dimerized or polymerized. The spectroscopy of hydrogen halides and their oligomers has been rather extensively studied, in particular in the heavier rare gases - argon, krypton and xenon [164, 165, 166]. It has also been noted that the dimerization has a considerable effect upon the guest dynamics: nonradiative relaxation processes are in general strongly accelerated, and in fact dimers become the sinks for vibrational energy. In the present paper we focus on a different aspect of the dimer or complex dynamics: on the effect of the hydrogen bond upon the cage effect and the guest photochemistry and dissociation.

5.2 Experimental

The HCl and HBr gases were commercial products (Aldrich, purity $> 99.8\%$), and HI was produced in a standard way by reduction of the halogen by red phosphorus and water. The corresponding deuterated halides could be generated by substituting D_2O for regular water. After extensive passivation of the gas system, mixtures of the matrix gas, neon (Messer-Griesheim, purity $>$ 99.999%) in most experiments, with the hydrogen halides were prepared by standard volumetric techniques. The concentrations of the hydrogen halides relative to the matrix gas were in the range of 1:1000-1:20000, and in some experiments comparable quantities of a second rare gas - Xe, Kr or Ar were also added in order togenerate and investigate the $XH\cdots Rg$ complexes.

The samples were deposited on a copper mirror substrate cooled by a Leybold RGD 580 closed cycle refrigerator. While this is nominally capable to attain 6 K, currently its base temperature is only about 8 K. The premixed gas were expanded via a pulsed valve through a 1mm orifice, using a backing pressure of about 2 bar, and condensed on the 8 K substrate. The samples could then be photolysed by means of an excimer ArF laser, operating at 10 Hz and delivering $\approx$20 mJ/pulse at 193 nm. Following photolysis, the samples could be annealed by carefully raising the substrate temperature to 10-12 K, but attempts to increase the temperature much beyond 12 K usually resulted in an irreversible loss of the matrix.

The samples were investigated spectroscopically using a Bruker IFS 120 HR Fourier transform spectrometer, equipped with beamsplitters and detectors for the 500-30000 cm^{-1} spectral range. An argon ion laser, as well as a Ti:Sapphire laser were available to excite sample fluorescence. In most experiments, first background infrared spectrum was recorded using the MCT (mercury-cadmium telluride) detector in the spectral range of 500-4000 cm^{-1}. Subsequently the spectra were recorded after sample deposition, after different periods of 193 nm photolysis, and finally again after careful annealing of the sample by raising its temperature to a desired temperature, typically 10-12 K, for times ranging from 5-20 min.

5.3 Results and Discussion

5.3.1 Rotating Molecules in the Matrix and the Effect of Rotation upon their Spectrum

While the weakly bound rare gas matrix hinders and stops the rotation of most larger molecules, some small species can even in the solid rotate relatively freely, and their spectraexhibit gas-phase like rotational structure. A very clear picture of diatomic rotation in solid rare gases emerged from high resolution investigation of the vibrational infrared emission of CN [149, 167]. While in the gas phase the Q branch transitions are forbidden, due to the barrier to free rotation they may become weakly allowed in the matrix, and one then observes a sharp Q(0) line. As the temperature is raised, a broadened P(1) line and other transitions involving excited rotational levels may become observable. The Q(0) lines connecting the long lived J=0 levels are, when observed, very sharp - in the case of CN their width is $<$0.03 cm^{-1}. Rotationally excited levels with $J>0$ are, on the other hand, immersed in the continuum of quasi-resonant lattice phonon states which leads to a rapid relaxation and a lifetime broadening of all transitions other than the Q(0) line, resulting in widths of typically many cm^{-1}.

Presence of other molecules in the neighbourhood of the guest strongly increases the anisotropic potential, and invariably results in arresting its free rotation [168]. The rotational structure and the usually rather broad rotational transitions are replaced by sharp “Zero Phonon Lines”, effectively the Q-branches of nonrotating molecules. This was demonstrated in the case of CN, where, for instance, addition of $<$1% of xenon or krypton to the argon matrix gas resulted in a complete disappearance of its rotational structure [169]. Understanding of these effects, that is appearance of sharp, forbidden Q(0) lines, the fact that transitions involving excited rotational levels are strongly broadened, and collapsing of the rotational structure into a sharp zero phonon line for nonrotating species will be of great assistance in interpreting the hydrogen halide spectra in solid neon.

5.3.2 Hydrogen Halide Oligomers, and Rotation of the Monomer in Solid Neon

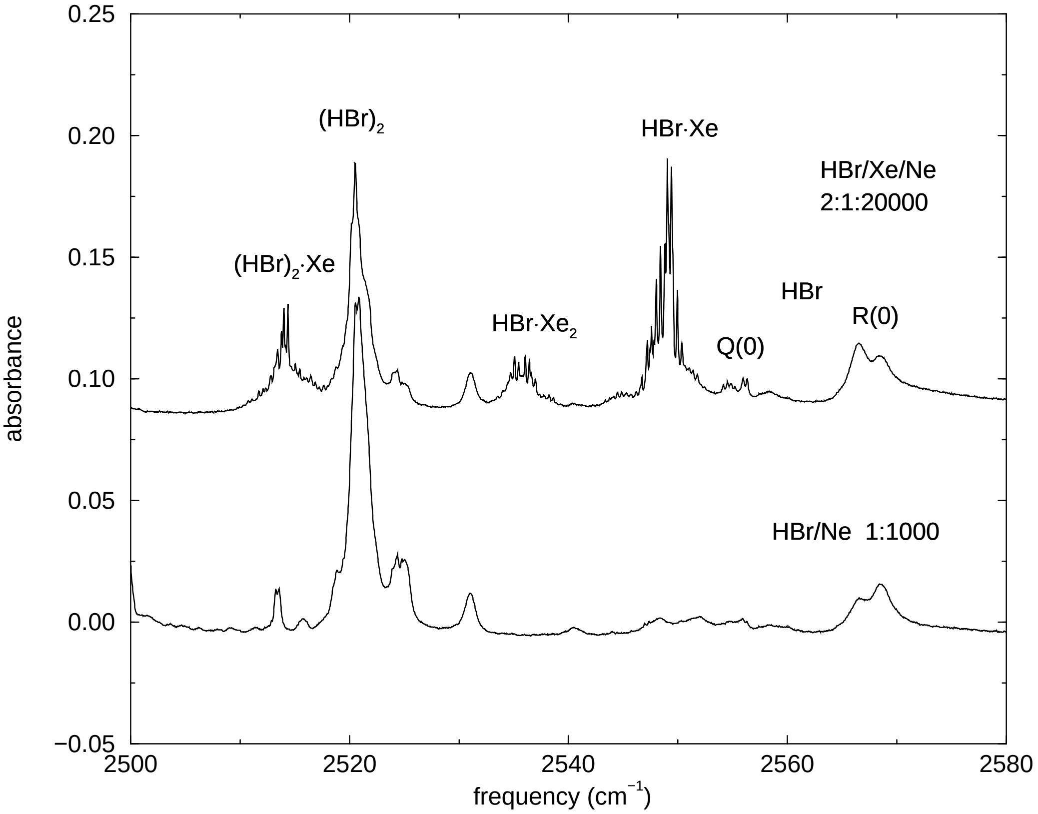

Figure 5.1: Typical IR absorption spectra of neon matrices containing different amounts of HBr and xenon. The lower trace shows pure HBr at the usual concentration of 1:1000. One can see there the broad R(0) and the much weaker Q(0) bands of the monomer, as well as the much stronger dimer absorption. The upper trace shows a more dilute matrix that additionally contains some xenon (HBr:Xe:Ne = 2:1:20000), with the well featured absorptions at 2515 and 2550 cm^{-1} being due to complexes with xenon.

A typical absorption spectrum of a dilute, 1:10^4 hydrogen bromide in neon matrix produced by the pulsed deposition is shown in Fig. 5.1. Hydrogen halides hydrogen bond readily, and even at the 10^4 fold excess of the neon gas absorptions due to the complexes and polymers dominate the spectrum, and their intensities exceed often considerably those of the monomer. The situation actually appears worse than it really is since, as we will discuss later, the complexation in general substantially increases the oscillator strength of the infrared absorptions, sometimes by orders of magnitude, so that the degree of clustering and complexation is much less than one might suspect by superficial examination of the spectrum.

The strongest features in the infrared spectra of cold monomeric hydrogen halides should be the fully allowed R(0) lines. In the case of hydrogen bromide, there appear in this region two broad, incompletely resolved lines at 2566.6 and 2568.6 cm^{-1}, undoubtedly due to monomer in two different sites. In the region of the deuterium stretching vibration there are actually three features: a broad band at 1842.3 cm^{-1}, and two sharper lines at 1839.81 and 1840.36 cm^{-1}. We assign the former to the R(0) line of DBr in one site, while the other two are clearly due to the isotopic D^{79}Br and D^{81}Br lines in a different site. We will return to this question later when presenting the HCl spectrum.

As noted above, even at the lowest concentrations used in our work the strongest infrared bands are due to the $(HBr)_n$ polymers, and the spectra are further complicated by multiple trapping sites. As well known, and confirmed by DFT calculations to be briefly discussed below, the dimers have a bent structure, with the "free" BrH unit oriented at about 92° to the linear BrH$\cdots$Br entity. The hydrogen bonding results in a substantial red shift of the vibrational frequency and an increase of its intensity, with the strongest absorption due to the hydrogen bonded HBr unit appearing around 2520 cm^{-1}. For the prominent major site absorption at 2520.51 cm^{-1} the two bromine isotopic species are not clearly resolved, but in the deuterated molecules one fully resolves the ^{79}BrDBrD and ^{81}BrDBrD bands at 1811.23 and 1810.71 cm^{-1}, respectively. The effects of the isotopic structure of the "free" BrH subunit upon the frequency of the hydrogen bonded HBr are apparently small, and are not resolved. The observed $\approx$36 cm^{-1} shift in the dimer frequency from that of the monomer indicates that the shifts are overestimated considerably by our density functional computations which predict a value of 77 cm^{-1}. Higher polymer absorptions are shifted still further towards the red, with the strongest trimer band appearing at 2487.56 for $(HBr)_3$, and 1783.46 and 1783.80 cm^{-1} for the two deuterium bromide isotopomers.

Species	$r_{Y-H\cdots}$ [Å]	$r_{H\cdots Y}$ [Å]	$r_{\cdots Y-H}$ [Å]	$\delta_{H\cdots Y-H}$ [deg]	$\nu_{\cdots Y-H}$ [cm^{-1}] (Intensity [km/mol])	$\nu_{Y-H\cdots}$ [cm^{-1}] (Intensity [km/mol])	$\nu_{Y-H\cdots}$ [cm^{-1}] exp. value in neon
ClH$\cdots$ClH	1.296	2.546	1.291	94	2874 (46)	2802 (297)	2840.3
BrH$\cdots$BrH	1.427	2.748	1.423	92	2602 (5)	2533 (233)	2520.5
ClH$\cdots$BrH	1.297	2.663	1.423	92	2601 (19)	2786 (362)	2826.6
BrH$\cdots$ClH	1.427	2.641	1.291	94	2876 (45)	2548 (177)	

Table 5.1: *Ab-initio* structure and IR spectra of hydrogen halide dimers at the B3LYP/6-311++G(3df,3pd)/SECP level.

The results of our calculations on the hydrogen halide dimers, as well as the experimental frequencies, are summarized in Table 5.1.

Returning to the monomer, an *a priori* observation and assignment of the forbidden Q(0) lines is made more difficult not only by their weakness, but also due to the fact that in the same region absorptions due to the terminal HBr units (with the free hydrogen) of the $(HBr)_n$ oligomers are expected. Also a method usually used to determine frequencies belonging to the same species in the matrix, that is the correlation (or lack of it) between their intensities, would fail in the present case. The Q(0) lines are forbidden, and their intensities are extremely sensitive to the local environment and its symmetry, and their relative intensities may change substantially with sample concentration, deposition conditions, annealing and photolysis history, etc. Fortunately, in spite of these difficulties, with the help of photolysis and annealing experiments to be described later, one can confidently identify the Q(0) lines. Both the monomer and the $(HBr)_n$ species can be almost completely destroyed by prolonged photolysis of dilute neon matrices, as shown

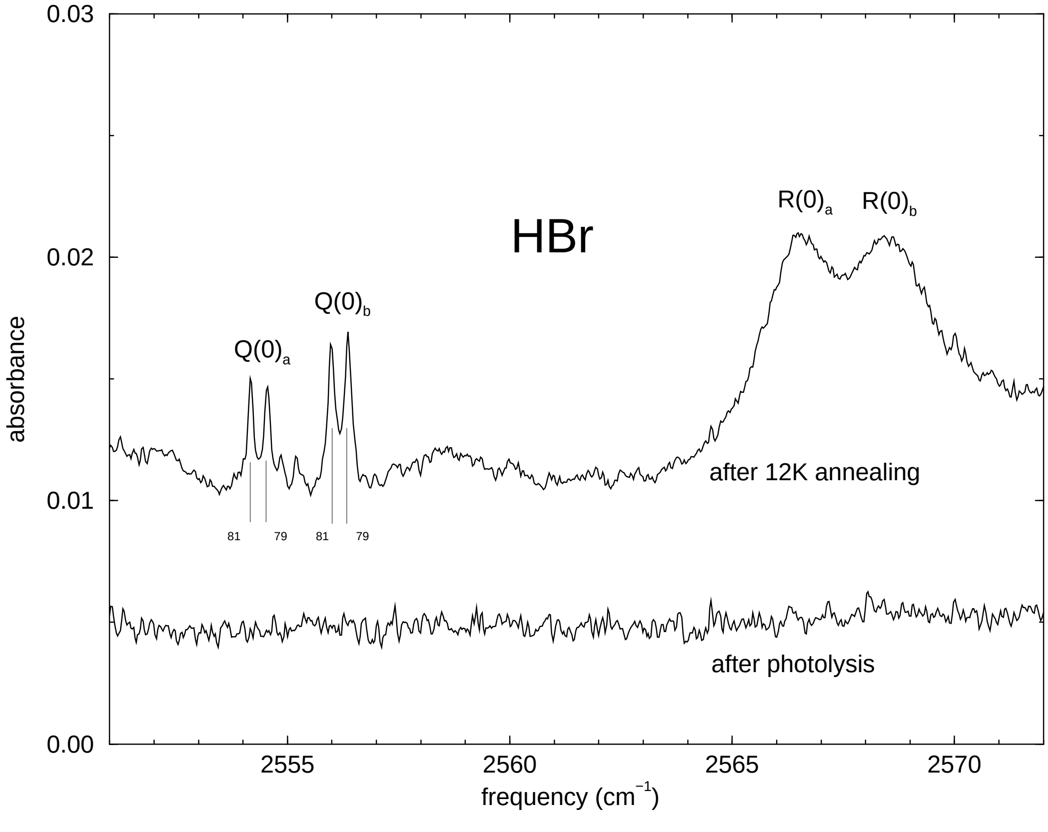

Figure 5.2: Detail of the HBr monomer absorptions in solid neon. The lower trace shows that extensive photolysis (193 nm, 20000 shots at 20 mJ) dissociates all HBr monomers. But after annealing at 12 K for 5 min, as one can see in the upper trace, the life-time broadened R(0) transition and the weak, forbidden Q(0) band of the rotating monomer in two sites, labelled a and b, reappear. Due to the extreme sharpness of the Q(0) transition, the isotopical splitting of the bromine is well resolved.

by the middle trace of Fig. 5.7. Upon subsequent annealing of the sample and diffusion, the monomer can be partially reformed and recovered, but in dilute samples the destruction of the $(HY)_n$ aggregates is virtually irreversible. The annealing also contributes to further reducing the inhomogeneous site broadening. As shown in the top trace in Fig. 5.2, simultaneously with the broad lines assigned above to the R(0) transitions of the monomer HBr in two different sites, also two pairs of sharp lines at 2554.14 and 2554.53, as well as 2555.95 and 2556.34 cm^{-1} grow in. These can be confidently attributed to the Q(0) transitions ^{81}BrH and ^{79}BrH in the two sites, and comparison with the gas phase reveals that the HBr vibrational frequency is red shifted by some 8.2 cm^{-1} in solid neon. If one takes the maximum of the broad bands as the position of the R(0) lines, then the Q(0)-R(0) splitting is reduced in the matrix from the gas phase value 16.9 to $\approx$12.4 cm^{-1}. The HBr rotational constant in solid neon is thus only $\approx$74% of its gas phase value, and the HBr rotation must involve a considerable motion of the neon cage atoms.

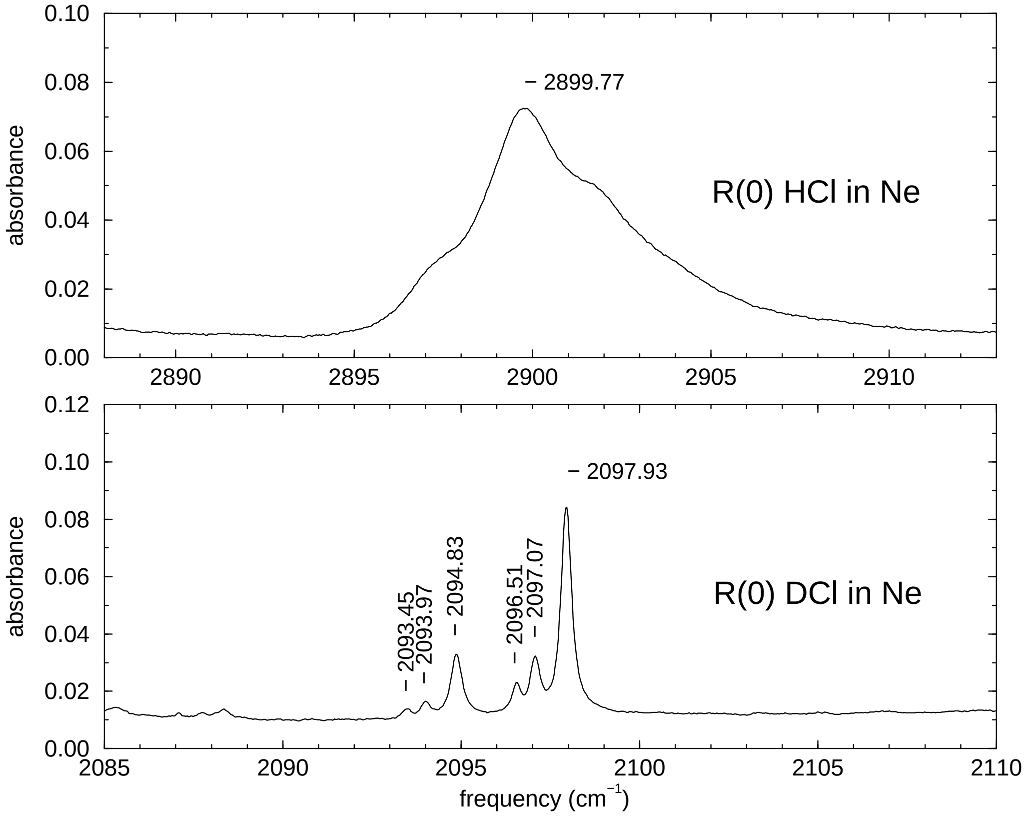

Figure 5.3: The R(0) transitions of both HCl and DCl in solid neon (1:10000). While the HCl band is strongly life-time broadened, the corresponding DCl transition shows two groups of three lines each. The triplet structure is attributed to three different sites, whereas the splitting in two groups is caused by the chlorine isotopic species ^{35}Cl and ^{37}Cl.

In the case of HCl, shown in Fig. 5.3, one finds close to the expected position of the gas phase R(0) lines a rather strong, structured and broad band at 2899.8 cm^{-1}. When the corresponding region of DCl is explored, an interesting isotopic effect is observed. Instead of a similarly broad band, here two well resolved groups of three lines each appear. The relative intensities of about 3:1 of the two groups and the appropriate shift of 3.1 cm^{-1} clearly indicate that they are to be attributed to the chlorine isotopic species ^{35}Cl and ^{37}Cl in natural abundance. The presence of three lines for each isotope is probably due to the presence of three distinct sites. This strong isotopic linewidth effect is again undoubtedly due to lifetime broadening, with about an order of magnitude faster relaxation of the J=1 level of HCl. This apparently couples more strongly to the lattice phonons due to its energy being closer to the maximum of the phonon density distribution of the neon matrix. As explained above, a similar effect was also observed for one of the sites of DBr: while the R(0) lines of HBr in two different sites were quite broad, in the DBr region only one broad R(0) line near 1842.3 cm^{-1} was found. In the place where the other one would be expected, a sharp isotopic doublet at 1839.81 and 1840.36 cm^{-1} appeared. This indicates that the rotational relaxation rates are not only a function of the nature of the matrix, but can also be strongly affected by the specific site geometry and properties: if the interpretation of the linewidths in terms of lifetime broadening is correct, the DBr J=1 rotational relaxation in one of the sites is slowerby more than an order of magnitude than that of the other site.

5.3.3 The Effect of Site Symmetry, and Hydrogen-Halide-Rare Gas Complexes

When dealing with matrix isolation experiments, one of the first experiences is the observation of several so-called “sites” for one transition. These sites are the result of different local environments of the individual guest molecules leading to slightly changed frequencies for one and the same transition. Generally, the larger the guest molecule is, the more different possibilities exist to embed it into the host matrix. Also the crystal structure of the host influences the site distribution. One can thus observe in the case of neon matrices, in general, two major sites resulting from the different *fcc* or *hcp* local environments.

To probe in more detail the effect of local environment, we have studied neon matrices containing small amounts of another rare gas, Ar, Kr, or Xe. In the top trace of Fig. 5.1 we have shown for comparison the H-Br stretching section of the spectrum of a sample with a small addition of xenon (HBr : Xe : Neon = 2 : 1 : 20 000). The presence of xenon had, in spite of its very minute concentration, a profound effect upon the infrared spectrum, with a whole series of new strong absorptions appearing. The most prominent new group between about 2547 and 2552 cm^{-1} consists of several pairs of bands, separated always by 0.39 cm^{-1}. These are clearly due to the isotopic ^{79}BrH$\cdots$Xe and ^{81}BrH$\cdots$Xe complexes in different local environments with the most prominent “site” having frequencies 2549.40 and 2549.01 cm^{-1}. Upon deuteration the major site absorptions shift to 1831.46 and 1830.91 cm^{-1}, again exhibiting the appropriate, 0.56 cm^{-1} splitting expected for the two DBr isotopic species.

Noteworthy is the observation, that in spite of the minute concentration of xenon used, the overall intensity of the new bands exceeds considerably those of the HBr monomer. This is at least partially due to the fact, that the formation of hydrogen bond to the rare gas atom besides shifting the frequency also increases considerably its intensity. Our computations again overestimate the shift caused by the BrH$\cdots$Xe complex formation, with the ab initio 9.24 cm^{-1} value exceeding considerably the observed $\approx$7 cm^{-1} shift, and they also predict an increase of its intensity by about a factor of four. Most conspicuous fact about the new bands is that unlike the broadened R(0) bands of the unbound monomer, the xenon complex absorptions are quite sharp, with widths of about 0.06 cm^{-1}. This is again, as discussed above, due to the fact that in this case one views the lowest level of a nonrotating molecule. The strong R(0) bands of the HBr (or in general HX) free rotor, involve the excited J=1 levels, which are lifetime broadened due to interactions with the lattice phonons.

In addition to the strong bands due to the BrH$\cdots$Xe complex, in the presence of xenon there appear similar groups of additional bands near the absorptions assigned to the polymeric $(HBr)_n$ species, which are clearly due to complexes of these polymers with xenon atoms, that is to species of the type BrH$\cdots$BrH$\cdots$Xe or BrH$\cdots$BrH$\cdots$BrH$\cdots$Xe. These have, compared to the uncomplexed bands lower relative intensities than those of the monomer complex. As noted above, the large intensity of the BrH$\cdots$Xe complex absorptions relative to the free HBr is due to the large enhancement caused by the complexation. Since the intensities of the uncomplexed dimer and trimer bands are already enhanced by the hydrogen bond formation, the additional effect of the xenon complexation is smaller. Thus for instance bands between 2511-2518 cm^{-1}, red shifted from the 2520.51 cm^{-1} free dimer band are attributed to BrH$\cdots$BrH$\cdots$Xe complexes, with the corresponding deuteride bands appearing between 1804-1807 cm^{-1}. Again multiple sites are observed, with the most prominent one being at 2514.35 and 2513.98 cm^{-1} for the ^{79}Br and ^{81}Br species, respectively, and shifting to 1807.01 and 1806.47 cm^{-1} in the deuterated samples.

The situation described for HBr is parallelled by the behaviour of other hydrogenhalides examined, HCl and HI. In each case addition of small amount of xenon results in the appearance of strong new bands due to the hydrogen bonded YH$\cdots$Xe complexes, as well as corresponding complexes involving the YH oligomers. Also here the situation was complicated by the presence of numerous sites, but in the case of chlorine the appearance of doublets with relative intensities of 3:1 and with the characteristic isotopic splitting due to the ^{35}Cl and ^{37}Cl isotopes facilitated greatly the assignments and data interpretation.

Besides xenon, we have investigated briefly also the addition of small quantities of krypton or argon, whose effect was, as could be expected qualitatively identical. In each case new sharp and intense bands due to the hydrogen bonded YH-Kr complex appear at the expense of the broadened bands due to the freely rotating hydrogen halides. In view of the lower polarizability of the lighter rare gas atoms, the interaction is correspondingly weaker, and the shifts of the complex frequencies from that of the free halide are smaller. The information obtained about the various hydrogen halide - rare gas complexes is summarized in Table 5.2.

5.3.4 Photolysis of Hydrogen Halides in Solid Neon

As mentioned in the introduction, the condensed solvent medium can have a considerable effect upon the photophysics of the guest. We have examined the photolysis of the HY hydrogen halides in solid neon, with hydrogen bromide being most extensively investigated. The 193 nm UV radiation of the ArF laser conveniently overlaps the HBr absorption, and the available photon energy of 6.425 eV is more than adequate to dissociate the molecule with $D_0 \approx$3.758 eV. Even

species	r_e [Å]	r_{VdW} [Å]	ν_{VdW} [cm^{-1}]	ν_δ [cm^{-1}]	ν_e [cm^{-1}] (Int. [km/mol])	$\Delta\nu_e$ [cm^{-1}]	ν_e [cm^{-1}] exp. value
ClH	1.289				2885 (37)	0	2899.8
ClH$\cdots$Kr	1.290	3.167	6.2	90	2876 (79)	9	2877
ClH$\cdots$Xe	1.291	3.222	26	185	2865 (126)	20	2867
ClH$\cdots$Cl	1.291	2.578	65	138	2822 (210)	63	
ClH$\cdots$Br	1.296	2.650	61	184	2792 (321)	93	
ClH$\cdots$I	1.297	2.861	54	178	2776 (421)	109	
BrH	1.461				2610 (12)	0	2566.6/2568.6
BrH$\cdots$Kr	1.422	3.482	11	45	2606 (24)	4	
BrH$\cdots$Xe	1.422	3.495	8.4	129	2600 (42)	10	2549.4
BrH$\cdots$Cl	1.426	2.595	36	72	2550 (61)	60	
BrH$\cdots$Br	1.427	2.705	29	126	2534 (185)	76	2527.9
BrH$\cdots$I	1.429	2.914	35	154	2514 (295)	96	

Table 5.2: Hydrogen bonding of hydrogen halides to rare gas and halogen atoms at the B3LYP/311++G(3df,3pd)/SECP level.

though, as mentioned above, all of the bands between2450-2580 cm^{-1} involve HBr, one finds that their rates of dissociation differ substantially, as shown by the logarithmic plot of intensity against photolysis time in Fig. 5.4. In general one can see that the photolysis rate of the dimers and trimers is considerably higher than that of the free monomer. While a part of the effect could, of course, be attributed to the fact that in the case of an “n–mer”, n HBr units are available to absorb the photon, the observed rate difference is larger than could be explained in this way alone. It should also be noted that while dimers photolyse much faster than monomer, there is little difference between dimers and trimers. Concerning the fact that nonradiative relaxation processes in dimers and polymers in matrix are invariably much more efficient than in the monomers, one might even advance the idea that aggregates should photodissociate less efficiently.

A possible explanation of the efficient aggregate dissociation lies in the orientational effects detected experimentally by Apkarian, and found by dynamical simulations by Gerber et al [170]. The $(HBr)_n$ oligomers obviously do not rotate in the matrix, and the unbound proton of the terminal HBr will presumably be oriented towards the potential minimum, in the direction of the cage exit. This may obviously favour photodissociation, and increase its rate relative to that of the freely rotating monomer. An additional factor may be the possibility of alternative reactive channels available to the aggregates. Thus the energetic H atom formed in the transient dissociation event may overcome the activation barrier and react with one of the other HBr units within the cage, yielding an H_2 molecule and probably molecular halogen. That such reaction must occur at least to some extent is evidenced by the observation that the $(HY)_n$ aggregates are essentially not recovered during the annealing process. While small amounts of the monomer can be regenerated by extensive annealing, the loss of the aggregates is virtually irreversible.

Interesting is the photolysis of samples containing a second rare gas, with added xenon being studied in most detail. Unlike the situation with the $(BrH)_n$ oligomers, the formation of the

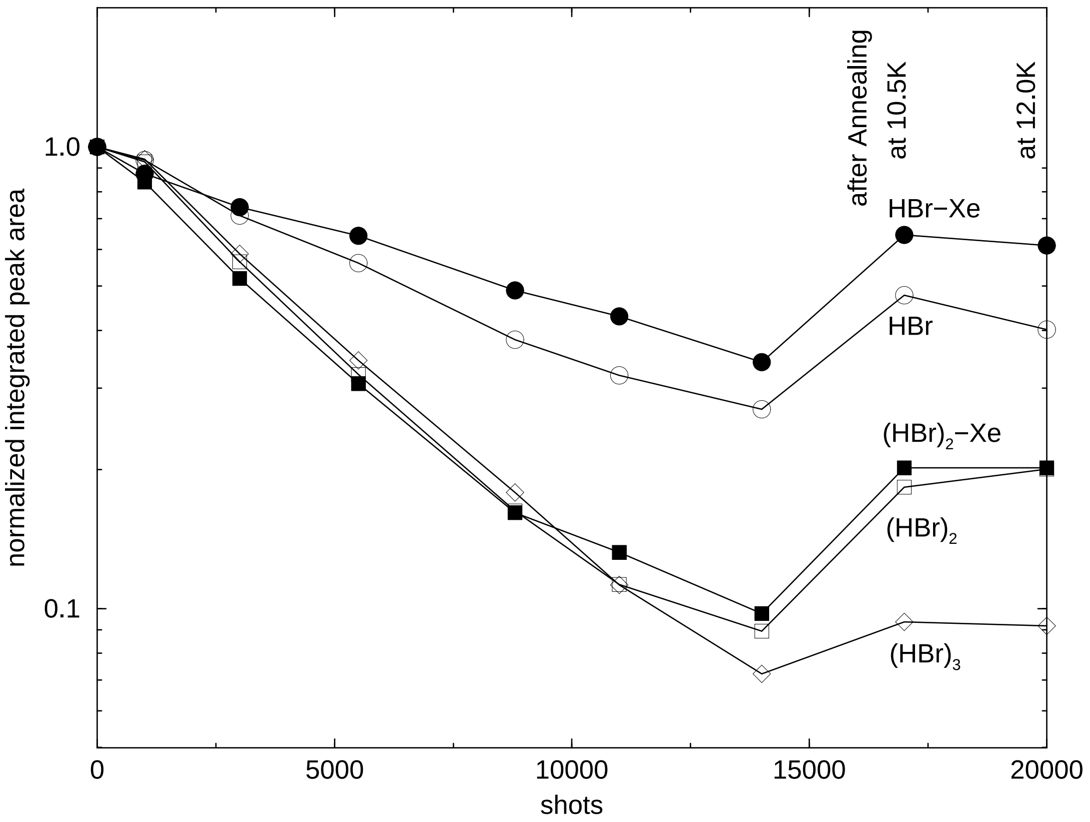

Figure 5.4: Photolysis of different species in a HBr:Xe:Ne (1:1:7000) matrix. This logarithmic plot shows the integrated absorption intensities of several species against the number of 193 nm ArF laser shots (∼10 mJ energy). As one can clearly see, the higher HBr polymers photodissociate faster than the monomer, whereas the formation of Xe complexes decreases the rate of dissociation. After annealing HBr and HBr$\cdots$Xe are almost completely recovered, but the higher (HBr)$_n$ oligomers show only very weak reformation.

BrH$\cdots$Xe complex considerably retards, rather than enhancing the rate of dissociation. In this case, the hydrogen atom is ejected in the direction of the Xe atom, and bounces then between the heavy rare gas and the halogen. After several reflections enough energy is transferred to the lattice to reduce the probability of a cage exit and permanent dissociation.

5.3.5 Photolysis Products, and the Hydrogen Dihalide Species

As previously explained, during the initial phases of irradiation the most efficiently photolysed species are the dimers and trimers, whose absorptions diminish, with a concurrent growth of intense product bands. The most prominent product absorptions in the case of hydrogen bromide appear as a group of sharp bands between 2523-2528 cm^{-1}. This is exemplified by Fig. 5.5, where the top trace shows the strong (HBr)$_2$ band with incompletely resolved Br isotopic structure in the top trace, with the almost complete photolysis of the dimer, and appearance of the slightly blue shifted product absorptions evident in the middle trace. Correlations of the rate of growth of the product bands with the rates of photolysis of the $(HBr)_n$ species in a series of samples with various concentrations indicates quite clearly that these absorptions are the result of a hydrogen atom loss from the $(HBr)_2$ dimer, and should be assigned to the BrHBr, hydrogen dibromide species. It is also easy to understand why the vibrational frequencies are close to those of the dimer: in both BrH· · ·Br and BrH· · ·BrH species, the BrH frequency is red-shifted by interaction with another Br atom, with the presence or absence of the free hydrogen making little difference.

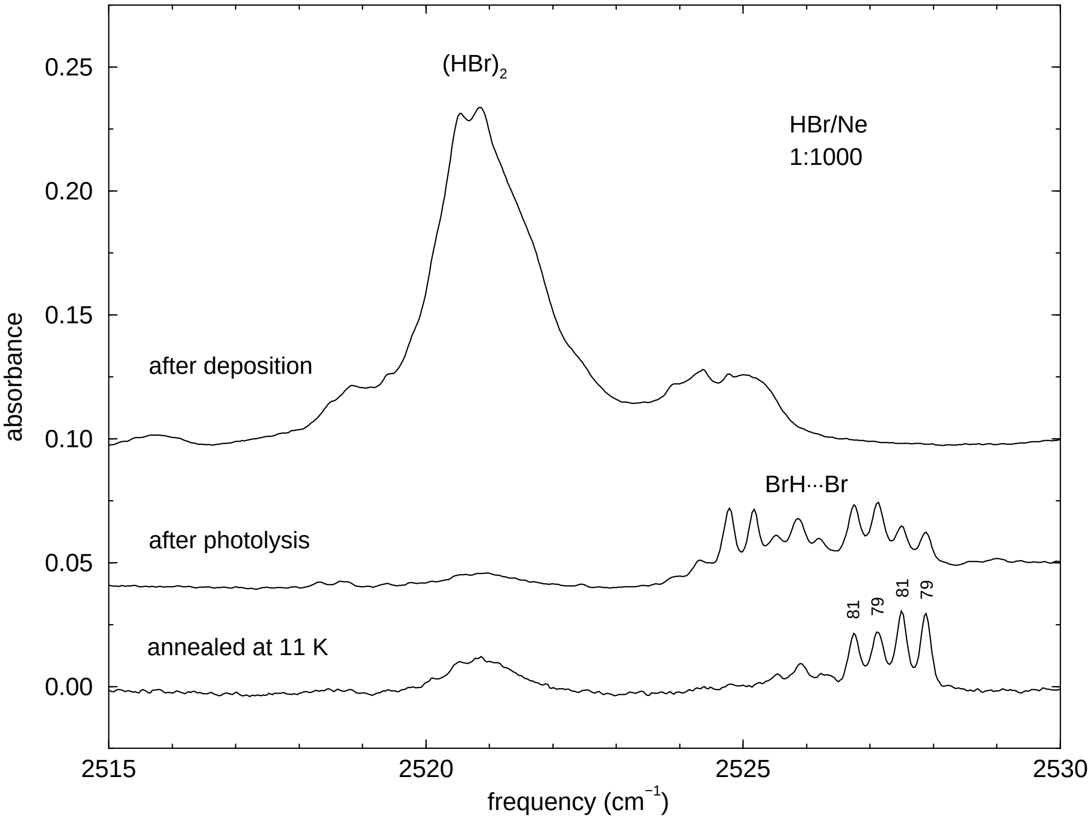

Figure 5.5: The formation of the hydrogen dihalide species in solid neon. From top to bottom: (a) the isotopically incomplete resolved $(HBr)_2$ dimer at 2520 cm^{-1} directly after deposition. (b) the same matrix after 20000 shots 193 nm photolysis, showing the BrH· · ·Br species. (c) After annealing at 11 K for 5 min, the dimer is slightly recovered and BrH· · ·Br (two prominent sites with clear $^{79}Br/^{81}Br$ splitting) gains even higher intensity.

Many years ago, a scheme was proposed for the bonding of hydrogen bihalide anions where the 1s orbital on hydrogen, and the half filled p-orbitals on the two halogen atoms combine to form three center molecular orbitals, one of them bonding, one basically nonbonding, and one antibonding. With four electrons available in the anion the bonding and non-bonding orbitals are filled, forming the well known and rather stable, strongly bound dihalide anions. Extrapolating this model, the removal of one of the non-bonding electrons should not affect the bonding significantly, and the dihalide radicals, HX_2 should have similar properties and similar spectrum to the anions, and an intense search by matrix isolation for these species was initiated in the laboratory of Pimentel. This search indeed resulted in identification of absorptions believed to be due to the HCl_2 and HBr_2 radicals [171]. At that time the possibility of their being due to the anions was considered but dismissed, since they were also produced under circumstances, where from the point of view of understanding of matrix photophysics at that time, ion formation should have been impossible. However, theoretical calculations carried out at the time, suggested that HF_2 should be an asymmetric molecule, essentially an HF perturbed by a second fluorine atom, rather than a linear, centrosymmetric radical [172]. Elegant experiments by Jacox and Milligan have cast increasing doubt on the radical assignment, and shown that the species observed should more likely be matrix isolated bihalide anions [173]. It is now understood that solvation by rare gas atoms can stabilize ionic species in matrices by several eV, and the original objection to the ionic assignment was fallacious.

The HBr_2 species produced here appear again, like the $(HBr)_2$ dimers from which they are formed, in several distinct sites, with the most prominent absorbing at 2527.88 and 2527.50 cm^{-1} for $^{79}BrH\cdots Br$ and $^{81}BrH\cdots Br$, respectively. The $\approx$28.5 cm^{-1} shift of the vibrational frequency from that of the free HBr indicates that the interaction is relatively strong, but it is again considerably smaller than the value of 75.28 cm^{-1} predicted by our DFT computations. Even more than the BrHXe species, the BrHBr complexes photolyze quite inefficiently. By very prolonged irradiation of the matrix they can be destroyed, yielding undoubtedly eventually molecular Br_2 product. Besides HBr, we have also attempted to photolyze HCl in solid neon. While HCl can be photolyzed by prolonged irradiation in solid xenon where its absorption is shifted towards lower energies, in neon its UV absorption occurs further towards the blue, essentially out of the range of the 193 nm ArF radiation. Only in matrices containing Xe, a small degree of photolysis can be detected, perhaps due to the ClHXe complexes absorbing at lower energies. Interesting was the photolysis of HCl samples contaminated by HBr (a contamination which is rather difficult to avoid when both HCl and HBr experiments are to be carried out). In these samples one can by observing the photolysis behaviour readily identify species containing HBr, since hydrogen bromide photolyses very readily. In these samples absorptions due to complexes like $HCl-HBr$ or $(HCl)_2HBr$ are completely photolyzed, while those involving only HCl units remain essentially unchanged. In this way the absorptions due to the mixed aggregates could be assigned with confidence.

5.3.6 Annealing and Diffusion in Neon Matrices

It is well known that while at sufficiently low temperatures most atoms can be stabilized in rare gas matrices, they can be mobilized if the temperature of the matrix is increased. In our cryostat when held at its current base temperature of around 8 K the spectra of both initially deposited and photolyzed neon matrix samples were stable, indicating that appreciable diffusion on the time scale of our experiment does not occur. We could explore the reactions occurring in the photolyzed matrices during a controlled warm up to about 12 K, with attempts to increase the temperature further usually resulting in an irreversible matrix loss. An onset of diffusion and selective mobilization of hydrogen atoms, resulting in changes in the infrared spectrum became in solid neon apparent already above about 9-10 K. The changes could effectively be classified into three categories: changes in the site distribution of existing guests, recovery of photolyzed species, and a growth of new products, and all three effects are documented in Figs. 5.6 and 5.7.

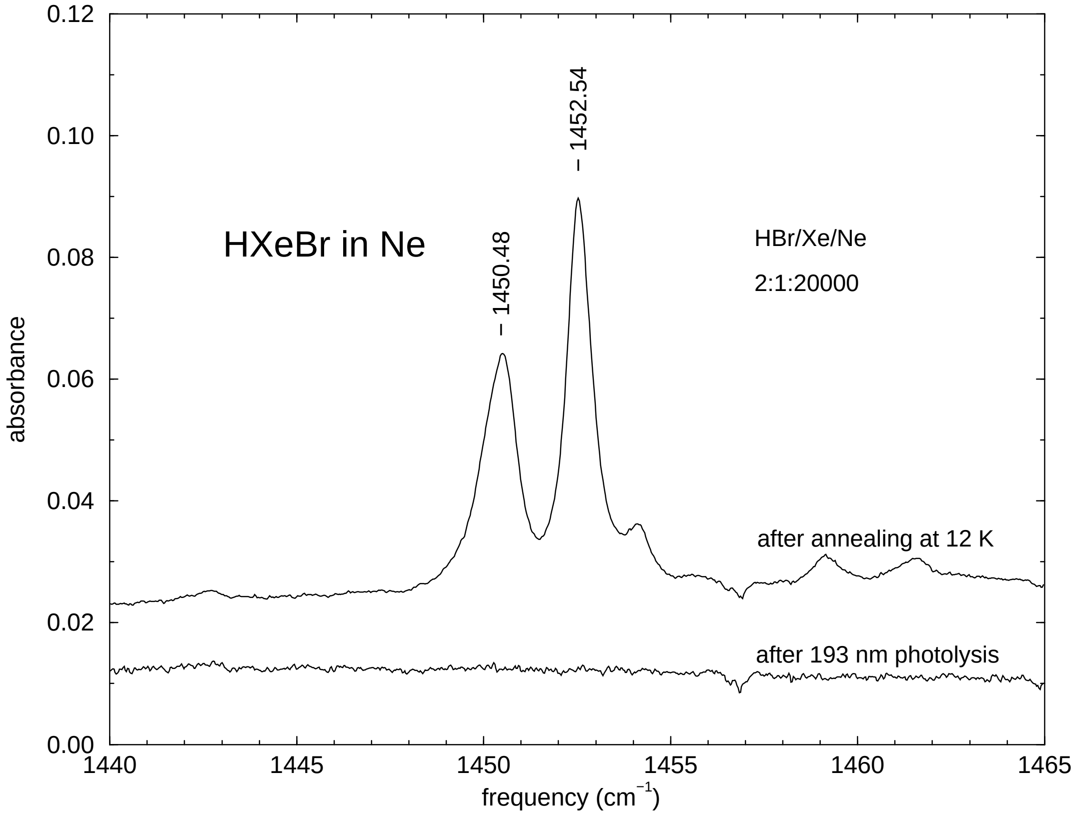

Figure 5.6: The H-Xe stretch vibration of the new HXeBr species in neon. The lower trace shows a HBr and Xe containing Ne matrix (2:1:20000) after 193 nm photolysis. Annealing of this matrix at 12 K leads to the appearance of the new HXeBr molecule, shown in the upper trace, where the most prominent sites are at 1450.5 and 1452.5 wave numbers.

As noted above, initial deposition usually yielded for most species a number of distinct sites, reflecting probably imperfections of the matrix structure, and distribution of different local environments and geometries of the neon atoms solvating the guest. Using annealing the spectra were simplified, with the intensity concentrating into the absorptions of presumably the most stable site, and many absorption bands became sharper. Besides the obvious species which do not appear in the infrared spectrum: halogen molecules, and in particular molecular hydrogen, the most interesting new products accompanying the annealing and diffusion in our matrices were the novel, hydrogen containing rare gas compounds of the type of HRgX or HRgH, which were previously extensively studied in solid xenon and krypton matrices [26, 174]. This is exemplified by Fig. 5.6, showing a section of the spectrum of Ne:Xe:HBr = 20000:1:2, with the region of the H-Br stretching vibrations of the same spectrum shown for comparison in Fig. 5.7. In the initial spectrum in the top trace of Fig. 5.7, strong absorptions due to HBr monomer, bands assigned

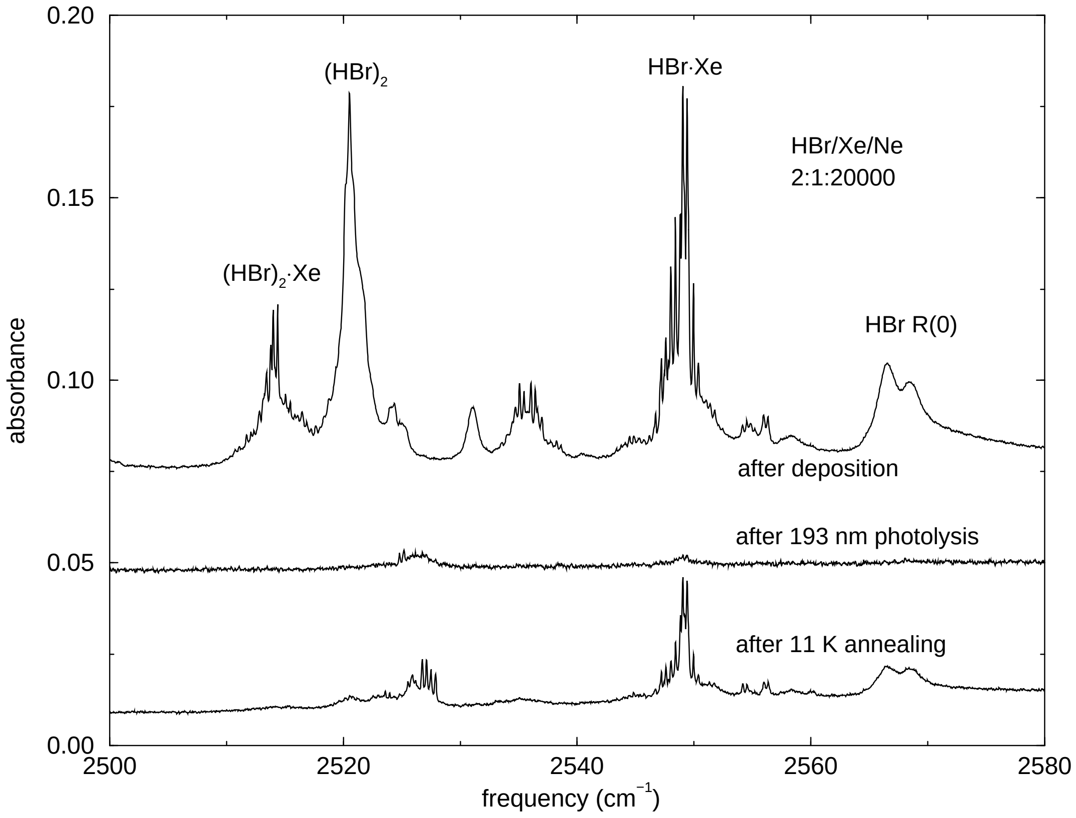

Figure 5.7: Overview spectra of different species in the HBr region: After deposition, after 193 nm photolysis and after 11 K annealing. The complete photodissociation of all species (except BrH· · ·Xe) after prolonged treatment with 30000 shots of an ArF laser is shown in the middle trace. Annealing then allows the recovery of photolyzed species, as well as growth of new products, for example BrH· · ·Br.

to the (HBr)$_n$ oligomer, as well as the sharp BrH· · ·Xe complexes can be seen. After extensive photolysis there is still no absorption in the bottom trace of Fig. 5.6, but almost all the HBr stretching vibrations in Fig. 5.7 (middle trace) disappear, with the exception of a small amount of the BrH· · ·Xe complex, and the photolysis resistant BrH· · ·Br product. Upon annealing of the sample near 11-12 K, hydrogen atom diffusion sets on, accompanied by partial recovery of the HBr monomer absorptions and of the BrH· · ·Xe complexes, as well as a slight growth of the BrH· · ·Br absorptions. One can also note the above mentioned changes in the relative site intensities and distribution. In addition, one can see in the Fig. 5.6 a strong pair of absorptions near 1450.48 and 1452.54 cm^{-1} due to the HXeBr molecule appears [26]. The formation of these species in solid neon is interesting in that it confirms, that the existence of these compounds is not solely due to stabilization by the polarizable xenon and krypton solvents, and this aspect is the subject of the separate chapter 6. Their formation, however, also provides some interesting insight into the diffusion processes in solid matrices.

While the formation of species like HXeBr in solid xenon during annealing of samples resulting from HBr photolysis can be well understood [174], their similarly efficient growth in dilute neon matrices is much more surprising. A hydrogen atom diffusing through a xenon matrix towards a halogen (e.g Br) atom can, regardless of the direction of approach, not avoid passing through the appropriate configuration for HXeBr formation, with a first solvation shell xenon atom between the hydrogen and the bromine. The situation is quite different in solid neon containing only typically 1 part in 20000 of xenon atoms. Even if preexisting XeBr complexes are present, the hydrogen has only about a one chance in 12 to be approaching from the right direction to form HXeBr, rather than interacting with the halogen, and yielding the much more stable BrH$\cdots$Xe complex. To make matters considerably worse, the matrix undoubtedly abounds with many more Br atoms than preexisting BrXe complexes, and one thus might expect a preferential recovery of the hydrogen bromide. In spite of that one notes that recovery of the hydrogen halide monomer is only a relatively minor process, and that the $(HBr)_n$ polymers do not reform almost at all. Against all statistical considerations, the formation of the rare gas hydrogen halide seems to be the most efficient process.

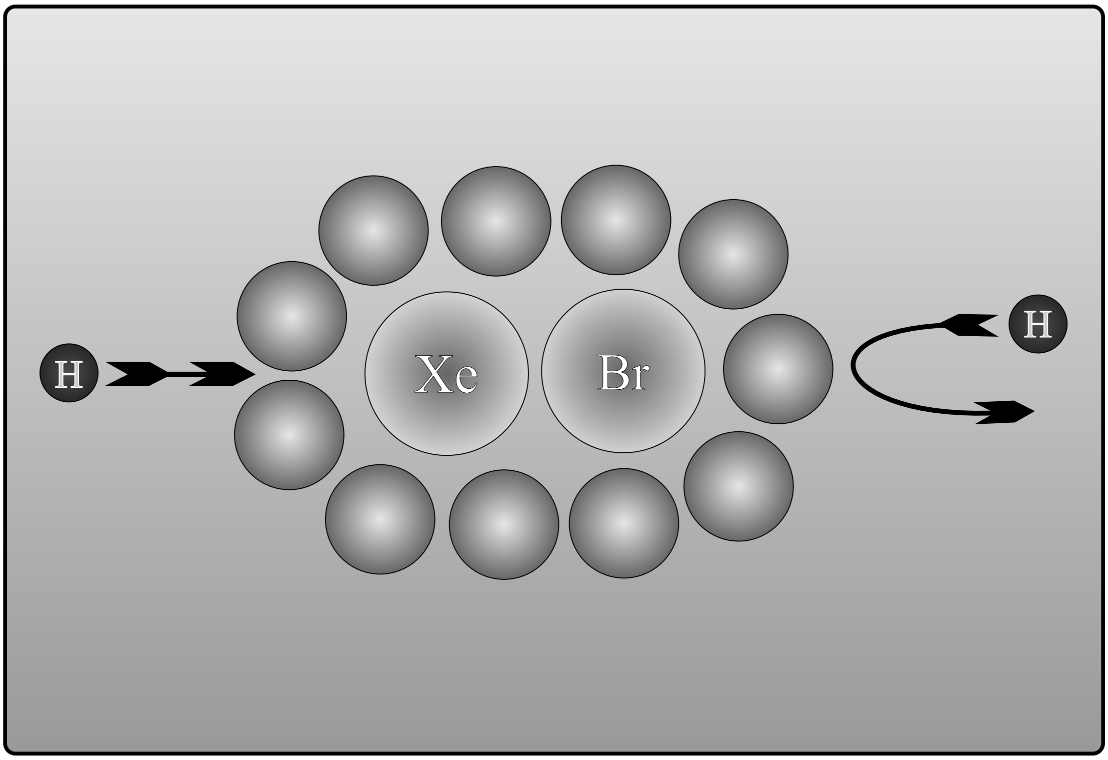

Figure 5.8: Schematic drawing of the formation process of HXeBr in solid neon: A XeBr complex surrounded by neon atoms, which is “attacked” by hydrogen atoms from different directions. Only the hydrogen approaching from the xenon side “tunnels” through the first solvation shell.

It appears like the hydrogen atoms are selectively avoiding the bromine atoms, and when approaching an XeBr complex, prefer to interact with the xenon end. A possible interpretation would be to postulate that each atom in the matrix is protected by a shell of host atoms. In general, the binding potential between e.g. neon host atom and the guest will be deeper than the neon-neon interaction of ca. 30 cm^{-1}. The activation energy for penetrating such a protective solvation shell may then be considerably higher than the barrierfor simple diffusional motion through a pure rare gas (neon) matrix. This idea has an interesting parallel in a series of recent studies by Gordon and coworkers [175, 176]. They found that by evaporating liquid helium into which impurity atoms have been injected, they obtain a solid residue, which remains stable up to temperatures of about 9-10 K when it decomposes explosively, yielding 90-98 % gaseous helium. The interpretation of this experiment is the formation of an impurity stabilized solid, consisting of helium “snowballs” consisting of a heavy atom e.g. nitrogen or xenon, with a relatively tightly held solvation shell. We therefore suggest that similarly also in a solid matrix, each guest atom or molecule in general can be viewed as being surrounded by such a solvation shell (see Fig. 5.8), which can, depending on its stability, retard or enhance its reactions. The fact that against statistical considerations the hydrogen atoms appear to prefer reacting with xenon, rather than with the halogen, would then reflect the fact that the activation energy needed to penetrate the neon solvation shell of a xenon atom is lower than that of the halogen (bromine).

As noted above, and as could be seen in Fig. 5.7, some reformation of HBr does occur, so that the bromine solvation shell is not quite inmpenetrable. We took advantage of the fact that the sharp transitions discussed above and assigned as the Q(0) lines of HBr in two different sites appear in parallel with the broad R(0) lines of monomeric HBr, and in the absence of any $(HBr)_n$ polymer bands, to confirm their assignment. It should be noted, that the $BrH\cdots Xe$ complex is also formed, in parallel with HXeBr, during annealing of the photolyzed samples, although again to a much lesser extent than one would expect statistically. A final product which also reappears on annealing of the completely photolyzed matrices is the $BrH\cdots Br$ complex. Its formation may be due to the reaction of hydrogen atoms with molecular Br_2.

5.4 Theoretical Methods and Computational Results

The calculations were carried out on Silicon Graphics Power Challenge work stations with the help of the Gaussian 94 program package [40]. In most density functional computations the B3LYP hybrid functional was used, although in some cases the results were checked by other methods. For the light atoms H and F all electrons were treated explicitly, using the 311++G(3df,3pd) basis set with two diffuse and four polarization functions on each atom. For the heavier atoms, Cl, Br, or I the quasi-relativistic effective core potential 6s6p1d/4s4p/1d basis sets of the Stuttgart/Dresden group were employed [177].

We have first computed the geometries of the diatomic hydrogen halides, HY, themselves, to check the methods and provide comparison with experiment. We have then examined the effect of formation of hydrogen bonded complexes upon the geometry and vibrational frequency of the hydrogen halides. The results of our computations are listed in Tables 5.1 and 5.2. Remaining with a given YH species, the shift upon formation of an $YH\cdots X$ complex is smallest when X is a rare gas, increasing from Kr to Xe with the rare gas polarizability. Much larger shifts are obtained for the “hydrogen dihalide” species, where X is a halogen atom. Here again the shifts increase with the size and polarizability of the halogen.

5.5 Summary

Hydrogen halides HY nearly freely rotate in solid neon matrix, and their 8 K IR spectra consist of strong, lifetime broadened R(0) lines, and weak and very sharp, matrixinduced Q(0) transitions. The free rotation is stopped in strongly bound oligomers, and complexes with the more polarizable rare gases Kr and Xe, which exhibit sharp zero phonon line spectra, with well resolved Br or Cl isotopic splitting. The spectra of both the monomers, as well as of the oligomers and complexes are somewhat complicated by the presence of multiple sites. The hydrogen bonding results in a red shift of the bound YH$\cdots$X frequency, and a considerable increase in its intensity. The interpretation of the results is facilitated by extensive density functional B3LYP computations.

The hydrogen bonding also has a considerable influence upon the YH photolysis behaviour. The 193 nm excimer laser radiation photolyses much more efficiently the oligomers than the monomers, an effect which is attributed to the molecular rotation. Photolysis of the dimers results in well defined, asymmetric hydrogen dihalide products such as BrH$\cdots$Br. Formation of complexes with rare gas atoms on the other hand retards the photolysis. Annealing of the matrices above $\approx$10 K results in selective mobilization of hydrogen atoms, resulting in partial recovery of the YH monomers, as well as in formation of the HXeY compounds in neon matrix. There is, on the other hand, virtually no reformation of the dimers and trimers. A model explaining the observed annealing behaviour and the formation of the rare gas hydrogen halide compounds is proposed.

Chapter 6

New Raregas Compounds in Solid Neon

The recently discovered halogen xenon hydrides ClXeH and BrXeH, their deuterated analogues, and tentatively also the HXeH dihydrides were generated in solid neon matrices, and characterized by infrared absorption spectroscopy. The preparation of these interesting species in the weakly interacting neon matrix, as well as extensive DFT calculations suggest that their observation is not solely due to stabilization effects by the matrix, but that they should be capable of independent existence as free molecules in the gas phase.

6.1 Introduction

Even though several small ions or metastable species involving rare gases were known for a long time, until fairly recently, its rare gas elements were generally regarded as chemically inert. In 1962 Neil Bartlett has shown in his trailblazing study [178, 179] that they are capable of forming of what one could consider as normal chemical compounds, compelling chemists to readjust considerably their thinking regarding these elements. In a burst of activity in the years that followed, a number of compounds of noble gases have been reported [180, 181, 182, 183, 184]. While many of these can be regarded as metastable species, several are actually thermodynamically stable compounds and can be obtained commercially. For example, xenon difluoride has found a relatively widespread use as a fluorinating agent, and has useful applications in semiconductor processing for etching silicon.

Very shortly after the discovery of the first rare gas compounds, matrix isolation specialists made considerable contributions to the understanding of their chemistry, with for instance xenon dichloride [185], krypton difluoride [186] and mixed xenon chloro-fluoride [187] having been characterized. Infrared spectra of the HAr_2^+ and HKr_2^+ species have also been observed, although initially their structure and ionic nature were in doubt [163], but recent calculations helped to clarify the exact structure [188, 189]. The progress in the following 20-30 years was then relatively slow, with the chemistry of rare gases being effectively restricted to a few compounds of xenon involving the most electronegative elements, fluorine or oxygen. Quite recently, a new breakthrough in this direction occurred in the laboratory of Räsänen, when a whole group of novel neutral rare gas compounds was observed. These included not only several hydridohalogenides of the type HRgX with both a halogen (Cl, Br, or I) and a hydrogen (or deuterium) atom bound to Kr or Xe [26], but also the symmetric dihydrides [190], as well as several compounds with CN, SH and other groups bound directly to the rare gas [191, 192].

While these species were carefully characterized, the question remained as to the ability of the molecules to exist outside the stabilizing environment of the polarizable xenon or krypton host matrix [27]. To address this question, we explore in the present publication the properties and chemistry of these species in solid neon, where any stabilization due to the solvent will be appreciably diminished with respect to the heavier rare gases. We also explore the question of solvent stabilization by extending our earlier theoretical computations with additional rare gas atom interactions with the HRgY species. We believe that the results show clearly that the solvent stabilization is not essential, at least in the case of HXeCl and HXeBr , and that once prepared, the species should be capable of existence as free gas phase molecules.

6.2 Experimental

To produce the samples in our experiments, commercially available HBr and HCl gases (Aldrich, purity > 99.8%) were used. HI was produced in a standard way by reduction of the halogen by red phosphorus and water. The corresponding deuterated halides could be generated by substituting D_2O for regular water. After extensive passivation of the gas system, mixtures of the neon matrix gas (Messer-Griesheim, purity > 99.999%) with xenon (Messer-Griesheim, purity > 99.998%)

and the hydrogen halides were prepared by standard volumetric techniques. The concentrations of the hydrogen halides relative to the matrix gas were in the range of 1:1000-1:20000, while the xenon:hydrogen halide ratio varied from 0.5:1 to 10:1.

The samples were deposited on a copper mirror substrate cooled by a Leybold RGD 580 closed-cycle refrigerator. While it should be nominally capable to attain 6 K, currently its base temperature is only about 8 K. The premixed gas was expanded via a pulsed valve through a 1 mm orifice, using a backing pressure of about 2 bar, and condensed on the 8 K substrate. The samples could then be irradiated by means of an excimer ArF laser, operating at 10 Hz and delivering $\approx$10 mJ/pulse at 193 nm. Following irradiation, the samples could be annealed by carefully raising the substrate temperature to 10-12 K, but attempts to increase the temperature much beyond 12 K usually resulted in an irreversible loss of the matrix.

The samples were investigated spectroscopically using a Bruker IFS 120 HR Fourier transform spectrometer, equipped with beamsplitters and detectors for the 500-30000 cm^{-1} spectral range. In most experiments, a background infrared spectrum was first recorded using a MCT (mercury-cadmium telluride) detector in the spectral range of 500-4000 cm^{-1} with 0.06 cm^{-1} resolution. Subsequently the spectra were recorded after sample deposition, after different periods of 193 nm photolysis, and finally again after careful annealing of the sample by raising its temperature to the desired value, typically 10-12 K, for times ranging from 5-20 min.

6.3 Results and Discussion

In the previous studies, the HRgY species were in most cases prepared by photolysing hydrogen halides HY in matrix of a rare gas Rg, and by subsequent annealing of the samples [26, 190]. Irradiation of the samples results in a permanent dissociation of the HY species, and presumably in the formation of halogen and hydrogen atoms. The presence of halogen atoms is evidenced by the infrared absorption bands due to the $P_{3/2} \rightleftharpoons P_{1/2}$ transition between the ground state spin-orbit components which appear in the irradiated samples near 3600 cm^{-1} in Br and $\approx$7600 cm^{-1} in I [193]. Subsequent controlled annealing of the matrices results then in diffusion of hydrogen, and is accompanied by the growth of strong absorption bands of the products, assigned to the HRgY species. In several investigations of these species it was suggested that they are strongly ionic structures of the type HRg^+Y^- [26, 27]. We have recently investigated proton solvation in rare gases, and shown that the effectively dimensionless proton will always be solvated by two rare gas atoms [156]. This naturally raised the question of wether the stability of the HRgY species could be due to the stabilization by the rare gas solvent, that is, if they could be actually considered to be the four-atom species $(RgHRg\ )^+Y^-$. We use here two approaches to test this question: we examine the solvation of the HRgY species by rare gases and the stability of the $(RgHRg\ )^+Y^-$ four atomic species by density functional calculations, and we try to prepare the HRgY species in solid neon, where, in view of the much lower polarizability and high ionization potential of neon atoms, the stabilizing effect of the rare gas solvent should be negligible.

The infrared spectra of even the most diluted HY+Xe : neon samples measured immediately after deposition contained not only the monomeric HY bands, but also rather strong dimer and trimer absorptions, see Fig. 5.1. This is in part due to formation of the complexes in the supersonic expansion and during deposition on the matrix surface, and may also be contributed to the relatively high, 8 K temperature of the matrix substrate. The spectra are, however, somewhat misleading, since hydrogen bonding greatly enhances the oscillator strength of the YH absorptions, in some cases by more than an order of magnitude [194].

In the presence of xenon, additional strong and sharp bands appear in the spectrum, which can be identified as YH· · ·Xe species, complexes of the hydrogen halide with a xenon atom. The complex formation results in a red shift of the HY infrared absorption, and again in a considerable enhancement of its intensity.

6.3.1 The HXeBr and DXeBr species

From the experimental point of view it was most expedient to study the photolysis of HBr since its absorption overlaps well the 193 nm line of the argon fluoride laser. When exposed to the 193 nm line, the HBr samples are bleached quite effectively, so that after some 60 minutes the absorptions

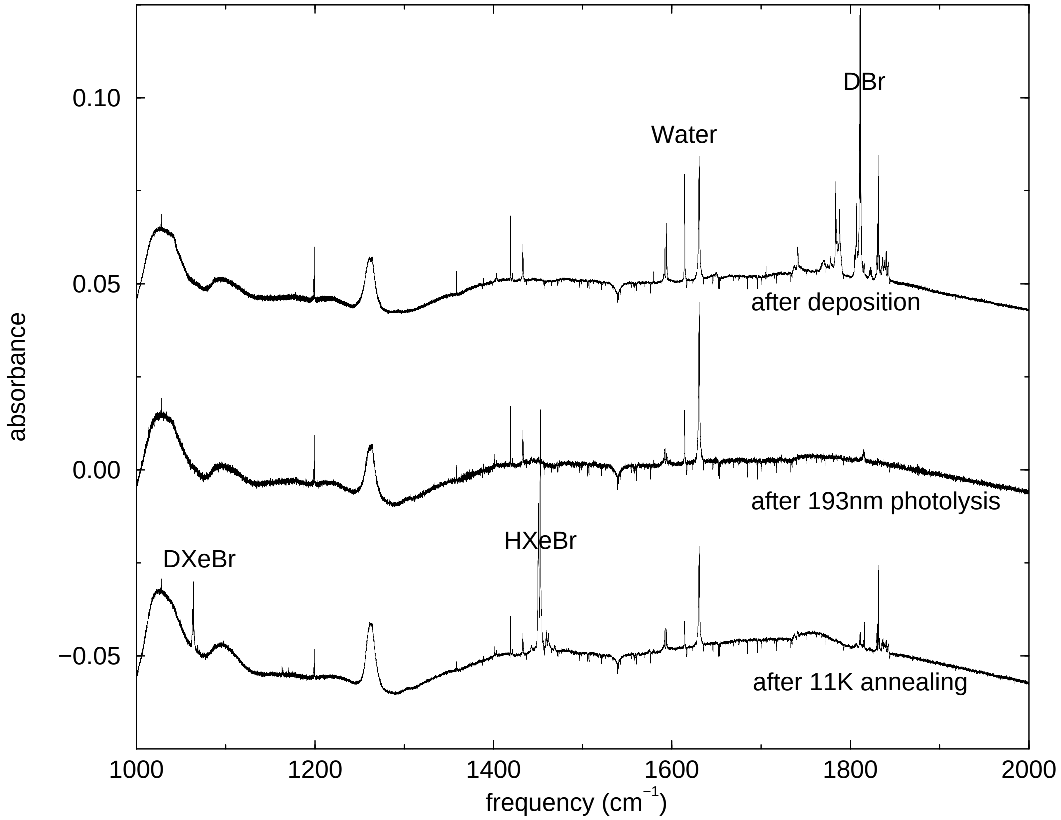

Figure 6.1: A series of spectra of an HBr/DBr:Xe:Ne mixture showing the xenon compound formation process. The DBr (and HBr) bands present in the top trace right after deposition disappear completely after extended 193 nm irradiation (middle trace). Annealing of the sample at 12 K allows H atom diffusion, and leads to appearance of bands of the HXeBr and DXeBr products.

both of the $(HBr)_n$ aggregates, as well as of the monomeric hydrogen bromide disappear almost completely. Although BrH$\cdots$Xe photolyzes less efficiently than the free species, even these complexes are bleached after an extended irradiation. The photochemistry of hydrogen halides in rare gas matrices, as well as the effect of hydrogen bonding, were studied in detail in the previous chapter.

More dilute samples (HBr:Xe:Ne = 1:1:10000) show immediately after UV irradiation little evidence of any new rare gas compound formation. When, however, the samples are carefully annealed to temperatures above $\approx$9.5 K allowing hydrogen atom diffusion, a group of strong, sharp bands appears near 1450 cm^{-1} as shown in the lowest trace of Fig. 6.1. Specifically, new bands grow in at 1436.61, 1442.61, 1450.49 and 1452.57 cm^{-1}, with the latter two being favoured with increasing dilution of the samples. Prolonging the sample annealing, and increase in the annealing temperature results in a gradual disappearance of the lower frequency absorptions, and the intensity shifts in favour of the 1452.57 cm^{-1} band. In more concentrated samples some absorption in this region, and in particular the 1442.61 cm^{-1} band, appears immediately after the sample irradiation, but the intensity again increases drastically upon annealing, with intensity shifting to the higher frequency 1450.49 and 1452.57 cm^{-1} absorptions.

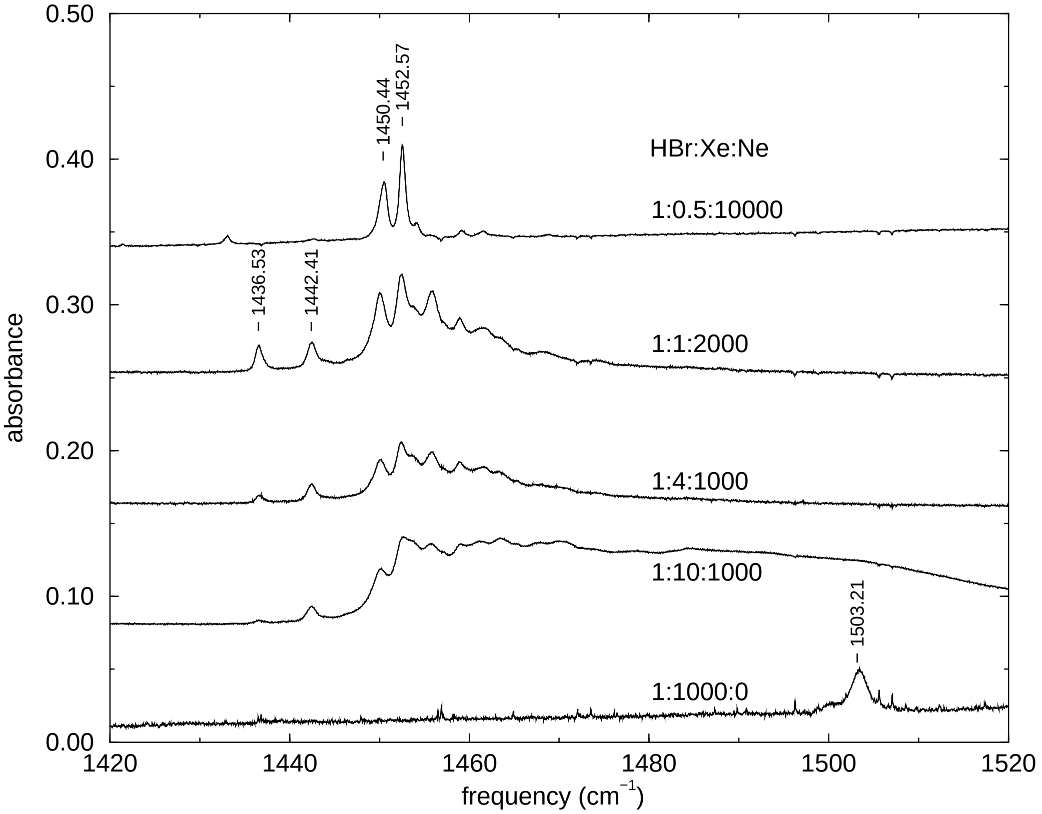

Figure 6.2: The hydrogen stretching vibration of HXeBr in solid neon in samples with different Xe concentrations. As the Xe concentration is increased, the absorptions broaden and shift towards blue. The lowest trace shows the HXeBr band in a pure xenon matrix.

These bands clearly correspond to the H-Xe stretching frequency of the HXeBr molecule. With increasing xenon concentration, additional bands probably due to species involving more than one Xe atom appear at higher energies, and when the concentration of xenon is increased to 1%, the 1452 cm^{-1} absorption is followed by a broad structured absorption extending to beyond 1503.2 cm^{-1}, the position of the corresponding HXeBr absorption in a pure xenon matrix [26]. This dependence on the xenon concentration is shown in Fig. 6.2.

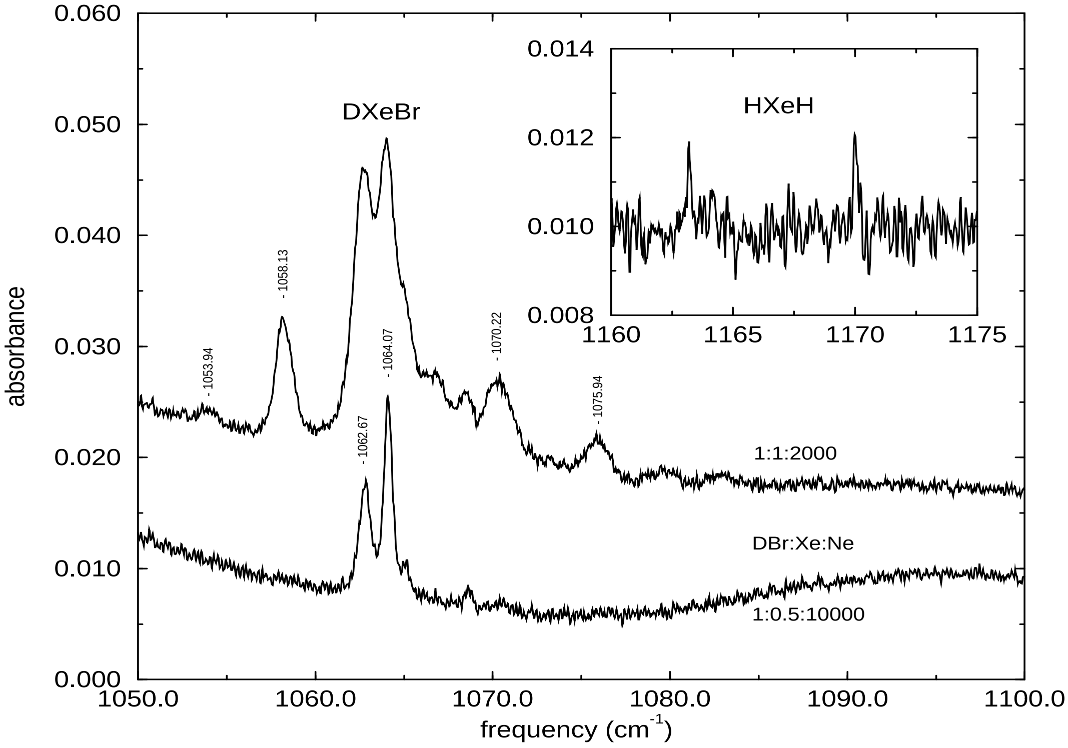

Figure 6.3: The hydrogen stretching vibration of DXeBr in solid neon using two different xenon concentrations. The insert shows the very weak absorptions at 1163.19 and 1169.98 cm^{-1} of a highly diluted HBr:Xe:Ne = 1:0.5:10000 matrix after photolysis and annealing at 12 K. These absorptions are assigned tentatively to the asymmetric stretch of HXeH (two sites).

The HXeBr bands shift appropriately in deuterated samples, as one can see in Fig. 6.3. A nearly identical pattern of bands appears near 1050 cm^{-1}, with the DXeBr bands at 1053.94, 1058.13, 1062.67 and 1064.07 cm^{-1} mirroring the four major sharp bands in the HXeBr region. Increasing sample dilution, and more thorough sample annealing again favour the highest frequency 1064.07 cm^{-1} band. In neon the frequencies are again considerably red shifted compared with the 1100 cm^{-1} absorption band in a pure xenon matrix. Besides the xenon hydrogen-bromide, in the most dilute experiments the diffusion also produced absorptions bands at 1163.19 and 1169.98 cm^{-1} (see insert of Fig. 6.3), very close to bands assigned in solid xenon to the xenon dihydride. Accordingly, we assign these neon matrix bands somewhat tentatively also to the HXeH species.

Irradiation of the samples using a tungsten lamp was found to photolyze very efficiently the HXeBr species. This confirmed their relatively labile nature, but also prevented meaningful measurements of their visible and near IR absorption spectra. After these species were decomposed and their absorptions bleached, only a very minor amount could be regenerated by additional annealing and diffusion. This suggests that the reaction involved is probably not dissociation to H + XeBr (or HXe + Br) but more likely to bromine-hydrogen recombination and presumably conversion to the BrH$\cdots$Xe "isomer". Similar photo-instability has also been observed in pure xenon matrices [26].

It is interesting to note that around 9 K temperature, where we observe the onset of a long-range hydrogen diffusion in solid neon and formation of the HXeY molecules, changes in the matrix Raman spectrum were previously observed, and interpreted in terms of a partial hcp-fcc phase transition [53]. If this is accepted, it is conceivable that the onset of global hydrogen mobility is connected with such a phase transition.

6.3.2 The HXeCl and DXeCl species

Hydrogen chloride absorptions occurs at considerably higher energies than those of hydrogen bromide, and are therefore not efficiently excited by the 193 nm laser. Only after a very prolonged irradiation there is a minor photolysis of the HCl monomer, with basically no change in the sharp, spectrally shifted absorptions of the ClH$\cdots$Xe complexes. Annealing of such irradiated samples leads to growth of absorptions due to the HXeCl species, as one can see in Fig. 6.4. These, like the corresponding bromine compound, exhibit in solid neon several distinct trapping sites, all of them again considerably red shifted compared with their positions in pure xenon. In samples thoroughly annealed to 11-12 K, the HXeCl absorptions concentrate into a quintet at 1607.03, 1608.25, 1609.88, $\underline{1611.80}$ and 1614.22 cm^{-1}, with the underlined fourth component being the strongest. Using a deuterated sample, the corresponding DXeCl absorptions appear at 1167.40, 1168.75, 1170.33, $\underline{1172.14}$ and 1172.96 cm^{-1}.

When an HBr impurity was added to the HCl/Ne sample, this of course could be photolyzed very efficiently, as did the mixed HBr$\cdots$HCl complexes, and annealing of such irradiated mixed samples leads also to an enhanced formation of the HXeCl species. This may be due to the reaction $HCl+H \rightarrow H_2+Cl$, followed by reactions of the Cl atom with Xe and eventually with another hydrogen atom. Interestingly, even though the 193 nm laser line overlaps ideally the HI absorption, and indeed HI is easily photolyzed in solid neon, we had no success trying to generate the corresponding HXeI compound by annealing of the photolyzed matrices. This may either be due to an intrinsic instability of the iodine compound which needs the stabilizing environment of solid xenon, or perhaps to the dynamics of the matrix diffusion and reaction, which do not favour the compound formation in solid neon. In this connection it is appropriate to note, that theoretical calculations also predict the HXeI molecules to be bound considerably weaker than the corresponding bromide or chloride [27]. The lower stability of the HXeI species is also evidenced by the observation that in solid xenon it can be readily photolyzed by infrared excitation near 3000 cm^{-1}, caused by the low dissociation energy D_0 = 2950 cm^{-1} [174].

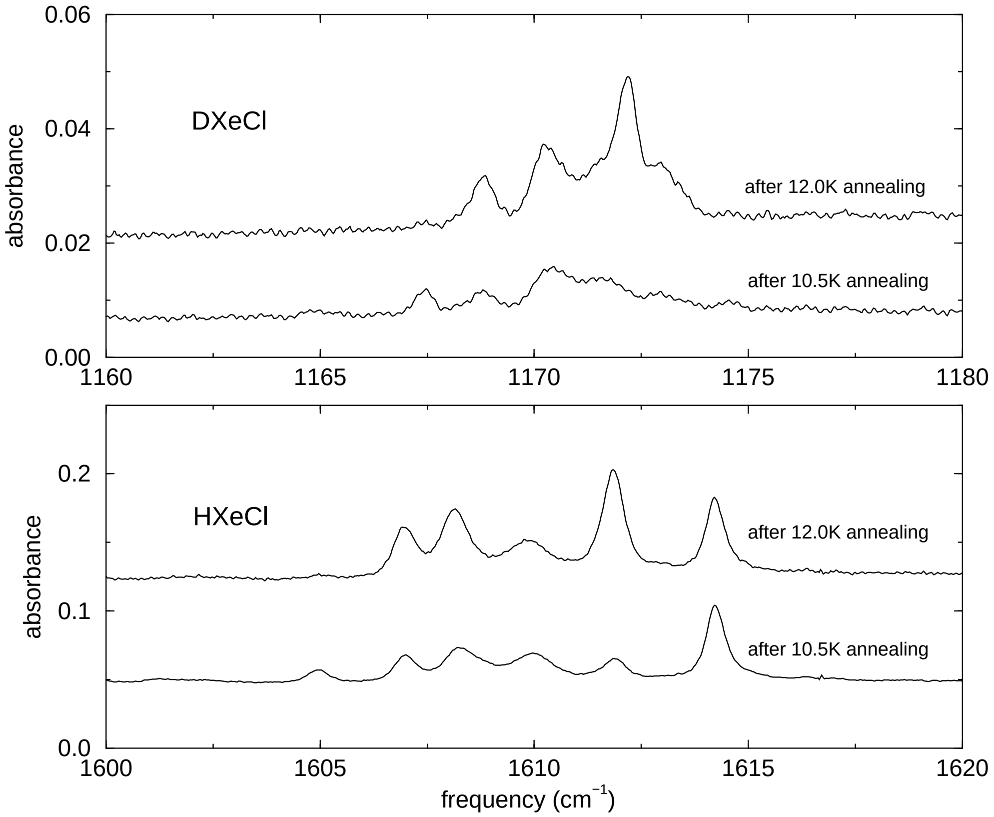

Figure 6.4: The effect of annealing upon site distribution. Spectra show the hydrogen stretching vibrations of HXeCl and DXeCl in a sample of H(D)Br:Xe:Ne = 1:0.5:10000.

6.3.3 The formation of HRgY in rare gas solids

If one considers more closely the problem of the mechanism of their formation, it is, in fact, remarkable that the HRgY compounds form in solid neon with an efficiency comparable to that in solid xenon. They are undoubtedly formed when lighter and more mobile hydrogen atoms diffuse through the matrix and eventually approach an RgY, e.g. XeBr complex. The substitutional Br atom will presumably have twelve nearest neighbour xenons, and regardless of the direction of approach, when the hydrogen reaches the second solvation shell, there will be a quasi-linear H-Xe-Br configuration appropriate for HXeBr formation [27]. The situation is quite different in solid neon, where even if an XeBr complex is already present, only one of the bromine nearest neighbours is xenon, and the approaching hydrogen would thus appear to have a less than 10% chance of arriving exactly from the right direction. One might thus expect that in more than 90% of events the hydrogen will encounter the halogen, and find the global minimum on the potential surface, that is the BrH$\cdots$Xe complex, rather than the shallow, much less stable HXeBr local minimum.

To explain the experimental observation that this does apparently not occur, that the hydrogen bromide recombination is relatively minor, and that the HXeBr forms efficiently, we have proposed that each matrix isolated atom can be viewed as being surrounded by a protective solvation shell of the matrix atoms. Since the interaction of the guest atom with the rare gas atoms is usually stronger than the interaction between two rare gas atoms themselves, such a shell may be relatively stable, and the activation energy for penetrating it may be considerably higher than that for diffusion through the pure matrix. If the barrier for penetrating such a solvation shell around Cl or Br atoms in neon were too high to overcome at the 10-11 K temperature where the H atom diffusion takes place, this would explain why the hydrogen halide recombination is relatively inefficient. The hydrogen would then preferentially have to attack the Xe-Br complex from the xenon side - supposing such a solvation shell around the xenon atom is easier to penetrate than that around the halogen - explaining the efficient HXeBr formation. Extending this idea, in the case of the large iodine atom the neon solvation shell might be less stable and more penetrable, and this could lead to efficient HI recombination, and provide an alternative explanation for our failure to observe the HXeI species in solid neon.

Species	Xenon (from ref. [26, 190])	Neon after 12 K annealing
HKrCl	1476	- (tried to observe, but failed)
DKrCl	1106	-
HXeF	-	-
HXeCl	1648	1607.03, 1608.25, 1609.88, 1611.80, 1614.22
DXeCl	1198	1167.40, 1168.75, 1170.49, 1172.14, 1172.96
HXeBr	1504	1436.61, 1442.61, 1450.49, 1452.57
DXeBr	1100	1053.94, 1058.13, 1062.67, 1064.07
HXeI	1193	-
DXeI	893	-
HXeH	1166, 1181	1163.19, 1169.98

Table 6.1: ν(H-Rg) [cm^{-1}] for H(D)RgY molecules in solid xenon and neon, with the strongest absorptions underlined.

The vibrational frequencies of the HXeY and DXeY species observed in this work are listed in Table 6.1, and compared with the values previously found in solid xenon. The comparison reveals a rather large matrix effect, with the frequencies being appreciably blue shifted when going from neon to xenon. The guest-host interactions are quite complex, and their magnitude and direction depend on the nature of the trapping site, polarizabilities of both the guest and the host, and a number of other factors. Very large matrix shifts are, in general, indicative of ionic or strongly polar bonds. The bonds in the HXeY molecules indeed have a partial ionic character, and the relatively large blue shifts observed could be rationalized by stabilization of the polar structures by the polarizable xenon solvent.

6.4 Theoretical Calculations

As explained in the introduction, the considerable stability of the linear RgHRg$^+$ ions led to the question of whether the HRgY compounds in the matrix could be viewed as RgHRg$^+$Y$^-$ species, rather than as HRg^+Y^- as previously proposed, and if they owe their stability to the stabilizing effect of the matrix. To explore this idea, we have carried out density functional calculations on these systems using the Gaussian 94 program package [40]. Most of the calculations were carried out by the hybrid B3LYP method, although several results were checked by other methods. On the light atoms (H,F) all electrons were explicitly treated with the 6-311++G(3df,3pd) basis sets. For the heavier halogens, Kr and Xe, the quasi-relativistic effective core potential 6s6p1d/4s4p1d basis sets of the Stuttgart/Dresden groups were used [177].

Species	r(Xe$\cdots$H)	r(H-Xe)	r(Xe-Y)	ν(Xe-Y)	δ(HXeY)	ν(H-Xe)
HXeF		1.6915	2.1670	434.0(153)	603.2(0.9)	1882.8(401)
Xe$\cdots$HXeF	4.5082	1.6914	2.1670	433.9(160)	610.3(1.1)	1883.7(403)
HXeCl		1.7252	2.6884	246.8(64)	523.2(0.5)	1698.0(1148)
X$\cdots$HXeCl	4.0798	1.7248	2.6898	246.2(68)	531.0(0.5)	1699.5(1133)
HXeBr		1.7437	2.8437	172.5(30)	499.4(0.6)	1616.9(1518)
Xe$\cdots$HXeBr	4.1961	1.7431	2.8449	172.1(33)	509.0(0.5)	1618.5(1524)
HXeI		1.7749	3.0756	137.1(17)	468.0(0.5)	1491.3(2163)
Xe$\cdots$HXeI	4.4708	1.7744	3.0763	136.9(18)	477.0(0.5)	1493.2(2210)

Table 6.2: The computational properties of different (Xe$\cdots$)HXeY molecules at the B3LYP/6-311++G(3df,3pd)/SECP level. Bond lengths are given in Å and frequencies in cm^{-1}, with the corresponding intensities [km/mol] in parentheses.

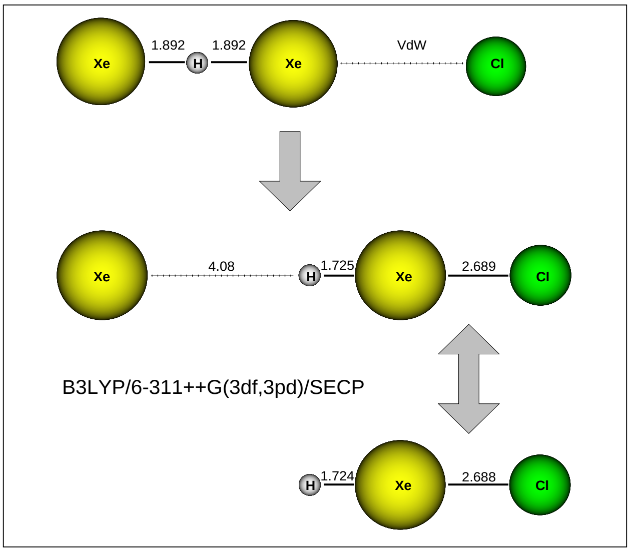

Figure 6.5: Schematic representation of the DFT (B3LYP) geometry optimization of XeHXeCl. Starting from a linear $(XeHXe)^+$ cation and a Cl^- anion at a large distance, the calculation smoothly converges to an HXeCl molecule, with the second Xe atom being pushed left to a distance appropriate for a weak Van-der-Waals bond. The resulting geometry of the HXeCl "perturbed" by the second Xe atom is almost identical to that of the "free" HXeCl.

Some of the results are summarized in Table 6.2. The calculated geometries and vibrational frequencies for the HRgY species are in good agreement with the previous theoretical results [26], and they overestimate somewhat the frequencies observed in solid neon. To check the effect of additional solvation, we have optimized the four-atomic RgHRgY species, starting from the geometry one might expect for the $RgHRg^{+}Y^{-}$ species, that is from the optimized geometry of $RgHRg^{+}$, with the halogen at a relatively large distance from one of the rare gas atoms. As one can see in Fig. 6.5, the optimization smoothly converged to a $Rg\cdots HRgY$ geometry, yielding the HRgY species with an almost identical geometry and frequencies as obtained from the triatomic calculations. The remaining rare gas atom was pushed away to a comfortably large van-der-Waals distance. This result, coupled with the ability of the HRgY compounds to exist in the weakly interacting neon matrix provides a strong evidence, that these do not owe their existence solely to the stabilization by the matrix, but should be capable of independent existence as free gas phase molecules.

6.5 Summary

The infrared spectra of the noble gas compounds HXeCl, HXeBr and their deuterated analogues, and possibly also of the xenon dihydride molecules were observed in solid neon. Their detection in the weakly interacting neon suggests that they should be capable of existence as free molecules even without the stabilization effect of the matrix, a conclusion supported also by DFT calculations. A mechanism for the formation of these xenon compounds is proposed, explaining the observation that they form in the highly diluted neon matrices with similar efficiencies as in solid xenon.

Part IV

Mass-selected Species

Chapter 7

Mass-selected CS_2^+ and $C_6F_6^+$ in Neon

Die Wahrheiten der Menschen sind die unwiderlegbaren Irrtümer.
FRIEDRICH NIETZSCHE

Infrared, visible as well as laser induced fluorescence and excitation spectra are obtained for several simple cations deposited from a mass selected ion beam. In the present chapter we demonstrate the successful and clean mass selection by presenting spectra of samples obtained by depositing the isotopic $^{34}S^{12}C^{32}S^+$ ion in natural isotopic abundance, and analyzing its spectrum. Spectra of $C_6F_6^+$ deposited from a 20 eV ion beam exhibit quite different inhomogeneous line profiles, suggesting that even the moderately high kinetic energies result in considerable solid damage. Analysis of the spectra indicates that the Jahn-Teller distorted vibrational structure in the doubly degenerate ground state of $C_6F_6^+$ is strongly perturbed in the newly formed sites, which are presumably of lower symmetry. A 33-46 cm^{-1} splitting of the origin and other totally symmetric bands in emission is tentatively attributed to the spin-orbit splitting in the $^2E_{1g}$ ground state.

7.1 Introduction

One of the major aims of the matrix isolation technique was the preparation, stabilization, and spectroscopic characterization of radicals, ions, clusters and similar highly reactive, transient species [15, 17]. While there are many methods for generating these reaction intermediates and transients, most of them share the same shortcoming, in that the species of interest are not prepared in pure form, but in a more or less complex mixture with a variety of other species. Also since the early days, an obvious solution to this problem was frequently considered: isolating the desired ions or molecules by means of mass selection. While conceptually it appears simple, implementation of this method proved for a whole variety of reasons to be quite elusive [25, 102].

In the first place, only for relatively few species it is easy to generate ion beams of sufficient intensity to accumulate sufficient concentration for their spectroscopic characterization. Another difficulty lies in the fact that in order to mass select the ions, they typically have to be accelerated to rather high energies, and to slow them down sufficiently for successful deposition is not a trivial task. Even if their energy can be reduced to 10-20 eV, an ion with this energy striking the matrix whose atoms are bound by few meV will produce a lot of damage, can vaporize hundreds of atoms, penetrate deep into the matrix [81], and react with impurities and other species present in the solid [101], thus defeating the major aim of matrix isolation. Final problem lies in the space charge resulting from accumulation of the charged species in the nonconducting rare gas matrix [25]. This may result in stray electric fields deflecting the molecular ion beam and further complicating the ion deposition.

In spite of the problems outlined above, there has been in the last decade a steady progress in this field, indicating that the problems are not insurmountable. Several different groups have reported successful deposition of mass selected ions and observations of their spectra [81, 82, 85, 86, 25, 100, 116, 117], and in particular the trailblazing experiments of MAIER and his group [23, 102, 103] have demonstrated that the problems can be solved.

We have now constructed an apparatus for mass selected ion deposition in our laboratory, which is in many respect similar to the successful design of MAIER and coworkers. The subject of the present chapter will be some interesting results and insights obtained in the first experiments using the new apparatus investigating individual isotopic species of the CS_2^+ and $C_6F_6^+$ cations.

7.2 Experimental

As noted above, the apparatus constructed in our laboratory has features similar to that of the Maiers group, and it is described in detail in section 2.4. The ion source in our experiment consists simply of a 12 mm Swagelok T piece. The precursor gas flows through the collinear sections and 50 W of 2.45 GHz microwave power are applied to a needle electrode located in the perpendicular arm. The pressure in the source chamber evacuated by a 360 l/s turbo-molecular pump is 10^{-4}-10^{-2} mbar. To improve the confinement of the charged species produced in the discharge, we use the magnetic field from a ring shape magnet surrounding the Swagelok. The source is typically held at +20 V, and the discharge products pass through a grid and are accelerated towards a 2 mm skimmer held at -20 V. Since both cw experiments, as well as experiments with a pulsed laser vaporization source were foreseen in our apparatus, we have opted for a quadrupole mass filter which, unlike for instance TOF, allows both modes of operation.

The ions produced in the source pass through a skimmer, are focused using an einzel lense and deflected 90^o in a quadrupole electric field. Depending on polarity, the ionic species are either deflected towards a Faraday cup, permitting to measure the total source ion current, or in the opposite direction, to be focused by a second lense, L2, onto the entrance aperture of the quadrupole mass filter. The neutrals jet remains undeflected and is pumped by a second 360 l/s turbo-molecular pump.

The mass selection is accomplished with a modified commercial triple stage HIDEN HAL/3F quadrupole filter with 12 mm rods, which has a specified mass range of up to 500 amu, and a better than unit mass resolution throughout this range. There is a trade-off between resolution and transmission which is 10%, but can be made higher by sacrifying resolution. The quadrupole mass filter was fitted with 7 mm entrance and exit apertures, and is differentially pumped by a 150 l/s pump.

Following mass selection, the ion beam is directed towards the matrix substrate by means of a further einzel-lens L3. The substrate, a silver coated copper plate, is cooled by a LEYBOLD RDG 580 closed-cycle refrigerator to 7-8 K. The ion beam is deposited on the substrate simultaneously with the matrix gas, neon in the present case. In order to maintain the overall neutrality of the matrix, and avoid building up space charges and stray fields, the matrix was sprayed by electrons from a hot tungsten filament held at negative potentials of up to $U_{Fila} = -200$ V. We experimented with alternating the ion and electron deposition, but in the end continuous operation proved to be most efficient, with optimal results being obtained with the electron current being maintained at about five times the ion current.

In order to optimize the experiment, the ability to measure the ion current is essential. For this purpose, one Faraday cup permitting measurement of the total ion current is located in the deflection chamber. A second detector close to the cold surface allows measuring the mass selected ion current. The weak currents are amplified by a FEMTO DLPCA 100 current amplifier and digitized in the quadrupole control unit. Currents as low as 100 fA can be easily detected and we obtain mass spectra with S/N better than 10000:1. With the mass filter set to the desired mass, all the experimental parameters can be adjusted for maximum current. With our microwave discharge source we could produce for both CS_2^+ and $C_6F_6^+$ mass-selected currents of up to 2 nA.

After deposition, the matrix is rotated 120° and then the matrices are characterized spectroscopically using a BRUKER IFS 120 HR Fourier transform spectrometer, equipped with beam splitters and detectors for the 500 - 30000 cm^{-1} spectral range. IR absorption spectra are measured with a liquid nitrogen cooled MCT (mercury-cadmium telluride) detector at a resolution of 0.06 cm^{-1}, whereas all other spectra were recorded with 0.5 cm^{-1} resolution. Laser excitation spectra are measured using an Ar^+ laser pumped and power stabilized dye laser operating with a stilbene-3 dye. The total emission of the sample is detected with a PMT (and appropriate optical filters) connected to a lock-in amplifier. Laser induced fluorescence spectra are measured with the FT spectrometer using the same detector at a resolution of 0.5 cm^{-1}.

7.3 Results and Discussion

In our initial experiments we have investigated several ions whose matrix spectra are well known from previous studies. To produce the ions, we have employed a microwave discharge through a low pressure precursor gas either pure or diluted with an inert buffer gas. In the first place, the mass spectrum of the ions emanating from the discharge was repeatedly recorded, and the source conditions were optimized for the ion of interest.

7.3.1 The CS_2^+ Cation

A typical mass spectrum obtained using CS_2 is presented in the Fig. 7.1a, which shows the ion current on a logarithmic scale against the selected ion mass. After some optimization, the strongest peak is indeed the parent ion, CS_2^+, accompanied with ^{13}C and ^{34}S isotopic satellites. Also present is a number of easily identifiable fragments, in particular S_2, CS, S, and C. Typically the most intense mass peaks from the source corresponded to an ion current of about 1-2 nA.

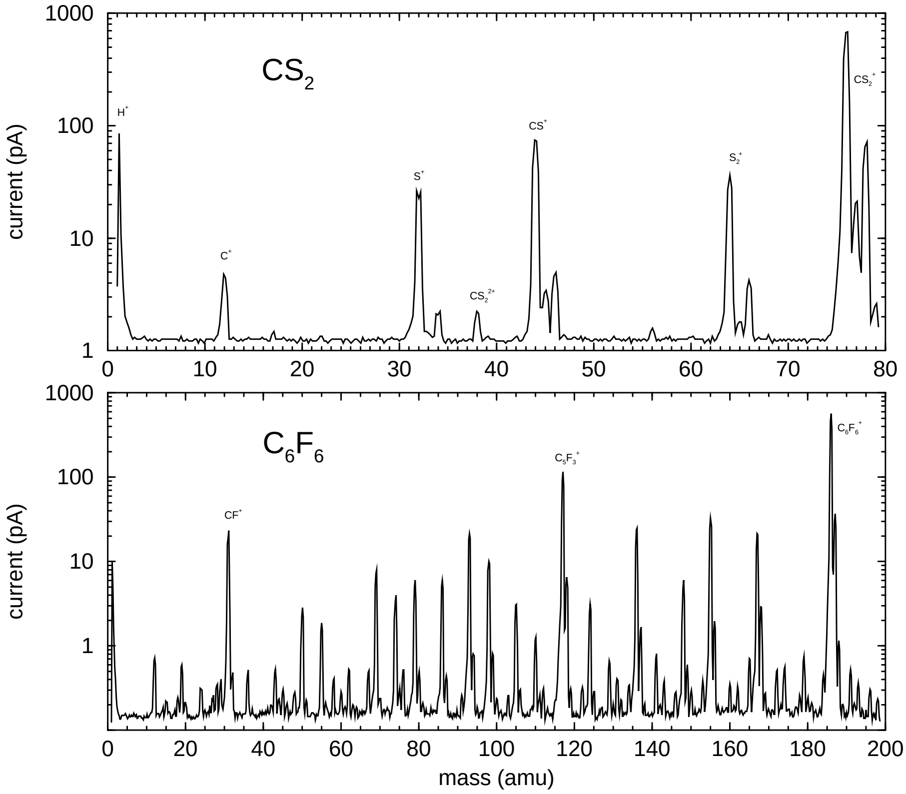

Figure 7.1: Mass spectra obtained from our microwave discharge source for the ions investigated in this work: CS_2^+ (a) and $C_6F_6^+$ (b).

In the small inset of Fig. 7.2 we present an infrared spectrum of a sample resulting from a 3h deposition of 1.5 nA current of ion mass 76 amu. In spite of the nearly a factor of 10 shorter deposition time than in the experiments of Leroi et al, a weak sharp peak at 1206.92 cm^{-1}, very close to the 1207.1 cm^{-1} frequency assigned by them to the v_3 asymmetric stretching vibration of CS_2^+ in solid neon [101], is clearly observable in the spectrum. In contrast with their study, we find in our samples little evidence of either the CS fragment at 1273.7 cm^{-1}, or of the CS_2^- anion at 1159.4 cm^{-1}. If present at all, their concentrations relative to that of the CS_2^+ cation must be at least a factor of ten weaker than in the earlier experiments. We have therefore no information as to the identity of the negatively charged species maintaining neutrality of the matrix. The absence of CS suggests that dissociative recombination with of the CS_2^+ cation with electron does not occur to any appreciable extent in our study.

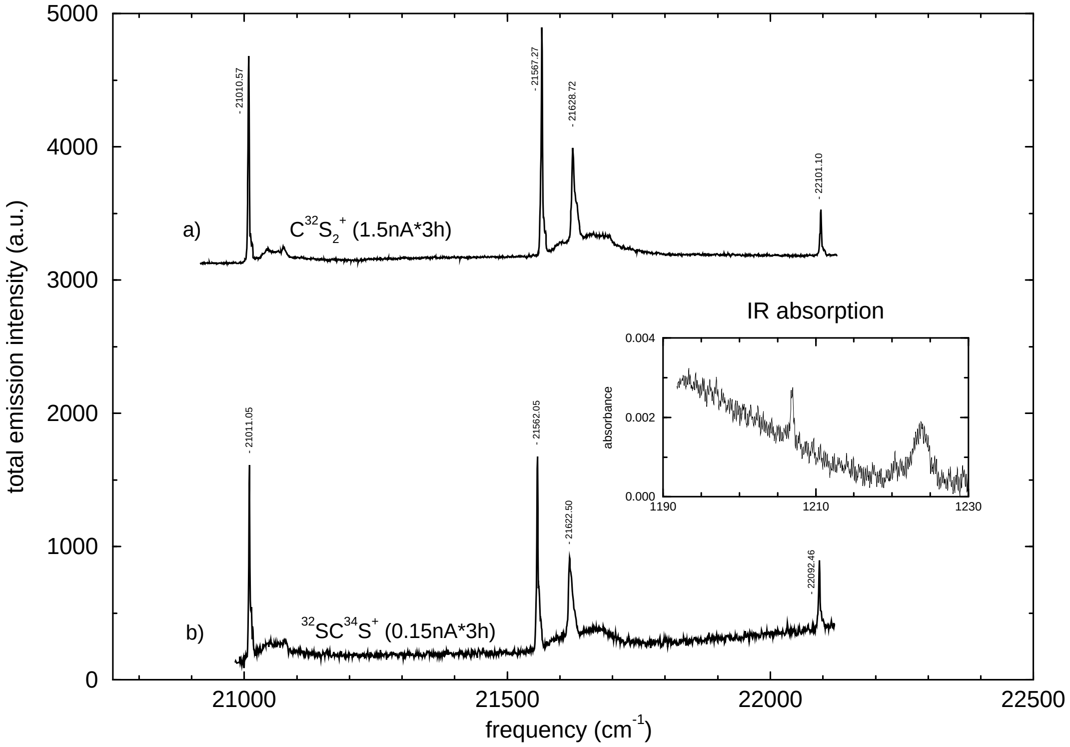

Figure 7.2: Partial excitation spectra of the mass-selected $^{12}\mathrm{C}^{32}\mathrm{S}_2^+$ (a) and $^{32}\mathrm{S}^{12}\mathrm{C}^{34}\mathrm{S}^+$(b) ions in solid neon matrices. The inset shows the infrared absorption spectrum of the former ion.

The presence of CS_2^+ is then unambiguously confirmed by the laser induced fluorescence experiments. Fig. 7.2a shows a total excitation spectrum of the matrix obtained by scanning a laser directed onto the matrix sample over the spectral range near the origin of the well known A $^2\Pi_u \leftrightarrow$X $^2\Pi_g$ CS_2^+ transition [47,48]. The spectrum shows clearly the (0,0,0) origin band at 21010.57 cm^{-1}, as well as several excited vibrational levels, the (1,0,0), (0,2,0) Fermi resonance doublet at 21567.27 and 21628.72 cm^{-1}, and the (2,0,0) level at 22101.0 cm^{-1}.

The remaining, and most important question which has to be answered is whether the observed CS_2^+ are really due to the ion deposition, or whether they could be due to neutral CS_2

from the source reaching the matrix, and being ionized by the electrons from the tungsten filament, or by the ions from the molecular beam. This question is unambiguously resolved by the Fig. 7.2b from a separate experiment, where the mass filter was tuned to mass 78 rather than 76, and a current of 0.15 nA deposited again over 3 hours. One obtains a spectrum very similar to Fig. 3a, but with the bands distinctly shifted to 21011.05, 21562.05, 21622.50, and 22092.46 cm^{-1}. These are clearly attributable to the $^{34}\mathrm{S}^{12}\mathrm{C}^{32}\mathrm{S}^+$ molecular ion present in a natural isotopic abundance in our sample.

(v_1,v_2,v_3)	$^{32}\mathrm{S}^{13}\mathrm{C}^{32}\mathrm{S}^+$	$^{32}\mathrm{S}^{12}\mathrm{C}^{32}\mathrm{S}^+$	$^{32}\mathrm{S}^{12}\mathrm{C}^{32}\mathrm{S}^+$	$^{34}\mathrm{S}^{12}\mathrm{C}^{32}\mathrm{S}^+$
	from Ref. [195]		this work	
(2,0,0)	22063	22114	22101.1	22092.5
(0,2,0)	21601	21639	21628.7	21622.5
(1,0,0)	21541	21578	21567.3	21562.0
(0,0,0)	21011	21016	21010.6	21011.0
(1,0,0)	20402	20398	20392.9	20398.5
(0,2,0)	20325	20318	20312.9	20317.4
?			19935.7	
(2,0,0)	19809	19792	19788.3	19797.4
(1,2,0)	19710	19700	19695.6	19710.1
(0,4,0)	19627	19600	19595.4	19604.2
(3,0,0)	19218	19188	19202.1?	19197.2 ?
(2,2,0)	19101	19082	19076.6	19094.3
(1,4,0)	19019	18996	18992.7	19009.0
(0,6,0) ?	18912		18863.0	
(0,0,2)	18671	18598	18592.8	18598.6
(1,0,2)	18080		17994.2	18006.0
(0,0,4)			16170.3	
(1,0,4)			15589.7	

Table 7.1: Observed bands of mass-selected CS_2^+ in solid neon.

A resolved fluorescence spectrum of CS_2^+ is shown in Fig. 7.3, and a similar spectrum was also recorded for the isotopic $^{34}\mathrm{S}^{12}\mathrm{C}^{32}\mathrm{S}^+$ cation, with the observed bands and their assignments listed in the Table 7.1. The measured frequencies are in general in good agreement with previous studies, but in view of the higher signal to noise in the present work, a number of new bands was detected. The most prominent features in the emission spectrum are “Fermi polyads” due to the near resonance between v_1 and $2v_2$. While the assignments of the first two polyads, that is the resonant (1,0,0), (0,2,0) levels and the levels involving the $2v_1$ overtone: (2,0,0), (1,2,0) and (0,4,0) are quite unambiguous, for the higher overtones the spectra become more complex, and more levels are detected than expected. Some of this complexity probably arises from the Renner-Teller splitting in the degenerate X $^2\Pi_g$ state, or is caused by additional resonances involving the v_3 asymmetric stretching mode.

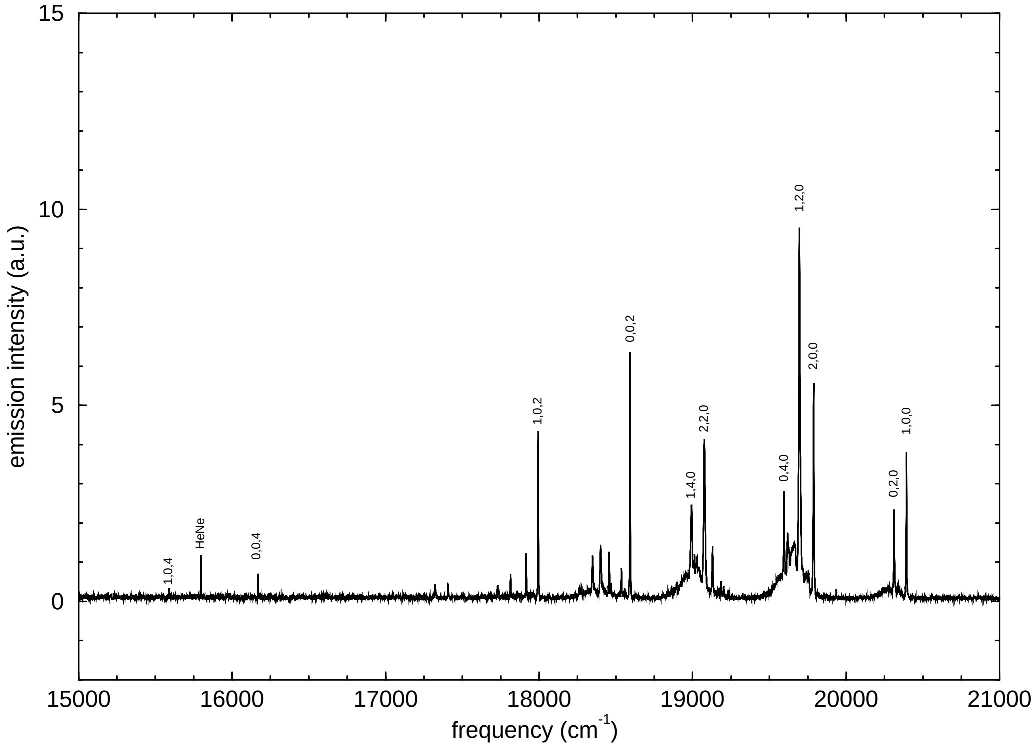

Figure 7.3: Laser induced fluorescence spectrum of the mass-selected ^{12}C^{32}S$_2^+$molecular ion excited at 21567 cm^{-1} (1,0,0).

A strong band at 18592.98 cm^{-1} is clearly the overtone of the asymmetric stretching vibration, yielding a value of $2v_3''$ =2417.75 cm^{-1}. This band is again origin of a series of polyads due to combinations with ν_1'' and $2\nu_2''$. Combining the frequencies of $2\nu_3$" = 2417.80 and $4\nu_3$" = 4840.30 cm^{-1}, one can deduce the molecular constant values of ω_3" = 1207.14 and x$_{33}$ = -0.5875. The asymmetric potential displays negative anharmonicity, that is the level spacing increases with the value of the vibrational quantum number v. This is usually attributed to the presence of a quartic term in the potential energy expression, and one treats the energy levels in terms of either a harmonic oscillator with a perturbing quartic term, or more commonly as a mixed harmonic-quartic oscillator, where the constant a changes from 0 to 1 as one goes from a pure harmonic to a pure quartic oscillator

$$H_m = P^2 + (1-a)Q^2 + a^{2/3}Q^4 \tag{7.1}$$

By setting up the P and Q matrices in a harmonic oscillator basis set, one gets from the observed $2\nu_3$" and $4\nu_3$" levels the constant $a = 0.004724$. In either case, either using the Morse oscillator, or mixed harmonic-quartic oscillator one can compute an almost identical value of the vibrational frequency ν_3 = 1208.31 cm^{-1}. Examination of the infrared absorption spectrum in this region reveals a weak, sharp band fairly close to the computed frequency, at 1206.92 cm^{-1}, which disappears upon annealing of the sample.

In Table 7.1 we also list the frequencies measured for the isotopic $^{34}S^{12}C^{32}S^+$ ion. In the previous studies both normal $^{12}C^{32}S_2^+$ as well as the isotopic $^{13}C^{32}S_2^+$ ions were investigated [196, 195]. Based on the isotopic shifts it was concluded that in both electronic states involved in the transition the ν_1 and $2\nu_2$ levels are almost perfectly mixed. While one would expect the symmetric stretching vibration ν_1 to exhibit no ^{13}C isotopic shift, $\rho \approx 1.0$, while for ν_2 an isotopic parameter $\rho \approx 1.034$ can be predicted, both ν_1 and $2\nu_2$ exhibited almost identical shifts just in the middle between these two values. Basically the same conclusion can be made in the present work based on the observed ^{34}S isotopic shifts. Strictly speaking, $^{34}S^{12}C^{32}S^+$ is no longer a symmetric $D_{\infty h}$ molecule, and therefore also the odd overtones, for instance the ν_3 and $3\nu_3$ levels could in principle appear directly in the spectrum. Unfortunately, due to the relatively low isotopic abundance of ^{34}S the spectra of the mixed isotopomer exhibit a somewhat lower signal to noise ratio, and these levels were not detected.

7.3.2 The $C_6F_6^+$ Cation

Another previously well known ion which we have now investigated with our new experimental apparatus is $C_6F_6^+$, the hexafluorobenzene cation. It is known that it possesses a fully allowed $\pi \leftrightarrow \pi^*$ transition in the visible, and is known to fluoresce in matrices with close to unity quantum yield [122]. To produce the ion, we have again employed a microwave discharge through a pure parent C_6F_6 at a pressure of about 10^{-3} mtorr. One of the problems of such approach is the extensive fragmentation of the parent, resulting in a very complex mass spectrum. As shown in Fig. 7.1b after optimization the parent ion is the strongest peak in the spectrum, but a large number of fragments and other reaction products is observed, with just about any $C_nF_m^+$ ion with n and m ranging up to at least 8 being present.

In Fig. 7.4 we compare an absorption spectrum of a sample resulting from 4 h deposition with the mass filter set to 186 amu with the corresponding excitation spectrum. This was obtained by monitoring the intensity of the sample fluorescence, and scanning the exciting laser in this spectral region. A very strong emission clearly attributable to $C_6F_6^+$ is indeed observed, but both the absorption and laser excitation spectra exhibit some interesting differences when compared with the previous studies, where the cation was produced by in-situ 1216 Å Lyman-α vacuum UV radiation photoionization of the parent hexafluorobenzene. While the photo-ionized spectra exhibited essentially a single site and a narrow inhomogeneous distribution, the ion-beam deposited samples contain, besides the “major” $C_6F_6^+$ site A with origin at 21551.77 cm^{-1}, numerous other sites, which exhibit appreciable spectral shifts, both to higher and lower energies.

Some time ago we have similarly compared spectra of several ionic species prepared in our laboratory by in situ photolysis of the parent neutrals in neon matrices, with the corresponding species deposited by Maier and coworkers from mass selected ion beams [104, 105]. While the ionization produced matrices yielding well defined, sharp lines, the ion beam deposition resulted in broad, structured bands with widths exceeding 150 cm^{-1}. We have at that time explained this difference by inhomogeneous broadening, due to damage to the neon matrix caused by the impact of the energetic, $\approx$60 eV ions. The present investigation seems to confirm this interpretation. While the in situ photolysis produces a single site with origin at 21551.77 cm^{-1}, even though in

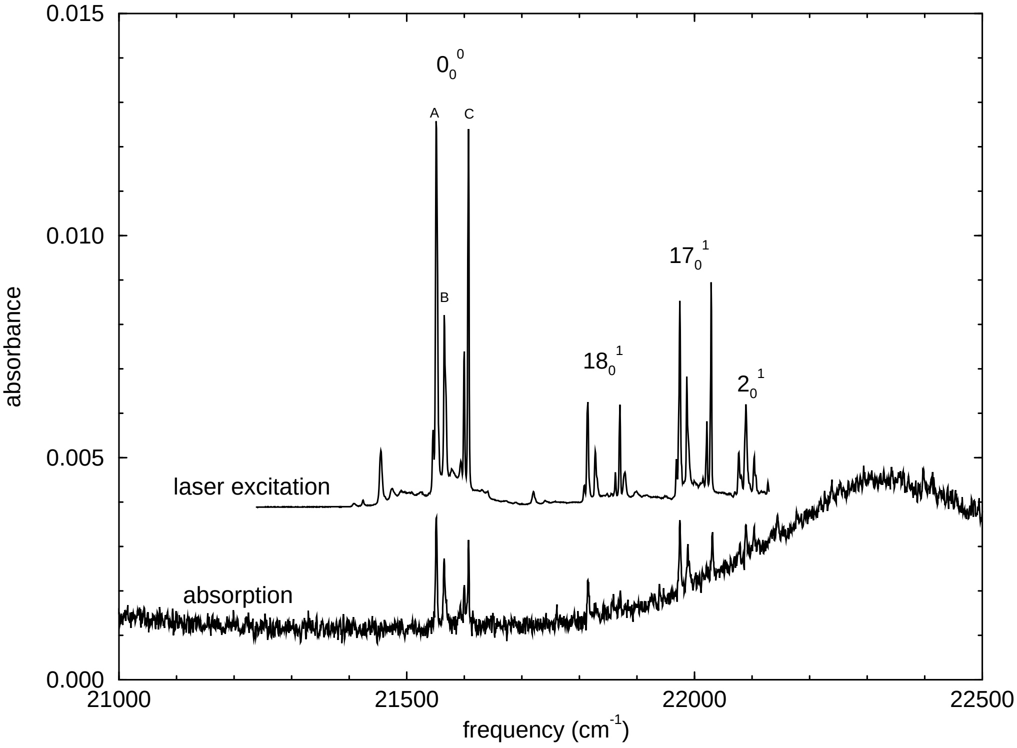

Figure 7.4: Laser excitation (top) and absorption (bottom) spectra of the hexafluorobenzene radical cation, $C_6F_6^+$. Besides the bands due to the "main" site A, note the presence of several additional, spectrally shifted sites.

our case the energy of the ions is believed to be ≈ 20 eV, their deposition results in about a dozen discrete sites, whose origins span a range of more than 200 cm^{-1}, from 21409.43 to 21640.44 cm^{-1}. In one experiment, on the other hand, where the energy of the deposited ions was lowered, the subsidiary sites almost disappeared, and the "main" site which was observed and investigated in the previous studies was dominant.

Mode	from Ref. [122]	Site A	Site B	Site C
ν'_2	540	537.4	537.5	
ν'_{17}	426	422.5	420.8	424.0
ν'_{18}	265	263.9	263.2	263.5
0-0 X_1	21558	21551.8	21565.3	21607.0
0-0 X_2			32.8	46.1
ν_{18}	289	288.8	294.7	296.9
ν_{18a}			305.0	308.3
ν_{17}	417	417.2	432.8	440.9

Mode	from Ref. [122]	Site A	Site B	Site C
ν_{17} + ν_{18}	498	497.9	500.9	503.0
$2\nu_{18}$	508	508.8		
		529.9	528.6	541.1
ν_2	554	553.1	553.6	554.7
		560.3	560.4	560.5
			567.2	
ν_2 X_2			585.5	599.1
		688.2	710.2	707.6
$3\nu_{18}$	699	698.5	721.9	731.4
	759	758.4		
	770	770.0		
$2\nu_{17}$	797	797.3	814.7	816.2
		801.2		823.8
	826	825.9		
		830.1		
ν_2 + ν_{18}	843	842.6	848.9	851.9
ν_2 + ν_{18a}			859.0	862.7
$4\nu_{18}$	919	919.3		
ν_2 + ν_{17}	972	971.2	986.8	995.4
ν_2 + $2\nu_{18}$	1052	1052.0		
$2\nu_2$	1107	1106.5	1107.0	1108.5
$2\nu_2$ X_2			1141.0	1153.1
ν_{16}	1226	1225.0	1246.5	
ν_2 + $3\nu_{18}$	1253	1252.2	1274.8	1286.2
	1280	1278.8		
		1310.1		
ν_2 + ν_{17} + $2\nu_{18}$ (?)	1324			
ν_2 + $2\nu_{17}$	1352	1350.7		
$2\nu_2$ + ν_{18}	1397	1396.0	1402.3	
$2\nu_2$ + ν_{18a}			1412.5	
ν_2 + $4\nu_{18}$	1474	1473.3		
$2\nu_2$ + ν_{17}	1526	1524.9		
$2\nu_2$ + $2\nu_{18}$	1605	1604.6		
$3\nu_2$	1661	1659.6	1660.2	?
	1682	1681.4		
ν_{15}	1698	1694.1	1696.2	1706.6
	1734	1732.9		
	1805	1805.2		
		1966.5		
	2172	2165.2		

Mode	from Ref. [122]	Site A	Site B	Site C
	2220	2219.9		
$\nu_{15} + \nu_2$	2250	2248.9		
		2281.6		
	2432			

Table 7.2: Observed transitions of $C_6F_6^+$ in solid neon. All values in cm^{-1}.

In Table 7.2 we list the observed transitions of $C_6F_6^+$ both for the “main” site A, as well as for the two strongest “new” sites B and C, which are blue shifted by 12.9 and 55.3 cm^{-1}, respectively. In Fig. 7.5, a comparison of the spectra and frequencies of the “main” site A with those of the new sites B and C reveals, that while the progression in the totally symmetric mode, ν_2, is essentially identical for the three sites, and also identical with the known gas phase frequencies, the other levels involving the Jahn-Teller active modes ν_{18} and ν_{17} [197] exhibit strong perturbations. Thus the 288.8 cm^{-1} ν_{18} level, is in both of the strongest perturbed sites split into two components, both of them blue shifted to about 295 and 305 cm^{-1}, respectively. Similarly, ν_{17} which occurs at 417.2 cm^{-1} in the main site is shifted to 432.8 and 440.9 cm^{-1} in the two other sites. This applies also to their combination and overtone bands. In general, the vibrational levels involving the Jahn-Teller active modes are in all the new sites strongly shifted and sometimes split in several components, and new absorptions appear. Also the 0-0 band, and each of the bands of the strong, totally symmetric ν_2 progression which is seen up to v_2=3, exhibit in the spectra of the new sites a broader satellite band, shifted in emission by $\approx$ 33 and 46 cm^{-1}, respectively.

A tentative interpretation of these observations is that when produced by in situ photolysis of the parent, the $C_6F_6^+$ cation is in an unperturbed site with relatively high symmetry. When, however, the ion is deposited in the matrix from the gas phase with kinetic energies of $\approx$ 20 eV, lower symmetry sites, perhaps with nearby vacancies, are produced and populated, which strongly affect the Jahn-Teller distortion, perturb the related vibrational structure, and relax the selection rules. An interesting question involving the doubly degenerate ground state of $C_6F_6^+$and similar cations is the magnitude of the spin-orbit splitting. Several older theoretical works suggested that this is probably small [198], but there is little *a priori* evidence on this point. Compared with the spin orbit constants in a number of small compounds of first row elements, the observed 33-46 cm^{-1}separation of the two components of the origin band, as well as of the other totally symmetric levels would seem to be of the right order of magnitude to be assigned to the spin-orbit splitting of the degenerate X $^2E_{1g}$ ground state of the $C_6F_6^+$ cation.

If one accepts this assignment, then considering that the magnitude of the splitting changes by some 30% between the two sites examined, the question arises as to how much of this is intrinsic, free $C_6F_6^+$ splitting, and how much is due to the asymmetric environment. In other words, one might ask if one sees an extra component because the selection rules are relaxed, and a level which is not accessible in a symmetric site becomes visible when the site symmetry is lowered, or because the initially degenerate and unresolvable levels were split by the asymmetry. An unambiguous answer to this question will require additional study. It should be noted,

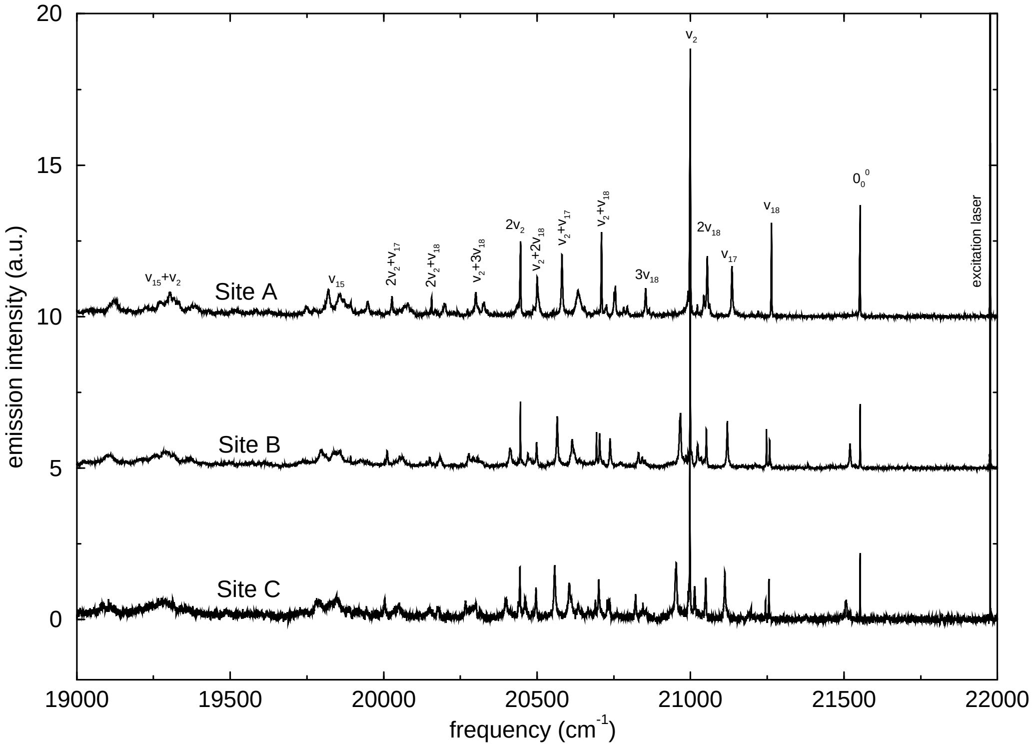

Figure 7.5: Overview of the LIF spectrum of the main site A compared with those of two of the "perturbed" sites, denoted B and C. For ease of comparison, the spectra of these sites were shifted to make the 0-0 origins overlap. Note the splitting of the spectral lines, as well as the presence of broader satellite bands near the 0-0 origin and other totally symmetric bands.

that the spin-orbit splitting was neglected in most previous treatments of the substituted benzene cations. Strictly speaking, however, the spin-orbit and Jahn-Teller interactions are not independent of each other, and if both splittings are non-negligible, both would have to be simultaneously considered in a rigorous treatment of the X $^2E_{1g}$ ground state vibrational structure.

Jahn-Teller Effect in the Benzene Cation and its Symmetrically Substituted Homologues

Halogenated benzenes represent a group of compounds whose radical cations have been extensively studied by matrix spectroscopy [199, 122]. Simple Hueckel Molecular Orbital theory shows that the unhybridized p electrons on the six carbon atoms of the benzene ground state occupy an a_{2u} and a doubly degenerate e_{1g} binding molecular orbital, yielding a stable, closed shell structure. In the cation one of the electrons from the highest occupied e_{1g} molecular orbital (HOMO) is missing, resulting in a doubly degenerate X $^2E_{1g}$ ground state. A $\pi - \pi$ promotion of one of the a_{2u} electrons into the e_{1g} orbital yields a low exciting B $^2A_{2u}$ electronic state, and represents the lowest energy fully allowed electronic transition of the cation. In benzene itself another electronic state resulting from promotion of one of the σ electrons lies below the $^2A_{2u}$

state, and provides a "gateway state" for its non-radiative relaxation, that is its interaction results in severe broadening of the B state and shortening of its lifetime. When, however, at least 2-3 hydrogen atoms on the benzene ring are substituted by halogens, the energy needed for the $\pi - \pi$ relative to the $\sigma - \pi$ excitation is lowered to the extent that the B $^2A_{2u}$ state becomes the lowest excited electronic state. The pathway for its non-radiative relaxation is closed, the spectra become sharp, and the radical cations fluoresce with near unity quantum efficiency, and can thus be conveniently investigated by laser induced fluorescence.

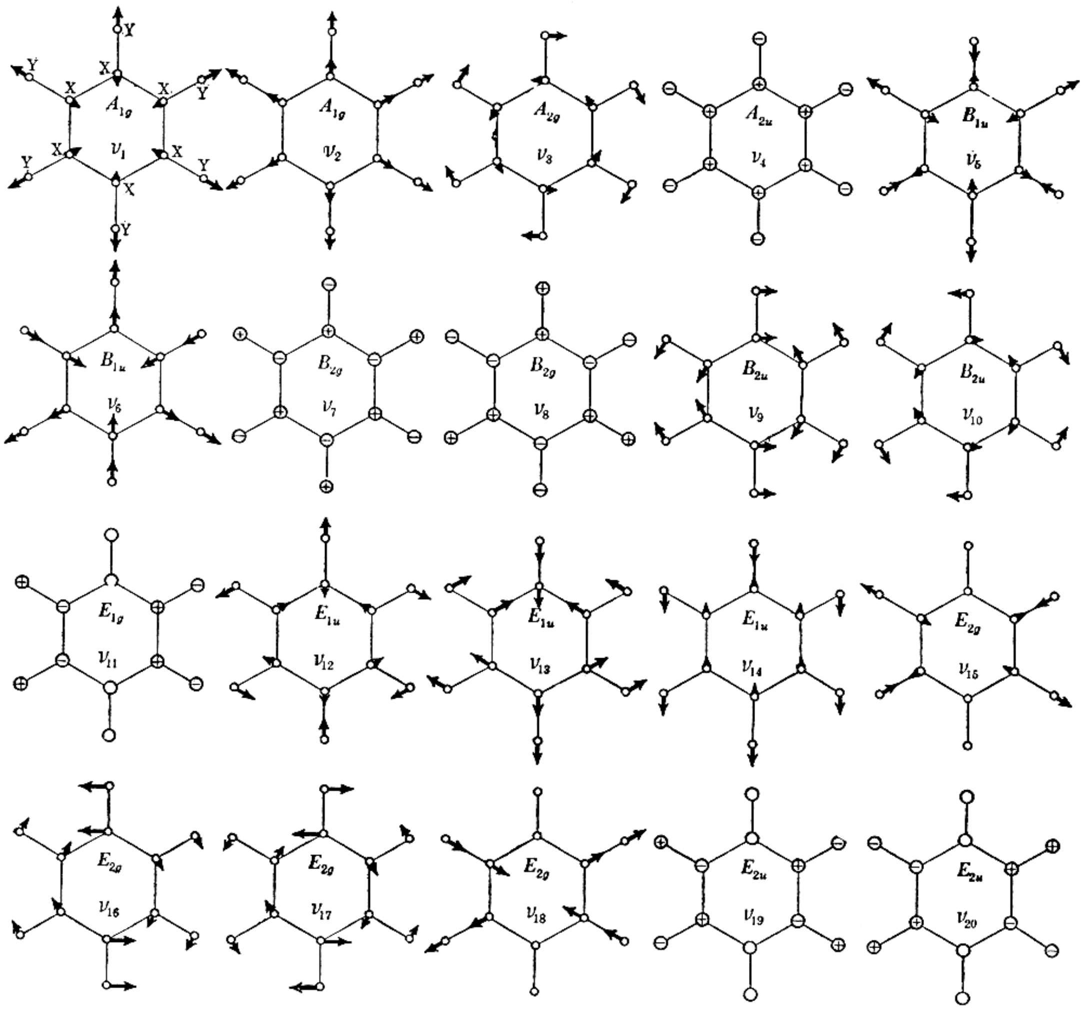

Figure 7.6: Normal vibrations of an X_6Y_6 molecule with D_{6h} symmetry. From Ref. [45]

As we explained in previous publications [122, 197], the emission spectrum shows clearly the distortion of the ion due to Jahn-Teller effect. While in a symmetry allowed transition of a molecule with a D_{6h} symmetry only the a_1 modes ν_1 and ν_2 should appear, most prominent in the spectrum are actually vibrations ν_{18}, ν_{17}, ν_{16}, and ν_{15} (see Fig. 7.6) – precisely the modes of e_{2g} symmetry which according to theory should become active, if the ground state symmetry is lowered from D_{6h} to D_{2h}. The presence of Jahn-Teller effect is then confirmed by analysis of the resolved emission spectra, which unlike the absorption spectra appear quite irregular and erratic – they reflect the vibrational structure of the degenerate ground state distorted by the Jahn-Teller effect.

Local Site Symmetry and Spectroscopic Selection Rules

Interesting insights can be gained by comparing the spectra of the ions in different sites. Ordinarily, such spectra appear to be almost identical except of a uniform shift of all the bands, corresponding to slight differential shifts in the energies of the electronic states involved in the transition. Also in the present case of $C_6F_6^+$, the absorption-laser excitation spectra show just such an effect, the resolved fluorescence, however, exhibits besides the usual uniform shift of all bands, additional changes in the spectrum, reflecting changes in the vibrational structure of the X $^2E_{1g}$ ground state. As noted previously, the structure of this state is distorted due to the Jahn Teller effect, and while the excitation spectrum, reflecting the structure of the upper B $^2A_{2u}$ electronic state consists of regular arrays involving several nearly harmonic vibrational frequencies, the emission spectrum lacks this regularity, with only a progression in the totally symmetric a_{1g} mode ν_2, the "ring breathing" frequency, being clearly recognizable.

The bands of this progression are observable at least to ν_2=2, and they are shown for the main site A in Fig. 7.7, and compared with the corresponding sections of the spectra in the subsidiary sites B and C in the lower panels, whose frequency scales have for clarity been shifted in frequency by 12.9 and 55.3 cm^{-1}, so that the 0-0 bands overlap. One can clearly see that while for the main site a single sharp band is observed for each value of ν_2, in the panels B and C each band has a broader satellite shifted ≈34 and ≈45 cm^{-1}, respectively, towards lower energies. This suggests the presence of a very low lying level above the vibrational level of the ground state as well as above each excited ν_2" level. These energies are way too low to correspond to an intramolecular vibrational mode of the ion, and surely too high to correspond to its rotation. While, in principle, the possibility that this mode could correspond to a "translational" mode of the ion, it is significant that similarly shifted satellites are not observed for the other, non-totally symmetric vibrational levels.

As noted above, the ground state of the cation, X $^2E_{1g}$, is a doublet state, whose spin orbit splitting is unknown. While a few theoretical works discussing this problem predicted a smaller splitting between the fine structure components, the observed value is of the same order of magnitude as, for instance, the fine structure constant $A_v = 77.12 - 0.655v + 0.0057v^2$ (in cm^{-1}) observed in the X $^2\Pi$ ground state of diatomic CF [200]. This raises the possibility that the extra level detected in the subsidiary sites is due to the higher spin orbit component of the ground state. Here again two possibilities have to be considered. Either is the forbidden transition in the main site A too weak to be observed, but becomes allowed in the "perturbed" sites B and C, or is the splitting in the main site too small to be resolved, but the near degeneracy is split in these sites. In either case, the spin-orbit splitting interpretation is consistent with the broader appearance of the satellite bands. In almost every case where spin-orbit splitting in multiplet states in matrices was observed, the higher level was broadened as a result of fast non-radiative relaxation into phonon states built upon the the levels of the lower spin orbit component.

In either case, the most likely cause of this difference between the "main" and "subsidiary"

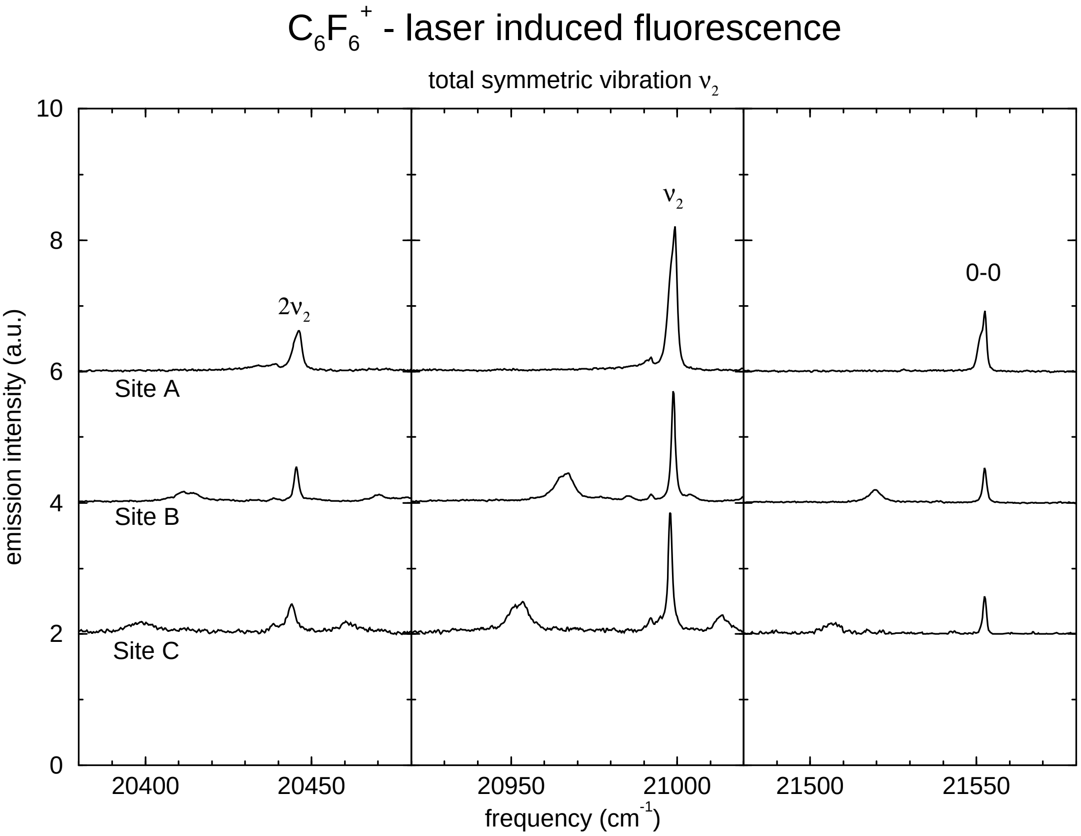

Figure 7.7: Detail of the LIF of $C_6F_6^+$ showing the total symmetric vibration ν_2 in the doubly degenerated electronic groundstate X $^2E_{1g}$.

sites is the local geometry and symmetry, and it is of interest to consider from this point of view the likely nature of the trapping site. The lowest energy structure of rare gas solids is experimentally known to be FCC, but neutron scattering studies have suggested that gas phase deposited sample contain both FCC and HCP regions, with the presence of impurities favoring the growth of the HCP abundance. In either case, the structure consists of identical planes with hexagonally arranged rare gas atoms, with the difference between the HCP and FCC structures being only in the arrangement of these planes. Considering the nearest neighbor distance between two neon atoms, and the geometry of the C_6F_6 molecule, it appears that the most natural way to accommodate the guest is to replace seven neon atoms in one of these planes, as shown in Fig. 7.8, yielding in each case a site of relatively high symmetry. The site will exhibit in an HCP lattice a hexagonal D_{3h} local symmetry, while in the case of FCC it will be D_{3d} with a three-fold improper rotation axis and a center of inversion.

In the case of the in situ produced ions, the geometry of the site is unlikely to change during the photoionization process. We suggest that the symmetry in the subsidiary sites, resulting from the deposition of the energetic ions from the ion beam is lowered as a consequence of the damage. The exact nature of the site is unknown, but it may simply be an additional vacancy, that is an additional matrix atom missing in the immediate neighborhood of the isolated ion. The lowered

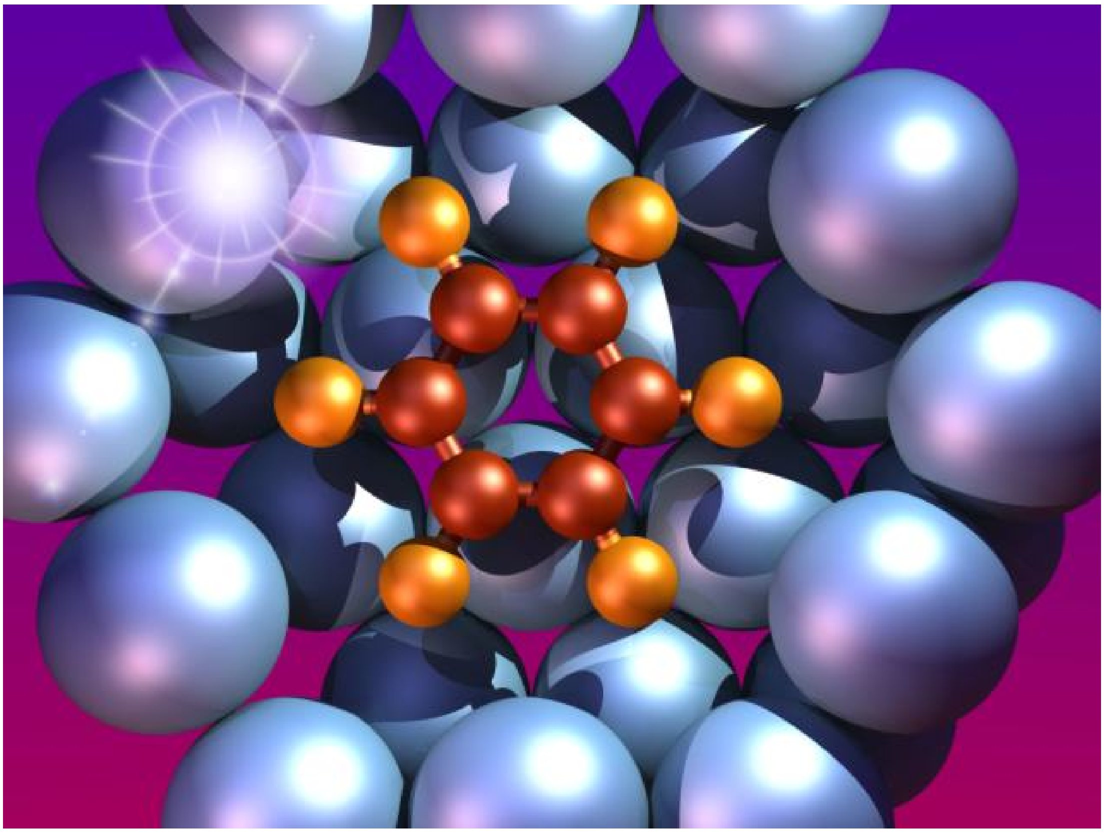

Figure 7.8: The $C_6F_6^+$ cation embedded in a neon matrix in a site with high symmetry.

symmetry has little effect upon the intramolecular vibration - the values of the ν_2 vibrational frequencies and their overtones are to within about 1 cm^{-1} identical in all the three sites, but it appears to affect the selection rules, and also influences the spin orbit splitting between the 1/2 and 3/2 components, since comparison of the B and C sites yields considerably different values of $\approx$ 33 and 45 cm^{-1}, respectively.

Effect of Sites on the Jahn-Teller Distortion

As noted in the above section, the frequencies of the totally symmetric ν_2 mode, and of its overtones are basically unaffected by the changes in the trapping site and its symmetry. Quite different is the behavior of the Jahn-Teller active e_{2g} vibrational modes, as is exemplified by Fig. 7.9. Here the top panel shows sections of the fluorescence spectrum of $C_6F_6^+$ in the main "unperturbed" site A. As shown in the right hand section, easily identifiable in emission are the lowest frequency e_{2g} modes ν_{18} = 288.8 cm^{-1}, ν_{17} = 417.2 cm^{-1}, with several bands previously shown to be due to their combinations and overtones being present at higher energies. An identical pattern of bands is then repeated built upon the totally symmetric ν_2 level, as well as upon its overtones, as shown in the two spectral sections further towards the left.

The bottom two spectra then show the corresponding sections of the spectra in the perturbed

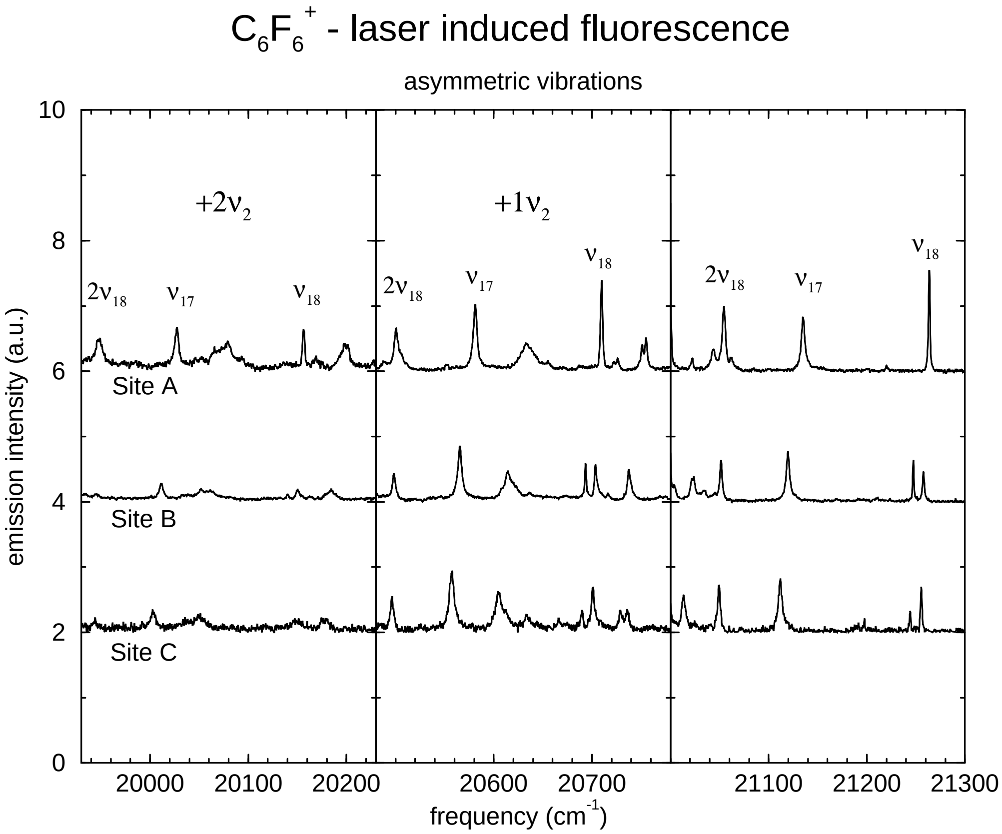

Figure 7.9: Detail of the LIF of $C_6F_6^+$ showing the Jahn-Teller active modes ν_{17} and ν_{18} in combination with ν_2.

subsidiary sites B and C, which have again been shifted by the appropriate amounts needed to make the 0-0 origin bands of all the sites coincide, to make more apparent the changes in the vibrational structure. It is immediately visible that in the place of the ν_{18} level now appear two bands, both of them shifted to higher energies compared with the main site frequency. The two bands are at 294.7 and 305.0 cm^{-1} in the site B and 296.9 and 308.3 cm^{-1} in site C. Similarly also the ν_{17} mode is blue shifted from its 417.2 cm^{-1} frequency in the main site to 432.8 and 440.9 cm^{-1} in the B and C sites, respectively. The same spectrally shifted band patterns are again repeated in combination with ν_2 and $2\nu_2$, as clearly visible in the Figure.

In previous studies of halogenated benzene radical cations it was already noted that while the ground state structures in neon matrix are very similar to the structure observed in the gas phase, the shifts and perturbations of the Jahn-Teller active modes and levels were distinctly larger than those of the levels not involved in the distortion, as in the present case of the totally symmetric a_g ν_2. The present study of the effect of sites gives additional evidence demonstrating this sensitivity of the Jahn-Teller distortion to local environment and its symmetry.

7.4 Conclusion

In the present manuscript preliminary results are presented which are obtained with a new apparatus for deposition of mass selected ions in low temperature matrices. With this apparatus we obtain infrared and visible absorption, as well as fluorescence and fluorescence excitation spectra of mass selected ions. We demonstrate the successful and clean mass selection by presenting spectra of samples obtained by depositing the isotopic $^{34}S^{12}C^{32}S^+$ ion in natural isotopic abundance. Experiments with $C_6F_6^+$ demonstrate, that deposition of ions with high kinetic energy from the gas phase, produces quite different inhomogeneous line profile, and results in a variety of “perturbed” sites, presumably due to nearby defects and vacancies. The emission spectra of the perturbed sites are characterized by appreciable shifts and doubling of the vibrational levels of the degenerate X $^2E_{1g}$ ground state, which may be due to combination of the spin-orbit splitting and the Jahn-Teller effect.

Summary and Outlook

In the scope of this thesis, a new apparatus for the deposition of mass-selected ions in low temperature matrices was constructed. The successful and clean mass-selection was demonstrated by presenting spectra of samples obtained by deposition of isotopic $^{34}S^{12}C^{32}S^+$ cations from a discharge source using CS_2 in natural isotopic abundance as precursor. With the new apparatus, infrared and visible absorption, as well as laser-induced fluorescence and laser excitation spectra are obtained from mass-selected and matrix-isolated ions. Experiments with the $C_6F_6^+$ cation demonstrated that the deposition of ions with high kinetic energy from the gas phase results in a variety of perturbed sites, presumably due to nearby vacancies and lattice defects, producing a different inhomogeneous line profile compared with *in-situ* experiments. The effects of ion beam deposition, like fragmentation or matrix damage, were discussed in detail and the concentration of mass-selected ions in rare gas matrices was examined quantitatively.

Unfortunately, the original purpose to couple our remarkably successful laser vaporization source with the mass-selection apparatus could not be achieved since the source emitted too low average ion currents for spectroscopical investigations. For future experiments, it is thus planned to apply for a new vaporization laser with a higher repetition rate allowing sufficient ion currents.

Parallel to the planning and implementation of the new mass-selection apparatus, research was continued using the old, conventional setup with the most interesting results being presented in this thesis: New insights into the vibronic structure and relaxation of tungsten oxides, as well as the photodissociation of hydrogen halides and, connected with that, the formation of new, neutral rare gas compounds in solid neon.

Absorption and fluorescence spectra of WO and WO_2 in the spectral range from IR to near UV have been investigated identifying several, previously unknown electronic states of WO in the near infrared range. Besides fluorescence from the known visible electronic states, emission from the low lying electronic states in the near infrared and extensive ground state vibrational emission was observed, providing a wealth of spectroscopic information with nearly unprecedented accuracy for a matrix molecule. The interesting relaxation pathways of WO such as inter-electronic cascade processes, which are leading to these emissions, were discussed in detail.

IR absorption spectra of hydrogen halide monomers, the strongly bound oligomers, as well as complexes with the heavy rare gases Kr and Xe have been examined showing that the hydrogen bonding results in a red shift of the bound $YH\cdots X$ frequency and a considerable increase in its intensity. The influence of the hydrogen bonding upon the hydrogen halide photolysis behaviour was discussed and the photolysis products were examined. Annealing of the neon matrices after photolysis resulted in partial reformation of the monomers, as well as the formation of the novel HXeY compounds. A mechanism for the formation of these neutral noble gas compounds in solid neon is proposed and their detection in the weakly interacting neon suggests that they should be capable of existence as free molecules in the gas phase. This conclusion is supported by *ab-initio* quantum chemical calculations, which were also performed for the tungsten dioxide as a comparison with experimental results.

These results, which were obtained with the old setup, the first results of the new mass-selection apparatus, as well as some additional studies not covered by this thesis, led to a series of publications presented in the following list of publications.

List of Publications

1. M. Lorenz, J. Agreiter, A.M. Smith-Gicklhorn and V.E. Bondybey: *"Electronic Structure of Diatomic Boron Nitride"*, J. Chem. Phys. **104**, 3143-3146 (1996).
2. A.M. Smith, M. Lorenz, J. Agreiter and V.E. Bondybey: *"Electronic Structure of Diatomic Boron Carbide"*, Mol. Phys. **88**, 247-254 (1996).
3. M. Lorenz, N. Caspary, W. Foeller, J. Agreiter, A.M. Smith and V.E. Bondybey: *"Electronic Structure of Triatomic Copper (II) Chloride"*, Mol. Phys. **91**, 483-493 (1997).
4. J. Agreiter, M. Lorenz, A.M. Smith and V.E. Bondybey: *"Neon Matrix Spectra and Isotopically Dependent Fluorescence Quantum Yields of* BO_2*"*, Chem. Phys. **224**, 301-313 (1997).
5. M. Lorenz, J. Agreiter, N. Caspary and V.E. Bondybey: *"Relaxation and Vibrational Fluorescence of WO in Solid Neon"*, Chem. Phys. Lett. **291**, 291-299 (1998).
6. M. Lorenz and V.E. Bondybey: *"Isotopically Resolved Spectra of Tungsten Oxides in Solid Neon"*, Chem. Phys. **241**, 127-138 (1999).
7. V.E. Bondybey, U. Achatz, B. Fox, G. Niedner-Schatteburg and M. Lorenz: *"Production of Ion Clusters and High Temperature Species and their Studies by Fourier Transform Techniques"*, Proceedings of the 12th International Conference on Fourier Transform Spectroscopy, August 1999, Waseda University Enterprise Press, pp. 35-38.
8. E.V. Savchenko, A.N. Ogurtsov, O.N. Grigorashchenko, M. Beyer, M. Lorenz, A. Lammers and V.E. Bondybey: *"Radiation-Induced Formation of Stable Charge Centers in Rare-Gas Solids"*, Nucl. Instrum. Methods Phys. Res. B **166-167**, 47-50 (2000).
9. M. Lorenz, D. Kraus, M. Räsänen and V.E. Bondybey: *"Photodissociation of Hydrogen Halides in Rare Gas Matrices, and the Effect of Hydrogen Bonding"*, J. Chem. Phys. **112**, 3803-3811 (2000).
10. M. Lorenz, M. Räsänen and V.E. Bondybey: *"Neutral Xenon Hydrides in Solid Neon and their Intrinsic Stability"*, J. Phys. Chem. A 2000, **104**, 3770-3774 (2000).
11. M. Lorenz and V.E. Bondybey: *"Deposition of Mass-Selected Ions in Neon Matrices:* CS_2^+ *and* $C_6F_6^+$*"*, Low Temp. Phys., accepted

12. E.V. Savchenko, O.N. Grigorashchenko, A.N. Ogurtsov, V.V. Rudenkov, G.B. Gumenchuk, M. Lorenz, A. Lammers and V.E. Bondybey: *"Stability of Charge Centers in Solid Ar"*, submitted to J. Low. Temp. Phys.

13. V.E. Bondybey and M. Lorenz: *"Mass Selected Ions in Solid Neon: Matrix Damage and Site Effects"*, submitted to J. Low. Temp. Phys.

Bibliography

[1] G. Herzberg, *The Spectra and Structure of Simple Free Radicals* (Cornell University Press, Ithaka, 1971).

[2] P. Gerhardt, S. Löffler, and K. H. Homann, Proc. Combust. Inst. 1988 **22**, 395 (1988).

[3] D. Smith and N. G. Adams, Pure Appl. Chem. **56**, 175 (1984).

[4] D. Smith and P. Spanel, Mass Spectrom. Rev. **14**, 255 (1996).

[5] D. G. Torr, *The Photochemistry of Atmospheres: Earth and Other Planets and Comets* (Academic, New York, 1985).

[6] M. Oppenheimer, Acc. Chem. Res. **13**, 378 (1980).

[7] F. Salama, C. Joblin, and L. J. Allamandola, in *The diffuse interstellar bands*, edited by A. G. G. M. Tielens and T. P. Snow (Kluwer Academic Publishers, 1995), p. 207.

[8] D. Smith, Chem. Rev. **92**, 1473 (1992).

[9] T. Oka, in *Molecular Ions: Spectroscopy, Strucure and Chemistry*, edited by T. A. Miller and V. E. Bondybey (North-Holland, Amsterdam, 1983), p. 73.

[10] J. L. Holmes, Org. Mass Spectrom. **20**, 169 (1985).

[11] L. Zandee, R. B. Bernstaein, and D. A. Lichtin, J. Chem. Phys. **69**, 3427 (1978).

[12] U. Boesl, H. J. Neusser, and E. W. Schlag, Z. Naturforsch. **33a**, 1546 (1978).

[13] G. S. Hurst and M. G. Payne, *Principles and Applications of Resonance Ionization Spectroscopy* (Hilger, Bristol, 1988).

[14] L. Zhu and P. Johnson, J. Chem. Phys. **94**, 5769 (1991).

[15] E. Whittle, D. A. Dows, and G. C. Pimentel, J. Chem. Phys. **22**, 1943 (1954).

[16] I. Normann and G. Porter, Nature **174**, 508 (1954).

[17] V. E. Bondybey, A. M. Smith, and J. Agreiter, Chem. Rev. **96**, 2113 (1996).

[18] V. E. Bondybey and J. H. English, J. Chem. Phys. **71**, 777 (1979).

[19] L. B. Knight, Jr., J. Chem. Phys. **78**, 6415 (1983).

[20] A. Thoma, B. E. Wurfel, R. Schlachta, G. M. Lask, and V. E. Bondybey, J. Phys. Chem. **96**, 7231 (1992).

[21] J. Agreiter, Ph.D. thesis, Technische Universität München, 1998.

[22] J. C. Rivoal, C. Grisolia, J. Lignieres, D. Kreisle, P. Fayet, and L. Wöste, Z. Phys. D **12**, 481 (1989).

[23] D. Forney, M. Jakobi, and J. P. Maier, J. Chem. Phys. **90**, 600 (1989).

[24] S. Fedrigo, W. Harbich, and J. Buttet, Phys. Rev. B: Condens. Matter Mater. Phys. **58**, 7428 (1998).

[25] M. S. Sabo, J. Allison, J. R. Gilbert, and G. E. Leroi, Appl. Spectrosc. **45**, 535 (1991).

[26] M. Pettersson and M. Räsänen, J. Chem. Phys. **102**, 6423 (1995).

[27] M. Pettersson, J. Lundell, and M. Räsänen, Eur. J. Inorg. Chem. 729 (1999).

[28] L. Khriachtchev, M. Pettersson, N. Runeberg, J. Lundell, and M. Räsänen, Nature **406**, 874 (2000).

[29] E. Schrödinger, Ann. Pys. **79**, 361,489 (1926).

[30] M. Born and R. Oppenheimer, Ann. Phys. **84**, 457 (1927).

[31] G. Schallmoser, A. Thoma, B. E. Wurfel, and V. E. Bondybey, Chem. Phys. Lett. **219**, 101 (1994).

[32] B. T. Sutcliffe, in *Computational Techniques in Quantum Chemistry*, edited by G. H. F. Diercksen, B. T. Sutcliffe, and A. Vaillard (Reidel, Boston, 1975), p. 1.

[33] H. A. Jahn, Proc. Roy. Soc. A **164**, 117 (1938).

[34] R. Renner, Z. Phys. **92**, 172 (1934).

[35] M. Brommer and P. Rosmus, Chem. Phys. Lett. **206**, 540 (1993).

[36] F. Schwabl, *Quantenmechanik* (Springer–Verlag, Berlin, 1990).

[37] P. Hohenberg and W. Kohn, Phys. Rev. **136**, 864 (1964).

[38] T. Ziegler, Chem. Rev. **91**, 651 (1991).

[39] A. D. Becke, J. Chem. Phys. **98**, 5648 (1993).

[40] M. J. Frisch, G. W. Trucks, H. B. Schlegel, P. M. W. Gill, B. G. Johnson, M. A. Robb, J. R. Cheeseman, T. Keith, G. A. Peterson, J. A. Montgomery, K. Raghavachari, M. A. Al-Laham, V. G. Zekrzewski, J. V. Ortiz, J. B. Foreman, J. Ciolowski, B. B. Stefanov, A. Nanayakkara, M. Challacombe, C. Y. Peng, P. Y. Ayala, W. Chen, M. W. Wong, J. L. Andres, E. S. Replogle, R. Gomberts, R. L. Martin, D. J. Fox, J. S. Binkley, D. J. Defrees, J. Baker, J. P. Stewart, M. Head-Gordon, C. Gonzalez, and J. A. Pople, *GAUSSIAN94*, Gaussian Inc., Pittsburgh PA, 1995.

[41] A. D. Becke, Phys. Rev. **38**, 3098 (1988).

[42] S. H. Vosko, L. Wilk, and M. Nusair, Canadian J. Phys. **58**, 1200 (1980).

[43] C. Lee, W. Yang, and R. G. Parr, Phys. Rev. B **37**, 785 (1988).

[44] M. Endoh, M. Tsuji, and Y. Nishimura, Chem. Phys. Lett. **109**, 35 (1984).

[45] G. Herzberg, *Molecular spectra and molecular structure* (Van Nostrand, Princeton London Toronto Melbourne, 1945), Vol. II Infrared and raman spectra of polyatomic molecules.

[46] E. B. Wilson, Jr., J. C. Decius, and P. C. Cross, *Moelcular Vibrations, The Theory of Infrared and Raman Vibrational Spectra* (McGraw–Hill, New York Toronto London, 1955).

[47] E. Fermi, in *Nuclear Physics* (Univ. Chicago Press, Chicago, 1950), p. 148.

[48] D. R. Miller, in *Atomic and Molecular Beam Methods*, edited by G. Scoles, D. Bassi, U. Buck, and D. Laine (Oxford University, New York, 1988), Vol. I, Chap. 2, p. 14.

[49] T. A. Miller, Science **223**, 4636 (1984).

[50] F. Stienkemeier, W. Ernst, J. Higgins, and G. Scoles, J. Chem. Phys. **102**, 615 (1995).

[51] F. Stienkemeier, J. Higgins, C. Callegari, S. I. Kanorsky, W. E. Ernst, and G. Scoles, Z. Phys. D **38**, 253 (1996).

[52] B. Meyer, *Low Temperature Spectroscopy* (American Elsevier Publishing Company, New York, 1971).

[53] E. Schuberth, M. Creuzburg, and W. Müller-Lierheim, Phys. Status Solidi B **76**, 301 (1976).

[54] M. E. Jacox, J. Mol. Struct. **157**, 43 (1987).

[55] M. E. Jacox, J. Mol. Spectrosc. **113**, 286 (1985).

[56] K. K. Rebane, *Impurity Spectra of Solids* (Plenum Press, New York, London, 1970).

[57] A. Nitzan, S. Mukamel, and J. Jortner, J. Chem. Phys. **63**, 200 (1975).

[58] V. E. Bondybey, J. Chem. Phys. **66**, 4237 (1977).

[59] V. E. Bondybey, in *Photoselective chemistry*, edited by J. Jortner (John Wiley & Sons, Inc., ADDRESS, 1981), Vol. 2.

[60] V. E. Bondybey and L. E. Brus, in *Advances in Chemical Physics*, edited by R. Prigogine and S. A. Rice (John Wiley & Sons, ADDRESS, 1980), Vol. 41.

[61] V. E. Bondybey, Ann. Rev. Phys. Chem. **35**, 591 (1984).

[62] H. Dubost and R. Charneau, Chem. Phys. **12**, 407 (1976).

[63] A. M. Smith, J. Agreiter, C. Engel, and V. E. Bondybey, Chem. Phys. Lett. **207**, 531 (1993).

[64] V. E. Bondybey and A. Nitzan, Phys. Rev. Lett. **38**, 889 (1977).

[65] V. E. Bondybey, J. Chem. Phys. **65**, 2296 (1976).

[66] H. J. Jodl, in *Chemistry and Physics of Matrix-Isolated Species*, edited by L. Andrews and M. Moskovits (North–Holland, Amsterdam Oxford New York Tokyo, ADDRESS, 1989).

[67] S. C. Foster and T. A. Miller, J. Chem. Phys. **93**, 5986 (1989).

[68] D. Forney, W. E. Thompson, and M. E. Jacox, J. Chem. Phys. **97**, 1664 (1992).

[69] R. L. Huang, S. H. Goh, and S. H. Ong, *The Chemistry of Free Radicals* (Edwald Arnold, London, 1974).

[70] V. E. Bondybey and J. H. English, J. Chem. Phys. **74**, 6978 (1981).

[71] V. E. Bondybey, Science **227**, 125 (1985).

[72] T. G. Dietz, M. A. Duncan, D. E. Powers, and R. E. Smalley, J. Chem. Phys. **74**, 6511 (1981).

[73] M. Lorenz, Master's thesis, Technische Universität München, 1995.

[74] A. Prengel, J. Dehaven, E. Johnson, and P. Davidovits, J. Appl. Phys. **48**, 3551 (1977).

[75] M. Downer, R. Fork, and C. Shank, J. Opt. Soc. Am. **B2**, 595 (1985).

[76] P. C. Engelking, Chem. Rev. **91**, 399 (1991).

[77] J. R. Gilbert, G. E. Leroi, and J. Allison, Int. J. Mass Spectrom. Ion Processes **107**, 247 (1991).

[78] P. H. Dawson, *Quadrupole Mass Spectrometry and its Applications* (Elsevier, Amsterdam, 1976).

[79] A. M. Smith, V. E. Bondybey, M. Horn, and P. Botschwina, J. Chem. Phys. **100**, 765 (1994).

[80] P. Fayet and L. Wöste, Z. Phys. D **3**, 177 (1986).

[81] S. Fedrigo, F. Meyer, D. M. Lindsay, J. Ligniers, J. C. Rivoal, and D. Kreisle, J. Chem. Phys. **93**, 8535 (1990).

[82] S. Fedrigo, W. Harbich, and J. Buttet, J. Chem. Phys. **99**, 5712 (1993).

[83] W. Harbich, S. Fedrigo, and J. Buttet, Z. Phys. D **26**, 138 (1993).

[84] W. Harbich, Y. Belyaev, R. Kleiber, and J. Buttet, Surf. Rev. Lett. **3**, 1147 (1996).

[85] Z. Hu, B. Shen, Q. Zhou, S. Deosaran, J. R. Lombardi, D. M. Lindsay, and W. Harbich, J. Chem. Phys. **95**, 2206 (1991).

[86] Z. Hu, J.-G. Dong, J. R. Lombardi, and D. M. Lindsay, J. Chem. Phys. **97**, 8811 (1992).

[87] Z. Hu, B. Shen, J. R. Lombardi, and D. M. Lindsay, J. Chem. Phys. **96**, 8757 (1992).

[88] Z. Hu, J.-G. Dong, J. R. Lombardi, and D. M. Lindsay, J. Phys. Chem. **97**, 9263 (1993).

[89] Z. Hu, G. Jian, J. R. Lombardi, and D. M. Lindsay, J. Chem. Phys. **101**, 95 (1994).

[90] J.-G. Dong, Z. Hu, R. Craig, J. R. Lombardi, and D. M. Lindsay, J. Chem. Phys. **101**, 9280 (1994).

[91] H. Haouari, H. Wang, R. Craig, J. R. Lombardi, and D. M. Lindsay, J. Chem. Phys. **103**, 9527 (1995).

[92] H. Wang, R. Craig, H. Haouari, J.-G. Dong, Z. Hu, A. Vivoni, J. R. Lombardi, and D. M. Lindsay, J. Chem. Phys. **103**, 3289 (1995).

[93] H. Wang, H. Hanouari, R. Craig, J. R. Lombardi, and D. M. Lindsay, J. Chem. Phys. **104**, 3420 (1996).

[94] H. Wang, R. Craig, H. Haouari, Y. Liu, J. R. Lombardi, and D. M. Lindsay, J. Chem. Phys. **105**, 5355 (1996).

[95] H. Wang, H. Haouari, R. Craig, Y. Liu, J. R. Lombardi, and D. M. Lindsay, J. Chem. Phys. **106**, 2101 (1997).

[96] H. Wang, Y. Liu, H. Haouari, R. Craig, J. R. Lombardi, and D. M. Lindsay, J. Chem. Phys. **106**, 6534 (1997).

[97] H. Wang, Z. Hu, H. Haouari, R. Craig, Y. Liu, J. R. Lombardi, and D. M. Lindsay, J. Chem. Phys. **106**, 8339 (1997).

[98] H. Wang, Y. Liu, H. Haouari, R. Craig, J. R. Lombardi, and D. M. Lindsay, J. Phys. Chem. A **101**, 7036 (1997).

[99] J. T. Godhout, T. M. Halasinski, G. E. Leroi, and J. Allison, J. Phys. Chem. **100**, 2892 (1996).

[100] T. M. Halasinski, J. T. Godbout, J. Allison, and G. E. Leroi, J. Phys. Chem. **98**, 3930 (1994).

[101] T. M. Halasinski, J. T. Godbout, J. Allison, and G. E. Leroi, J. Phys. Chem. **100**, 14865 (1996).

[102] J. P. Maier, Mass Spectrom. Rev. **11**, 119 (1992).

[103] J. P. Maier, Chem. Soc. Rev. **26**, 21 (1997).

[104] P. Freivogel, J. Fulara, D. Lessen, D. Forney, and J. P. Maier, Chem. Phys. **189**, 335 (1994).

[105] J. Fulara, P. Freivogel, D. Forney, and J. P. Maier, J. Chem. Phys. **103**, 8805 (1995).

[106] D. Forney, P. Freivogel, J. Fulara, and J. P. Maier, J. Chem. Phys. **102**, 1510 (1995).

[107] J. Agreiter, A. M. Smith, and V. E. Bondybey, Chem. Phys. Lett. **241**, 317 (1995).

[108] A. M. Smith, J. Agreiter, and V. E. Bondybey, Chem. Phys. Lett. **244**, 379 (1995).

[109] M. Grutter, M. Wyss, J. Fulara, and J. P. Maier, J. Phys. Chem. A **102**, 9785 (1998).

[110] M. Grutter, M. Wyss, and J. P. Maier, J. Chem. Phys. **110**, 1492 (1999).

[111] P. Freivogel, M. Gutter, D. Forney, and J. P. Maier, J. Chem. Phys. **107**, 4468 (1997).

[112] M. Tulej, D. A. Kirkwood, G. Maccaferri, O. Dopfer, and J. P. Maier, Chem. Phys. **228**, 293 (1998).

[113] M. Grutter, M. Wyss, E. Riaplov, and J. P. Maier, J. Chem. Phys. **111**, 7397 (1999).

[114] M. Tulej, D. A. Kirkwood, M. Pachkov, and J. P. Maier, Astrophys. J. **506**, 69 (1998).

[115] D. A. Kirkwood, H. Linnartz, M. Grutter, O. Dopfer, C. Motylewski, M. Pachkov, M. Tulej, M. Wyss, and J. P. Maier, Faraday Discuss. **109**, 109 (1998).

[116] S. Fedrigo, T. L. Haslett, and M. Moskovits, J. Am. Chem. Soc. **118**, 5083 (1996).

[117] T. L. Haslett, K. A. Bosnick, and M. Moskovits, J. Chem. Phys. **108**, 3453 (1998).

[118] T. L. Haslett, K. A. Bosnick, S. Fredrigo, and M. Moskovits, J. Chem. Phys. **111**, 6456 (1999).

[119] Princeton Electronic Systems, Inc., SIMION 3D, Version 6.0, http://www.sisweb.com/simion.htm, 1995.

[120] E. V. Savchenko, A. N. Ogurtsov, O. N. Grigorashchenko, M.Beyer, M. Lorenz, A. Lammers, and V. E. Bondybey, NIMB accepted (2000).

[121] E. V. Savchenko, O. N. Grigorashchenko, A. Ogurtsov, V. V. Rudenkov, G. Gumenchuk, M. Lorenz, A. Lammers, and V. Bondybey, submitted to J. Low. Temp. Phys. (2000).

[122] V. E. Bondybey and T. A. Miller, J. Chem. Phys. **73**, 3035 (1980).

[123] A. M. Smith, J. Agreiter, M. Härtle, C. Engel, and V. E. Bondybey, Chem. Phys. **189**, 315 (1994).

[124] M. D. Morse, Chem. Rev. **86**, 1049 (1986).

[125] J. F. Harrison, J. Phys. Chem. **100**, 3513 (1996).

[126] C. W. Bauschlicher, Jr., S. R. Langhoff, H. Partridge, and M. Sodupe, J. Phys. Chem. **97**, 856 (1993).

[127] H. Wu, S. R. Desai, and L.-S. Wang, J. Chem. Phys. **103**, 4363 (1995).

[128] G. V. Chertihin, W. Saffel, J. T. Yustein, L. Andrews, M. Neurock, A. Ricca, and C. W. Bauschlicher, Jr., J. Phys. Chem. **100**, 5261 (1996).

[129] J. G. Kay, D. W. Green, K. Duca, and G. L. Zimmermann, J. Mol. Spectrosc. **138**, 49 (1989).

[130] K. R. Thompson, W. C. Easley, and L. B. Knight, J. Phys. Chem. **77**, 49 (1973).

[131] W. H. E. Schwarz, A. Rutkowski, and S. G. Wang, Int. J. Quant. Chem. **57**, 641 (1996).

[132] A. Gatterer and S. G. Krishnamurty, Nature **169**, 543 (1952).

[133] W. Weltner, Jr. and D. McLeod, Jr., J. Mol. Spectrosc. **17**, 276 (1965).

[134] D. W. Green and K. M. Ervin, J. Mol. Spectrosc. **89**, 145 (1981).

[135] A. N. Samoilova, Y. M. Efremov, and L. V. Gurvich, J. Mol. Spectros. **86**, 1 (1981).

[136] C. J. Nelin and C. W. Bauschlicher, Chem. Phys. Lett. **118**, 221 (1985).

[137] L. A. Heimbrook, M. Rasanen, and V. E. Bondybey, J. Phys. Chem. **91**, 2468 (1987).

[138] J. K. Bates and D. M. Gruen, J. Mol. Spectrosc. **78**, 284 (1979).

[139] Cheetham and Barrow, Trans. Faraday Soc. **63**, 1835 (1967).

[140] L. Schriver-Mazzuoli, A. Schriver, C. Lugez, A. Perrin, C. Camy-Peyret, and J.-M. Flaud, J. Mol. Spectrosc. **176**, 85 (1996).

[141] M. Berkowitz and R. B. Gerber, Chem. Phys. Lett. **49**, 260 (1977).

[142] F. Legay, Chem. Biochem. Appl. Lasers **2**, 43 (1977).

[143] H. Kono and S. H. lin, J. Chem. Phys. **79**, 2748 (1983).

[144] P. F. Zittel and C. B. Moore, J. Chem. Phys. **59**, 6636 (1973).

[145] V. E. Bondybey and L. E. Brus, J. Chem. Phys. **63**, 794 (1975).

[146] C. Blindauer, M. Winter, O. Sild, G. Jansen, B. A. Hess, and U. Schurath, J. Phys. Chem. **97**, 10002 (1993).

[147] N. Caspary, B. E. Wurfel, A. M. Smith, and V. E. Bondybey, Chem. Phys. **220**, 241 (1997).

[148] L. Abouaf-Marguin, B. Gauthier-Roy, J. Dupre, and C. Meyer, Mol. Spectrosc. **110**, 347 (1985).

[149] B. E. Wurfel, G. Schallmoser, G. M. Lask, J. Agreiter, A. Thoma, R. Schlachta, and V. E. Bondybey, Chem. Phys. **174**, 255 (1993).

[150] D. H. Katayama, T. A. Miller, and V. E. Bondybey, J. Chem. Phys. **71**, 1662 (1979).

[151] L. Young and C. B. Moore, J. Chem. Phys. **81**, 3137 (1984).

[152] A. Leger and J. L. Puget, Astron. Astrophys. **137**, L5 (1984).

[153] L. J. Allamandola, A. G. Tieles, and J. R. Barker, Astrophys. J. **290**, L25 (1985).

[154] D. T. Anderson and J. S. Winn, Chem. Phys. **189**, 171 (1994).

[155] D. T. Anderson, S. Davis, and D. J. Nesbitt, J. Chem. Phys. **107**, 1115 (1997).

[156] M. Beyer, A. Lammers, E. V. Savchenko, G. Niedner-Schatteburg, and V. E. Bondybey, Phys. Chem. Chem. Phys. 2213 (1999).

[157] A. Garcia-Vela, R. B. Gerber, and J. J. Valentini, J. Chem. Phys. **97**, 3297 (1992).

[158] P. Zdanska, B. Schmidt, and P. Jungwirth, J. Chem. Phys. **110**, 6246 (1999).

[159] B. Poully and M. Monnerville, Chem. Phys. **238**, 437 (1998).

[160] D. E. Milligan and M. E. Jacox, J. Chem. Phys. **47**, 278 (1967).

[161] I. Last and T. F. George, J. Chem. Phys. **89**, 3071 (1988).

[162] A. I. Krylov and R. B. Gerber, J. Chem. Phys. **106**, 6574 (1997).

[163] V. E. Bondybey and G. C. Pimentel, J. Chem. Phys. **56**, 3832 (1972).

[164] D. E. Mann, N. Acquista, and D. White, J. Chem. Phys. **44**, 3453 (1966).

[165] B. Laroui, O. Damak, O. Maillard, and C. Girardet, J. Chem. Phys. **97**, 2359 (1992).

[166] Y. Hannachi and B. Silvi, J. Mol. Struct. **200**, 1989 (1989).

[167] V. E. Bondybey, J. Chem. Phys. **66**, 995 (1977).

[168] B. Laroui, J. P. Perchard, and C. Girardet, J. Chem. Phys. **97**, 2347 (1992).

[169] A. Thoma, G. Schallmoser, A. M. Smith, B. E. Wurfel, and V. E. Bondybey, J. Chem. Phys. **100**, 5387 (1994).

[170] R. Almi, B. Gerber, and V. A. Apkarian, J. Chem. Phys. **89**, 174 (1988).

[171] V. E. Bondybey, G. C. Pimentel, and P. N. Noble, J. Chem. Phys. **55**, 540 (1971).

[172] R. N. Kortzeborn and P. N. Noble, J. Chem. Phys. **52**, 5375 (1970).

[173] D. E. Milligan and M. E. Jacox, J. Chem. Phys. **55**, 2550 (1971).

[174] M. Pettersson, J. Nieminen, L. Khriachtchev, and M. Räsänen, J. Chem. Phys. **107**, 8423 (1997).

[175] E. B. Gordon, V. V. Khmelenko, A. A. Pelmenev, E. A. Popov, O. F. Pugachev, and A. F. Shestakov, J. Chem. Phys. **170**, 411 (1997).

[176] R. E. Boltnev, E. B. Gordon, V. V. Khmelenko, I. N. Krushinskaya, M. V. Martynenko, A. A. Pelmenev, E. A. Popov, and A. F. Shestakov, Chem. Phys. **189**, 367 (1994).

[177] A. Nicklass, M. Dolg, H. Stoll, and H. Preuss, J. Chem. Phys. **102**, 8942 (1995).

[178] N. Bartlett, Proc. Chem. Soc. London 218 (1962).

[179] F. O. Sladky, P. A. Bullier, and N. Bartlett, J. Chem. Soc. A 2179 (1969).

[180] J. G. Malm, H. Selig, J. Jortner, and S. A. Rice, Chem. Rev. **199**, 65 (1965).

[181] C. A. Coulson, J. Chem. Soc 1442 (1964).

[182] K. Seppelt and D. Lentz, Prog. Inorg. Chem. **29**, 167 (1982).

[183] J. H. Holloway, J. Flourine Chem. **33**, 149 (1986).

[184] C. K. Jørgensen and G. Frenking, Struct. Bonding **73**, 1 (1990).

[185] L. Y. Nelson and G. C. Pimentel, Inorg. Chem. **6**, 1758 (1967).

[186] J. J. Turner and G. C. Pimentel, Science **140**, 975 (1963).

[187] V. E. Bondybey, Ph.D. thesis, University of California, Berkeley, 1972.

[188] J. Lundell and H. Kunttu, J. Phys. Chem. **96**, 9774 (1992).

[189] H. Kunttu, J. Seetula, M. Räsänen, and V. A. Apkarian, J. Chem. Phys. **96**, 6530 (1992).

[190] M. Pettersson, J. Lundell, and M. Räsänen, J. Chem. Phys. **103**, 205 (1995).

[191] M. Pettersson, J. Lundell, L. Khriachtchev, and M. Räsänen, J. Chem. Phys. **109**, 618 (1998).

[192] M. Pettersson, J. Lundell, L. Khriachtchev, E. Isoniemi, and M. Räsänen, J. Am. Chem. Soc. **120**, 7979 (1998).

[193] M. Pettersson and J. Nieminen, Chem. Phys. Lett. **283**, 1 (1998).

[194] M. Lorenz, D. Kraus, M. Räsänen, and V. E. Bondybey, J. Chem. Phys. **112**, 3803 (2000).

[195] V. E. Bondybey and J. H. English, J. Chem. Phys. **73**, 3098 (1980).

[196] V. E. Bondybey, J. H. English, and T. A. Miller, J. CHem. Phys. **70**, 1621 (1979).

[197] T. J. Sears, T. A. Miller, and V. E. Bondybey, J. Chem. Phys. **74**, 3240 (1981).

[198] H. M. McConnel, J. Chem. Phys. **34**, 13 (1961).

[199] V. E. Bondybey and T. A. Miller, J. Chem. Phys. **70**, 138 (1979).

[200] K.P.Huber and G. Herzberg, *Molecular Spectra and Molecular Structure, IV. Constants of diatomic molecules* (Van Nostrand Reinhold Company, New York, 1979).

Acknowledgement

This thesis is dedicated to my parents. They provided me with with their love and financial support – the sound fundament which allowed me to complete this work. Therefore I would like to express to them my deep and cordial “thank you”.

I would also like to express my deep gratitude to my supervisor Prof. Vladimir E. Bondybey whose overwhelming knowledge, fruitful ideas and critical advice are the second fundament of this work. The warm reception in his institute provided me with an atmosphere which made working a pleasure.

I gratefully acknowledge the financial support of the Deutsche Forschungsgemeinschaft through the DFG proposal Bo945/18-1 permitting the implementation of the new experiment, as well as the Fonds der Chemischen Industrie for their generous support.

Without the collaboration and intense, fruitful discussions with my colleagues Dr. Alice M. Smith-Gicklhorn and the former FTIR group members Dr. Jürgen Agreiter and Nicola Caspary, this work would have been impossible. Special thanks to Alice for her careful proof-reading of this thesis.

I would also like to mention the pleasant collaboration with Dr. Elena V. Savchenko – she knew how to keep us busy – and with Prof. Markku Räsänen who compelled me to readjust considerably my thinking regarding rare gas chemistry and whose great black humor shortened several long hours in the lab.

The help of Peter Kämmerer and Fritz Klaus, who did all the “dirty jobs” including the synthesis of all kind of toxic or explosive compounds, is gratefully acknowledged.

Furthermore, I would like to thank Andreas “The Hacker” Lammers, and in recent times Peter; without their assistance in numberless fights with different computer systems, this work probably would not exist. In particular, I acknowledge the infinite patience of ever helpful Andreas who introduced me into the secrets of UNIX and teached me to esteem it highly.

Finally, I cordially thank the rest of the Bondybey group, Dieter Kraus, Bernd Urban, Brigitte S. Fox, Björn Reinhard, Uwe Achatz from Lower Bavaria, and especially Dr. Martin Beyer and Prof. Gereon Niedner-Schatteburg, as well as our secretary Sabine Kullick, for their ever cooperative attitude.